# DEVELOPMENT OF ADVANCED RADIATION MONITORS FOR PULSED NEUTRON FIELDS


Thesis submitted in accordance with the requirements of the

University of Liverpool for the degree of Doctor in Philosophy

by

**Giacomo Paolo Manessi**

June 2015

# Abstract

The need of radiation detectors capable of efficiently measuring in pulsed neutron fields is attracting widespread interest since the 60s. The efforts of the scientific community substantially increased in the last decade due to the increasing number of applications in which this radiation field is encountered. This is a major issue especially at particle accelerator facilities, where pulsed neutron fields are present because of beam losses at targets, collimators and beam dumps, and where the correct assessment of the intensity of the neutron fields is fundamental for radiation protection monitoring.

LUPIN is a neutron detector that combines an innovative acquisition electronics based on logarithmic amplification of the collected current signal and a special technique used to derive the total number of detected neutron interactions, which has been specifically conceived to work in pulsed neutron fields. Due to its special working principle, it is capable of overcoming the typical saturation issues encountered in state-of-the-art detectors, which suffer from dead time losses and often heavily underestimate the true neutron interaction rate when employed for routine radiation protection measurements.

This thesis presents a comprehensive study into the design, optimisation and operation of two versions of LUPIN, based on different active gases. In addition, two other devices, a beam loss monitor and a neutron spectrometer, which have been built using LUPIN's acquisition electronics, are also discussed in detail. Experimental results obtained in a number of facilities where the detectors have been exposed to most diverse and extreme conditions are shown in order to demonstrate the superior instrument performance in a critical assessment with commercial devices commonly employed for personnel and machine protection.

# Table of contents

# List of tables

# List of figures

FIG. 49. Experimental set-up for the measurements performed with the 178 mm sphere at the CERN PS: BSS-LUPIN (left) and conventional CERN BSS (right).

FIG. 50. Spectrum calculated at PS for the measurements performed with the CERN BSS and the BSS-LUPIN, unfolded with MAXED.

# List of abbreviations

The abbreviations are listed here in alphabetical order. Each acronym is also given in parentheses at the first appearance of the full expression in the text.

| | |
|---|---|
| ACCREDIA | Italian National Centre for Accreditation |
| ADC | Analogue to Digital Converter |
| BLM | Beam Loss Monitor |
| BNC | Bayonet Neill-Concelman |
| BSS | Bonner Sphere Spectrometer |
| CERF | CERN-EU Reference Field |
| CNAO | Italian National Centre for Oncological Hadrontherapy |
| EURADOS | European Radiation Dosimetry group |
| FEL | Free Electron Laser |
| FPGA | Field Programmable Field Array |
| HiRadMat | High Radiation to Materials |
| HZB | Helmholtz Zentrum Berlin |
| IC | Ionisation Chamber |
| LINAC | Linear Accelerators |
| LINUS | Long Interval Neutron Survey Meter |
| LogAmp | Logarithmic Amplifier |
| LUPIN | Long Interval Ultra Wide Dynamic Pile Up Free Neutron Rem Counter |
| MCC | Mean Collected Charge |

| | |
|---|---|
| MSV | Mean Square Voltage |
| M.U. | Monitoring Units |
| PMMA | Poly-Methyl Meth-Acrylate |
| PMT | Photo Multiplier Tube |
| PNF | Pulsed Neutron Fields |
| PS | Proton Synchrotron |
| RAMSES | Radiation Monitoring System for the Environment and Safety |
| rem | Roentgen Equivalent Man |
| SCA | Single Channel Analyser |
| SDD | Single-crystal Diamond Detector |
| SPS | Super Proton Synchrotron |
| SS | Straight section |
| TTL | Transistor-Transistor Logic |
| VELO | Vertex Locator |
| Wendi | Wide Energy Neutron Detection Instrument |

# 1. Introduction

## 1.1. Neutron detection

*"These results, and others I have obtained in the course of the work, are very difficult to explain on the assumption that the radiation from beryllium is a quantum radiation, if energy and momentum are to be conserved in the collisions. The difficulties disappear, however, if it be assumed that the radiation consists of particles of mass 1 and charge 0, or neutrons* [Chadwick 1932]*."* It took a while to the scientists of the first half of the nineteenth century to understand the characteristics of the particle they were dealing with and to give it a proper name. Several hypotheses were made in order to justify the presence of this very penetrating radiation that could not be easily stopped even in lead, including the hypothesis made by Rutherford in 1920 [Rutherford 1920] and the theory that Ambartsumjan and Iwanenko developed in 1930 [Ambartsumjan and Iwanenko 1930]. Only Chadwick in 1932 speculated, and later proved, the existence of a neutral particle that allowed the energy and momentum conservation laws to be still written in physics books without having to justify a troublesome exception, and gave it the name of neutron. The late discovery of this particle if compared to the discovery of electrons (1897) and protons (1919) was linked to the fact that it did not easily interact and could not be easily stopped in matter. A direct consequence of this is that neutrons still constitute the most difficult radiation field to be detected and stopped. Neutrons are usually detected through nuclear reactions that result in prompt energetic charged particles such as protons, alpha particles or heavier nuclides. The most common techniques involve the combination of a target material designed to perform the conversion between neutron and a charged particle and another material in which the charged particle can deposit at least a fraction of its energy. Since essentially all nuclear reactions show an interaction probability, i.e. a cross section, whose value is maximum for low-energy neutrons with a rapid decrease for increasing neutron energy, the target material is usually coupled with a moderating material in order to reduce the energy of the impinging neutrons and then to increase the interaction probability. The three most commonly employed nuclear reactions for thermal neutron detection are listed below, whereas no indication is given on reactions induced by fast neutrons or on methods employed to derive the neutron kinetic energy.

One of the most employed reactions for the detection of thermal neutrons is the $^{10}B(n,\alpha)^{7}Li$ reaction. The atom of $^{7}Li$ can be produced in the excited state with a branching ratio of 94% or directly

to the ground state with a branching ratio of 6%, under the assumption that the reaction has been induced by thermal neutrons. The Q-value of the reaction is 2.310 MeV or 2.792 MeV, depending on whether the $^{7}$Li atom is produced in its excited or ground state, respectively. When it is produced in its excited state, the $^{7}$Li atom returns with a half-life of $10^{-13}$ s to its ground state via the emission of a 480 keV gamma ray. The Q-value is much higher than the energy of the incoming neutrons and therefore the energy imparted to the reaction products is essentially equal to the Q-value itself. Similarly, as the linear momentum of the impinging neutrons is negligible, the reaction products are emitted in exactly opposite directions, and the energy is always shared between them in the same way, i.e. 0.84 MeV for the excited $^{7}$Li atom and 1.47 MeV for the α particle. The thermal cross section for this reaction is 3840 b, while its value drops with increasing neutron energy, being proportional to the reciprocal of the neutron speed. The popularity of this reaction comes not only from the high cross section value but also from the fact that highly enriched boron is readily available.

Another reaction commonly employed for thermal neutron detection is the $^{6}$Li(n,α)$^{3}$H reaction. The $^{3}$H atom is produced only in the ground state and the reaction Q-value is 4.78 MeV. As for the $^{10}$B(n,α)$^{7}$Li reaction, the Q-value is much higher than the energy of the impinging neutrons, and this results in an energy transmitted to the reaction products which is essentially equal to the Q-value itself. The $^{3}$H atom and the α particle are emitted in opposite directions with an energy of 2.73 MeV and 2.05 MeV, respectively. The reaction cross section for thermal neutrons is 940 b, with the usual decrease for higher energy, which is proportional to the reciprocal of the neutron speed. Even if the $^{6}$Li(n,α)$^{3}$H reaction is characterised by a lower cross section than the $^{10}$B(n,α)$^{7}$Li reaction, it has the advantage of a higher Q-value, thus resulting in an easier discrimination of the neutron-induced events from the electronics noise and the photon background. Moreover, as for $^{10}$B, also $^{6}$Li is readily available in separated form.

The $^{3}$He(n,p)$^{3}$H reaction is another reaction employed for detection of thermal neutrons. The atom of $^{3}$H is produced in the ground state only and the reaction Q-value is 764 keV. The reaction products are emitted in opposite directions with energy of 573 keV for the proton and 191 keV for the $^{3}$H atom. The thermal cross section is 5330 b, with the usual dependence on the reciprocal of the neutron speed. $^{3}$He is a rare isotope of helium and, even if it is commercially available, its cost is relatively high and in the last years a shortage of the $^{3}$He stocks occurred worldwide [Shea and Morgan 2010, Nuttall 2012]. This is a direct consequence of the fact that $^{3}$He is produced as a by-product of the maintenance

of nuclear weapons and for many years its supply outstripped the demand, until the September 11th attack, after which the U.S. government began deploying $^{3}$He neutron detectors at the borders for homeland security. To face this problem, several solutions are being thought on how to increase the production via other techniques and to reduce the demand by employing new technologies based on different detection reactions. Nevertheless, since the situation nowadays seems to be partially improved, for the studies performed in the framework of this thesis, it has been considered that the provision of $^{3}$He will still be possible at affordable prices in the next years.

Less than 20 years after the discovery of the neutron by Chadwick, the scientists started to concentrate their efforts not only on the neutron detection techniques, which were developed in a relatively short time, but also on the problems arising from the detection of neutrons in pulsed fields. In fact with the development of the first particle accelerators it came clear that techniques had to be developed in order to detect short pulses of radiation, both photons and neutrons, by limiting the counting losses induced by the instrument dead time. Westcott was one of the pioneers in this research field, since in one of his papers in 1948 he stated that "*One of the outstanding trends in the present phase of research in nuclear physics is the use of increasingly large and complex machines for the acceleration of charged particles to very high energies… A feature common to all machines giving particles of the highest energies is that their output is not continuous, but occurs in bursts or pulses separated by relatively long intervals during which the machine gives no output… The difficulty which arises in electrical counting when the source is pulsed is due to the finite resolution of any counting system. Thus, following any count, there is a dead time during which the system would be unable to record a further count, should one occur* [Westcott 1948]*."* In his long paper he tries to define several correction equations to compensate for these dead time losses based on several hypotheses and it ends up with complex tables where one should find a correction factor to be applied to the instrument readings in specific radiation conditions. This was the only way known at the time to limit the problem, since no solutions existed on how to reduce the dead time under a certain value. This first investigation triggered the interest of the scientific community, which ended up later on with numerous studies focused on this topic. Section 1.2. explains the details of the problems in the present scientific context and outlines the main scientific needs.

## 1.2. Detection in pulsed neutron fields

The need of radiation detectors capable to measure efficiently in pulsed neutron fields (PNF) is attracting widespread interest for applications such as radiation protection and beam diagnostics in research and medicine particle accelerators. Since the 1960s, numerous investigations focused on the development of detectors specifically conceived to work in pulsed fields. This is a major issue at particle accelerators, where pulsed neutron and photon fields are present because of beam losses at targets, collimators and beam dumps. The interest in active detectors to be employed in PNF is constantly increasing due to the growing number of applications where the time structure of the stray neutron field is characterised by a pulsed structure, i.e. by radiation bursts whose duration varies in a range from few ns to few ms with a typical repetition rate in the range 0.1-100 Hz [Caresana et al. 2013c]. Among the different applications we can find ultra-high intensity lasers, where a power varying from hundreds of TW to a few PW is delivered onto a target in bursts whose duration is in the order of hundreds of fs [Agosteo 2010], hadrontherapy facilities, characterised by a spill duration of 1 s and repetition rate of about 0.5 Hz [Rossi 2011], material testing facility, spallation sources [Andersen et al. 2012], medical linear accelerators (LINAC), laser plasma facilities and free electron lasers (FEL), where the accelerator is usually operated at a repetition rate of 10 Hz and a bunch duration of a few ps [Pedrozzi 2010]. In all these applications the pulsed structure of the radiation field hinders the use of active detectors operating in pulse mode in the halls housing the accelerators and the beam lines, including the treatment rooms, thus limiting their use in areas where the field intensity has been reduced and the typical duration of the bursts increased. Therefore the choice is usually directed towards passive detectors, which show several limitations, notably the fact that they cannot display the ambient dose equivalent, $H^*(10)$, rate in real time and that real time alarms cannot be set. Section 1.3 will describe the main limitations that affect the performance of active detectors in PNF and the related causes.

Pulsed radiation usually consists of a sequence of short bursts, but also single bursts delivered at low repetition rates are not uncommon. Though the $H^*(10)$ which characterises a single burst is usually low, and would not constitute a problem in terms of averaged $H^*(10)$ rate over the entire measurement period, the $H^*(10)$ rate during the radiation burst can reach extremely high values, up to 100 Sv/h in typical medical diagnostics applications and up to $10^7$ Sv/h in facilities such as the ones used for material testing [Schmidt et al. 2009], and this usually leads to severe underestimations of the $H^*(10)$. Recent measurements around research particle accelerators reported severe under response in

commercial active neutron detectors [Leake et al. 2010] with tremendous underestimation of the *H*(10)*, up to three orders of magnitude [Klett et al. 2007].

The main cause of this underestimation can be attributed to dead time losses, which are a distinctive feature of active detectors working in pulse mode. An active radiation detector can in fact operate in three modes: current, mean square voltage (MSV) and pulse mode. Current mode averages out the fluctuations in the intervals between individual interactions and is usually employed with high interaction rates when there is no need of preserving the information on the amplitude and timing of single interactions. MSV mode, whose detection principle is based on a special processing of the fluctuating component of the detector current signal, becomes useful when making measurements in mixed radiation environments when the charge produced by one type of radiation is much different than that from the second type. Pulse mode is the most commonly applied, especially for applications that are better served by preserving information on the amplitude and timing of individual events. This is the case for most neutron active detectors where the output usually consists of a sequence of individual pulses, each representing the results of a single interaction. One of the advantages of pulse mode operation is that the sensitivity is greater than when using current or MSV mode, because each interaction can be detected as a distinct pulse. This is a desirable property for radiation protection measurements because of the low detection limits required. The downside is represented by the dead time losses induced by the counting system, which can be correctly compensated only in the case of steady-state sources of constant intensity, but not in the case of pulsed sources. An ideal detector would in fact count every event that occurs. However, a real detector and its read-out electronics need a specific amount of time to create and process an output pulse. An event that occurs during this time span cannot be registered correctly. Depending on the detector system, it is either suppressed (non paralysable systems) or changes the shape of the previously detected pulse, resulting in a pile up (paralysable systems). The minimal time between two separately detectable events is called the dead time of the detector and the consequent losses are called dead time losses. The dead time for state-of the-art neutron detectors typically ranges from 1 to 10 μs.

It is clear that an ideal active detector should not be affected by dead time losses if it has to be employed in PNF. However, this is not the only constraint. One can define five other requirements that an active neutron detector should show for efficiently working in PNF:

1) capability to withstand very high instantaneous neutron fluxes with little or no saturation;

2) high sensitivity, usually expressed in $nSv^{-1}$, at least comparable with that of commercially available rem counters, i.e. about 1 $nSv^{-1}$;
3) capability to measure correctly the intensity of a single neutron burst;
4) capability to reject the photon contribution that usually accompanies the neutron fields;
5) good sensitivity over the entire neutron energy range, especially to high-energy neutrons, which is desirable for use in high-energy fields like those encountered around particle accelerators or cosmic ray fields.

Section 1.3 gives a brief review of the active detectors available at the state of the art and of their main limitations, with a special focus on the five requirements listed above.

### 1.3. State of the art detectors

One way to deal with the problem of the detection in PNF is to use activation detectors and there has been extensive research in this field since the 1970s [Mayer and Brysk 1975, Slaughter and Pickles 1979]. A considerable effort has recently been put on the improvements of silver activation detectors [Dighe et al. 2004], for which experiments have shown good linearity of the response in PNF [Luszik-Bhadra et al. 2010]. These detectors, however, show some limitations: they have a low neutron sensitivity, i.e. about 9 $\mu Sv^{-1}$ for a bare $^{252}Cf$ source [Luszik-Bhadra and Hohmann 2009], and they can detect a neutron *H*(10)* of 10 μSv in a reliable way only if the photon contribution is a factor of 10 lower [Luszik-Bhadra et al. 2010]. However, the crucial issue is the response time, which is determined by the half-life of the Ag isotope: the neutron capture (n,γ) on $^{107}Ag$ and $^{109}Ag$ produces $^{108}Ag$ and $^{110}Ag$ isotopes, characterised by a half-life of 25 s and 144 s, respectively, which subsequently decay by $\beta^-$ emissions in $^{108}Cd$ and $^{110}Cd$. The approach based on silver activation detectors eventually fulfils the requirements 1 and 4 given in Section 1.2, but does not permit the measurement of the intensity of a single neutron burst. Moreover the sensitivity is about two orders of magnitude worse than commercially available rem counters.

An alternative approach which relies on the activation of $^{12}C$ has recently been proposed in a new survey meter designed to work in PNF [Klett et al. 2010]. It detects neutron via the (n,pα), (n,x) and (n,p) reactions on $^{12}C$ and the resulting production of $^{8}Li$, $^{9}Li$ and $^{12}B$ isotopes, which subsequently decay by $\beta^-$ emissions in $^{8}Be$, $^{9}Be$ and $^{12}C$. The decay process is fast, being characterised by a half-life of 840 ms, 178 ms and 20 ms, respectively, but the (n,p) reaction on $^{12}C$ have a threshold at 14 MeV.

This means that the instrument has limited applications as it can only be used for detecting with good efficiency neutrons above 20 MeV, and has strong limitations in sensitivity and on the burst repetition rate over which it can be used [Leake et al. 2010]. Consequently, the requirements 1 and 2 cannot be fulfilled.

Single-crystal diamond detectors (SDD) have been used effectively in PNF [Rebai et al. 2012]. Diamond is characterised by one of the highest atomic density and allows an SDD to have very high radiation efficiency per unit of volume and, consequently, extremely compact dimensions. The high mobility of the charge carriers leads to a very fast response, which minimizes the dead time losses, provided that the SDD is coupled to special fast amplifiers. The fast neutron detection is based on the (n,α), (n,p) and (n,d) reactions on $^{12}C$ which produce $^{9}Be$, $^{12}B$ or $^{11}B$. However, these detectors are sensitive only to high-energy neutrons, above a few MeV, and must be coupled with $^{6}LiF$ or $^{10}B$ in order to detect thermal neutrons, but this would increase the complexity of the detector and alter the fast response properties.

A different approach which is using a proportional counter connected to a conventional acquisition chain has recently been proposed in order to reduce the counting losses in PNF [Weizhen et al. 2009]. This method takes into account the nearly simultaneous detection of two or three neutrons, which are discriminated by the single interaction event and which generate a double or triple logic signal at the output of the single channel analyser (SCA). However, this method proved to be reliable up to a limit of 100 counts generated by a single burst in the detector and a limit of 0.1 Gy/h on the photon $H^*(10)$ rate that accompanies the neutron field. The limit on the number of counts is very stringent and does not allow the detector to meet the requirements 1 and 3.

A promising theoretical method which allows dealing with the typical problems of the detection in PNF has recently been proposed [Leake et al. 2010]. It is based on the exploitation of the die-away of thermalised neutrons in the detector moderator: when a large neutron burst is detected, the interaction rate is initially too high to be correctly detected but then it exponentially decays and, after a certain time, it falls below a certain level where the dead time losses become negligible. If a proper algorithm is implemented in the detector acquisition system, then the size of the initial burst can be calculated by measuring the tail of the signal, i.e. by measuring the integrated number of detected interaction from the time when the interaction rate falls below a certain level. This is a very promising

method, which will be further investigated in Section 2.4, but at present it has not been put into practice in any detector acquisition system.

Recently a new neutron monitor has been designed to measure the $H^*(10)$ rate of high intensity neutron bursts generated by beam losses in an accelerator [Iijima et al. 2011]. This detector is based on a current readout and shows no count losses in a dynamic range from 4 μSv/h to 5 mSv/h. The drawback of the current working mode is that the monitor cannot distinguish a signal generated by a photon and a neutron and it cannot preserve the information on the amplitude and timing of the single interactions. It cannot therefore operate under stringent constraints and the requirements 1 and 4 cannot be respected.

This brief review showed that at the state of the art there is no device capable of fulfilling all the requirements listed in Section 1.2 for efficiently measuring in PNF. A new approach is treated in this thesis: an innovative detection principle, based on logarithmic amplification, and subsequent integration, of the current signal collected at the output of a proportional counter, is applied as the main operating principle of the detection devices: an extended range rem counter, a beam loss monitor (BLM) and an extended range Bonner Sphere Spectrometer (BSS). Chapter 2 describes the rem counter, its working principle, the results of measurements performed in various stray field conditions, and goes into the details of some aspects of the detector physics; Chapter 3 describes the working principle of the BLM, the measurements performed and the basic principles of its implementation in an machine protection system; Chapter 4 describes the physical characteristics of the BSS, the procedure followed to calculate the response of each sphere as a function of the impinging neutron energy, and the measurements carried out in different radiation environments. The conclusions are given in Chapter 5, together with the lists the possible applications of the innovative instrumentation described in this thesis and the potential future developments.

# 2. LUPIN, an innovative rem counter

This chapter describes an innovative rem counter called Long interval Ultra-wide dynamic Pile-up free Neutron rem counter (LUPIN) and the measurement campaigns performed to test and improve its performance. The term *rem counter* is used as an inheritance of past decades, when the first instruments capable of directly relating the results of the measurements with the corresponding neutron equivalent dose were called Roentgen equivalent in man (rem) counter or rem meter, with a direct reference to the measuring unit of the time. These detectors should be called nowadays *H*(10) counters*. However, the old acronym is still widely used in radiation protection to define all instruments based on a thermal neutron detector and on a moderating assembly capable of directly relating the number of measured counts with the neutron *H*(10)*. Therefore the term *rem counter* has been used throughout the text to define LUPIN and similar instruments. Section 2.1. describes the main characteristics and the working principle of this innovative rem counter. Section 2.2. reports the description and the results obtained in several measurements campaigns in which the detector has been tested to verify its performance and to understand its possible applications and limitations. Section 2.3. discusses the origin and the consequences of the space charge effect which is the main cause of the limitations observed in the detector when it is exposed to extremely intense PNF. Section 2.4. is focused on the experimental evidence of the presence of a neutron die-away time characteristic of any thermal neutron detector such as LUPIN and on the proposal of an innovative acquisition technique based on this die-away time which should be in principle applicable to any neutron detector working in pulse mode.

The aim of the measurement campaigns described in this chapter was to test the detector in the most different stray field conditions in order to analyse its *in the field* performance and to derive useful information from each test in order to implement changes in its physical characteristics, in the acquisition interface and in the off-line analysis techniques. This allowed optimizing the detector performance in parallel while continuing planning new measurement campaigns, thus drastically reducing the time required to reach the actual development, i.e. a prototype with robust reliability and well-known performance, as well as known limitations.

All measurements have been performed in the framework of my thesis work. Similarly, the data shown in the tables and in the figures, as well as the results at which the text indirectly refers, have been obtained during the work carried out in the PhD, opportunely supported by technicians, physicists and other colleagues, and under the close monitoring of the university supervisor. Where the discussion or the conclusions refer to measurements or data that have not been obtained by me personally, the text clearly refers to external sources, such as papers, conference proceedings, books or internal reports. In this latter case, since the reader could find difficulties in obtaining the original text, the bibliography reports, close to the standard reference formula, an hyperlink whose validity has been verified in May 2015.

## 2.1. The detector

LUPIN is a rem counter type instrument available in two versions, consisting of either a $^{3}He$ or a $BF_3$ proportional counter placed inside a spherical or cylindrical moderator, respectively. From now on, for simplicity, the text will refer to LUPIN-He and LUPIN-BF, respectively. The moderator is designed so that the response function of the instrument reproduces sufficiently well the curve of the conversion coefficients from neutron fluence to *H*(10)* over a wide energy range, as in the original extended range Long Interval NeUtron Survey meter (LINUS) [Birattari et al. 1990, Birattari et al. 1992, Birattari et al. 1993, Birattari et al. 1998].

The LUPIN-He moderator consists of a polyethylene sphere of 12.5 cm outer radius with lead and cadmium inserts, hosting at its centre the $^{3}He$. The inner part of the moderator, 5.6 cm in radius, is surrounded by a 6 mm thick lead shell. The outer layer of this inner polyethylene sphere hosts eleven cadmium buttons, 2.5 cm in radius and 1 mm thick. Polyethylene fillers are used to fill the void around the detector stem. A scheme and a photograph of the inner parts of LUPIN-He are shown in Fig. 1.

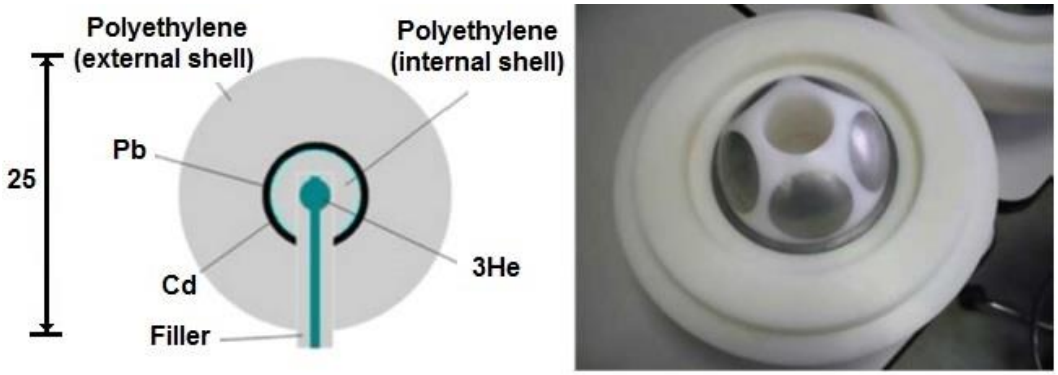


FIG. 1. Scheme and photograph of the inner parts of LUPIN-He, dimension in centimetres.

The same moderator has been used with CR-39 dosimeters and a $^{3}He$ proportional counter as a dual-detector extended range rem counter by Agosteo et al. [Agosteo et al. 2010]. The difference here is the presence of the electrostatic shielding that contains the detector and the polyethylene inserts, which is constituted by an aluminium cylinder of 1.5 mm thickness. In order to host this cylinder, the diameter of the polyethylene fillers was reduced by 3 mm.

The LUPIN-BF moderator consists of a polyethylene cylinder of 25 cm diameter with lead and cadmium inserts, hosting at its centre the $BF_3$. The electrostatic shielding has the same thickness of

the one used in the spherical moderator, i.e. 1.5 mm, but it is longer due to the bigger length of the $BF_3$ and of the polyethylene fillers. A scheme and a photograph of LUPIN-BF are shown in Fig. 2.

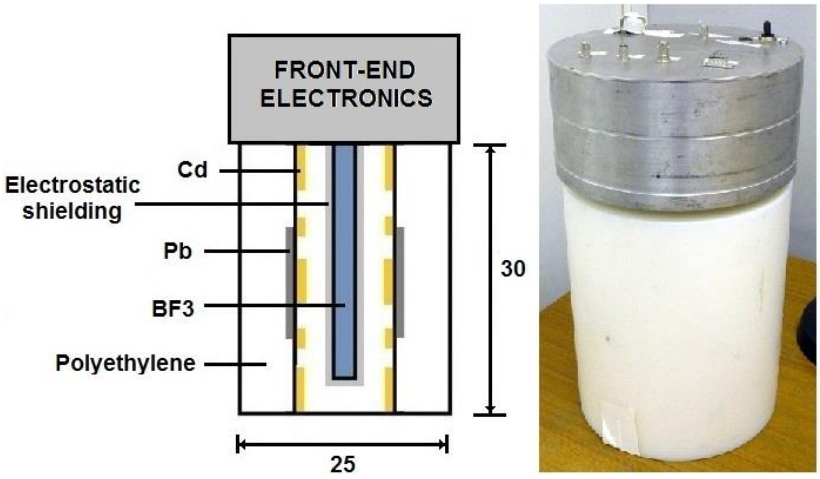


FIG. 2. Scheme and photograph of the moderating assembly of LUPIN-BF, dimensions in centimetres.

The proportional counters used in the two versions of LUPIN are a spherical Centronic SP9He3/152/Kr $^3$He and a cylindrical Centronic 15EB/20/25SS $BF_3$, characterised by a nominal pressure of 1520 mmHg (203 kPa) and 200 mmHg (267 kPa), respectively. However, even if the pressure of the $^3$He is nominally stated as 1520 mmHg (203 kPa), the actual pressure is 1748 mmHg (233 kPa), to which 912 mmHg (122 kPa) of Krypton is added as a quench gas [Sutter 2011].

The front-end electronics consists of a current-voltage logarithmic amplifier, whose output signal is acquired by an analogue to digital converter (ADC) with a conversion rate of 10 MSamples/s and processed with a LabVIEW program running on a PC. The idea at the basis of the software is simple: the voltage signal is converted back into a current signal and integrated over a time that can be freely set by the user. The result of this calculation represents the total charge generated in the detector by the neutron interactions. This quantity, divided by the average charge expected by a single neutron interaction, represents the number of interactions occurring during the integration time. The acquisition may start when the current signal overcomes a certain threshold, via the so called *trigger mode*, or at regular intervals, regardless of what the current value is, via the *streaming mode*. The first acquisition mode allows the user to focus its attention to the shape of the signal and guarantees that the data are not integrated in case of absence of neutron interactions. For most of the measurement campaigns this mode was employed. On the other hand, if one is interested in measuring the average neutron *H*(10)* in a

certain area, the *streaming mode* must be employed; otherwise the measured value would overestimate the actual one.

The scheme of the front-end electronics is shown in Fig. 3.

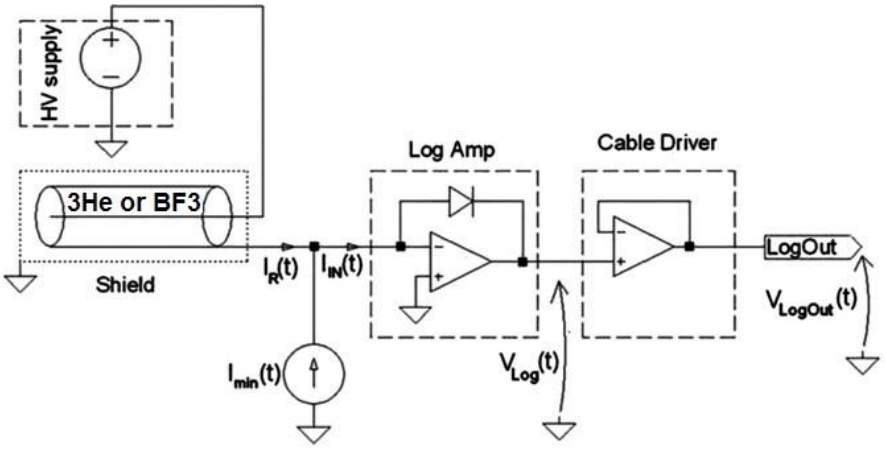


FIG. 3. Schematic working principle of the LUPIN electronics.

The polarisation between the electrodes of the proportional counter is provided by a user-adjustable internal high voltage supply. The electronics is based on a current-voltage logarithmic amplification of the signal produced inside the proportional counter. A fixed current $I_{min}$ is added to the current signal $I_R$ generated by the reactions inside the gas to avoid negative saturation in case of absence of signal generated by the neutron interactions. The current $I_{min}$ is usually set to 160 pA, but this value can be modified if necessary. A larger value of $I_{min}$ induces a faster response of the logarithmic amplifier (LogAmp). The sum of the two currents, $I_R + I_{min}$, is collected and processed by the LogAmp. Even if the value of $I_{min}$ is negligible for typical acquisition conditions, it plays a role when the detector is used to measure radiation background. Therefore proper techniques are put in place in order to subtract the charge generated by this very low current from the total charge, see Section 2.2.6. The proportional counter must be electrostatically shielded to avoid noise pick up. The electrostatic shield is constituted by an aluminium cylinder that encases the detector, as discussed above. The LogAmp output signal passes through a cable driver and the signal $V_{LogOut}$ is acquired via a PC digital oscilloscope (Picoscope™ 4424 by PicoTechnology) and monitored by the LabVIEW program. The choice of a LogAmp was driven by the need to achieve a dynamic range of a few orders of magnitude with respect to the burst intensity to be measured. Conventional LogAmps are too slow for the purpose of the detection of a radiation signal, because, as mentioned above, their response is characterised by long

time constants when they are fed with low currents, and this is usually the case during the detection of the tail of the signal. It was then decided to employ a high-speed LogAmp, i.e. the Texas Instruments LOG114. The LogAmp is declared to work over a range of eight decades (160 dB) with high temperature stability. The circuital scheme of the front-end electronics is shown in Fig. 4.

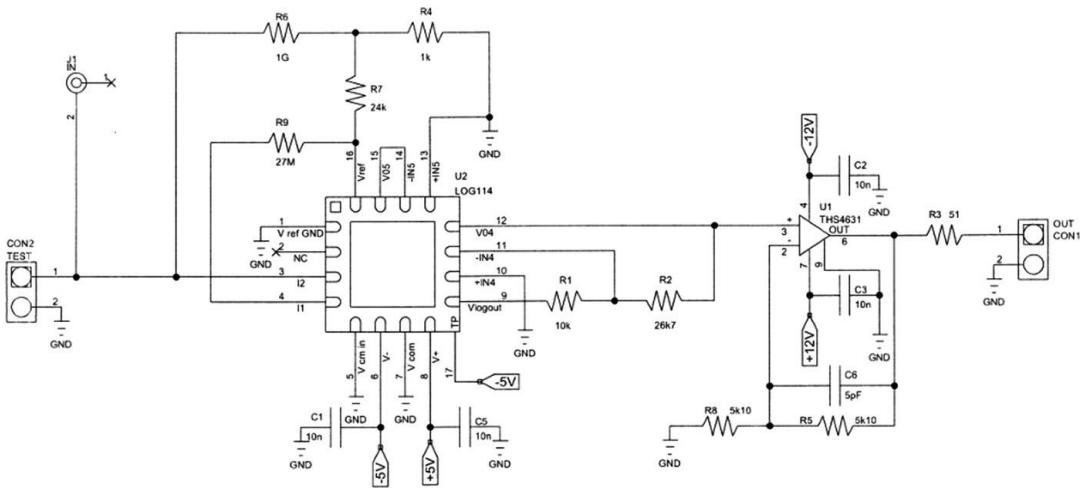


FIG. 4. Circuital scheme of the LUPIN electronics.

The principle of detection of LUPIN differs strongly from the ones employed by most active neutron detectors. It introduces in fact a big simplification in the overall acquisition chain. In a conventional detector working in pulse mode the signal generated in the proportional counter first needs to be pre-amplified before the main stage of amplification, and then needs to pass in an SCA in order to be discriminated from electronic noise and interactions of other particles, such as photons, in the detector. Eventually, a counter must be employed to display the total number of detected neutron interactions. In LUPIN, the signal is directly fed to the amplifier, and the number of neutron interactions is derived from the total integrated charge. The main advantage of this principle of detection is that the system is not affected by dead time losses, which are usually introduced by the SCA. The dead time losses can induce severe underestimations of the true interaction rate, as it has been explained in Section 1.2. For example a dead time of 5 μs, which is typical of a rem counter, leads to an underestimation of 50% at a true interaction rate of $2 \cdot 10^5$ $s^{-1}$, assuming that the acquisition electronics can be treated as a non-paralysable system [Knoll 2010b].

Both versions of LUPIN show some advantages and some drawbacks as well. The choice of the version should be driven by the type of application and by the characteristics of the stray radiation field in which it must be employed. The advantages of LUPIN-BF are the following:

- higher Q-value of the $^{10}B(n,\alpha)^{7}Li$ reaction if compared to the $^{3}He(n,p)^{3}H$ which results in a better photon rejection and, consequently, a better neutron/photon discrimination;
- larger active volume, 25 mm diameter and 150 mm length for the $BF_3$, to be compared with the 31 mm diameter for the $^{3}He$, which reflects in a mitigation of the space charge effect. This effect is generated when a large number of neutron interactions occur in the gas in a very short time: the space charge causes a reduction in the electric field around the anode and consequently a decrease in the multiplication factor. Its importance is therefore reduced if larger active volumes are employed [Rios et al. 2013]. A complete discussion on this topic, as well as on the possible countermeasures that can be put in place to limit its consequences, will be given in Section 2.3.

On the other hand, the advantages of LUPIN-He are:

- higher sensitivity, which is a direct consequence of the higher pressure and the higher multiplication factor of the $^{3}He$ compared to the $BF_3$;
- isotropic response, due to the spherical geometry of the proportional counter and the moderating assembly.

### 2.2. Measurements

The development of LUPIN was performed in parallel with the execution of tests and measurement campaigns. This allowed a continuous and progressive development of the detector and a consequent optimisation of its characteristics. Therefore the results obtained in the measurements and in the intercomparison campaigns will be presented by including at the end of each section the key information derived from each series of test, the limitations and the problems encountered, as well as the solutions implemented to solve them. The facilities where the detector has been employed were chosen in order to test LUPIN in most different radiation environments, ranging from a calibration laboratory to operational conditions around particle accelerators and extreme situations where the detector was brought to its limits of operation, reproduced on purpose in dedicated facilities or research centres. For each section a description of the facility and the expected stray field conditions is given, together with an overview of the radiation detectors employed. In many cases the measurements were carried out in the framework of larger intercomparisons or wider collaborations. In this case the attention is focused only on the results obtained with LUPIN. The description of the working principle,

the main specifications and the response functions of the detectors used for comparison in the different measurements are given in Appendix: throughout the section the detectors will be referred only with their commercial acronyms.

### 2.2.1. Detector calibration

The characterisation of LUPIN is connected to its working principle and requires the knowledge of two calibration factors, instead of the single calibration factor usually needed for a rem counter: the mean collected charge (MCC), expressed in fC, i.e. the average amount of charge generated in the detector by a neutron interaction. This is used to derive the number of neutron interactions occurring during the integration time, and the conversion coefficient from neutron interactions to $H^*(10)$, expressed in $nSv^{-1}$. The measurements were performed with calibrated neutron sources in two dedicated laboratories, at the *Politecnico di Milano* and at CERN.

The calibration in charge was performed in the calibration laboratory at the *Politecnico di Milano* with an AmBe source. Knowledge of the precise activity of the source is not an essential value for these measurements, since the only requirement is to have one, and only one, neutron interaction in each acquisition. The source-detector distance was therefore tuned in order to obtain about 10 $s^{-1}$ interactions, a rate low enough to avoid multiple interactions in a single acquisition, but sufficiently high to limit the time needed to reach a reasonably low statistical uncertainty on the integrated number of counts, i.e. less than 1%. Several integration times where used, ranging from 0.5 ms to 4 ms. Fig. 5 and Fig. 6 show the distributions for both versions of LUPIN, where the frequency of events for each bin has been normalised in order to set the sum of all the data to 1. The noise-induced low-energy events have been excluded from the plot: the full-energy deposition peak and the wall effect continuum are clearly visible. The wall effect is the direct consequence of the fact that the incoming neutrons carry no appreciable momentum. Therefore, the products of the neutron-induced reaction, $^3H$ and p in the case of $^3He$, $^7Li$ and $\alpha$ in the case of $BF_3$, are emitted in opposite directions and the reduced dimensions of the proportional counter do not allow a complete energy deposition of both particles [Knoll 2010d].

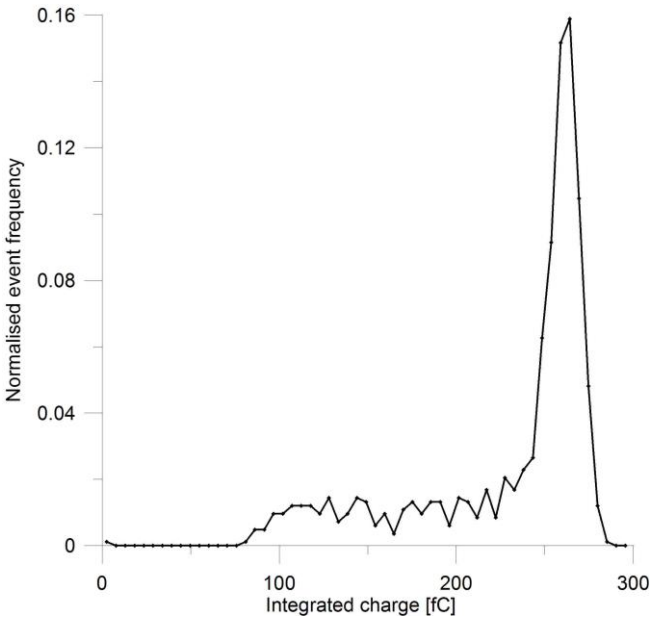


FIG. 5. Normalised distribution of the charge integrated with LUPIN-He over a 4 ms acquisition time.

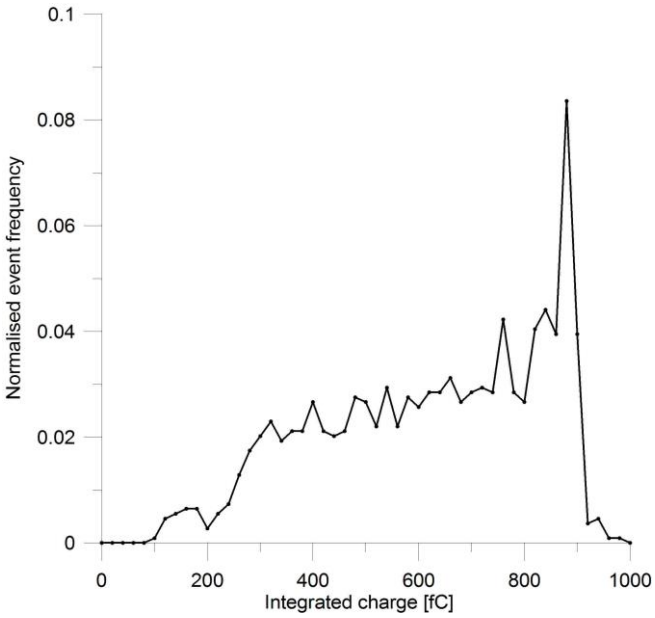


FIG. 6. Normalised distribution of the charge integrated with LUPIN-BF over a 4 ms acquisition time.

The MCC is defined as the weighted average of the charge distribution, after having set a proper upper and lower limit in order to cut the electronics noise and the energy depositions due to photon interactions in the gas. It depends on the detector, the operating voltage and the integration time, as shown in Table I: it reaches a *plateau* for integration times longer than 1 ms. For lower values the charge collection is incomplete due to the ballistic deficit, i.e. the difference in the amplitude of the pulse if compared to that attainable with an acquisition system characterised by an infinite time constant [Knoll 2010e]. The

uncertainty in the determination of the MCC is due to the statistical uncertainty on the integrated number of counts.

Table I. Values of MCC as calculated for several integration times.

| Integration time [ms] | MCC [fC] | |
|---|---|---|
| | LUPIN-He | LUPIN-BF |
| 0.5 | 211 ± 15 | 547 ± 38 |
| 1 | 229 ± 16 | 616 ± 43 |
| 2 | 243 ± 17 | 611 ± 43 |
| 3 | 251 ± 18 | 616 ± 43 |
| 4 | 260 ± 18 | 617 ± 43 |

The calibration in *H*(10)* was performed in the CERN calibration laboratory with a PuBe source. The integration time was set to 2 ms. The calibration factor was determined to be 2.13 ± 0.17 $nSv^{-1}$ for LUPIN-BF and 3.64 ± 0.26 $nSv^{-1}$ for LUPIN-He. In order to test the geometrical dependence of the response of LUPIN-BF, which is not isotropic due to the cylindrical shape of the moderating assembly, the calibration was also performed at different angular orientations, along the three detector axes, see Fig. 7.

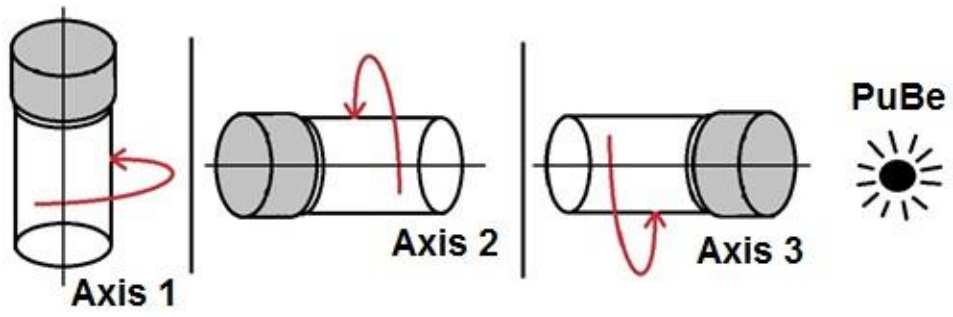


FIG. 7. Configurations used to test the geometrical dependence of LUPIN-BF. The red arrow indicates the positive direction of angular turning.

The detector has been turned in different orientations by steps of 30˚, from -150˚ to +180˚, in each of the three configurations. The results are shown in Fig. 8, where the uncertainties are not displayed for clarity. The total uncertainty is the sum of the statistical uncertainty on the integrated number of counts and the uncertainty on the calibration of the neutron source, i.e. 7%, as obtained from the source documentation.

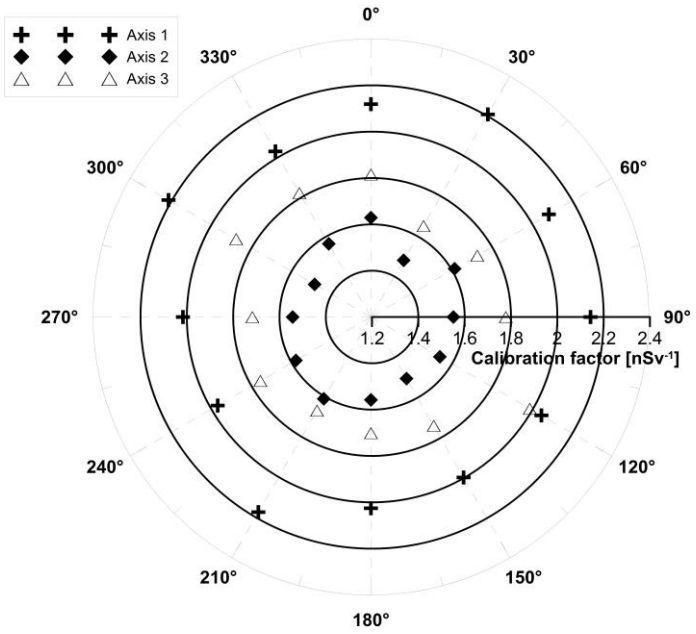


FIG. 8. *H*(10)* calibration factor obtained for different orientations of LUPIN-BF along the three axes. As expected, the response is not isotropic. However, the difference in the value of the calibration factor is always included in a ±20% variation, for all orientations along the three axes. This variation can be further limited if a $BF_3$ counter characterised by a lower active length is employed. Under this condition the height of the moderating assembly could be slightly reduced so that it would become approximately equal to the cylinder diameter, in order to resemble a quasi-isotropic geometry. However a lower active length of the proportional counter would result in reduced detector sensitivity.

### 2.2.2. Measurements in high-energy mixed fields

Measurements were carried out at the CERN-EU high-energy reference field (CERF) facility [Mitaroff and Silari 2002] to test the performance of LUPIN-BF in high-energy mixed fields. The facility was conceived to generate a stray radiation field which resembles the high-energy component of the radiation field created by cosmic rays at commercial flight altitudes. Although the detector is specifically conceived for PNF, a test in operational non-pulsed conditions is necessary. This is in fact a typical stray field that can be found not only at commercial flight altitudes but also close to the shieldings of high-energy particle accelerators, where LUPIN could be employed as an on-line radiation monitor for machine and personnel protection.

The CERF facility is installed in one of the of the secondary beam lines (H6) of the Super Proton Synchrotron (SPS) in the North Experimental Area on the Prévessin site of CERN. The stray radiation field at CERF is generated by a positive hadron beam (61% positive pions, 35% protons and

4% kaons) with momentum of 120 GeV/c impinging on a copper target, 7 cm in diameter and 50 cm in length, placed inside an irradiation cave, see Fig. 9.

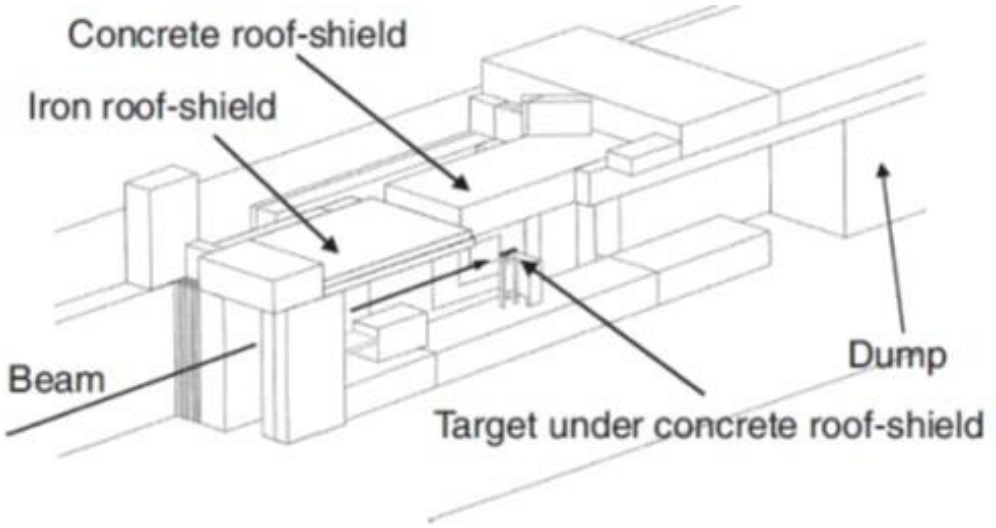


FIG. 9. Axonometric view of the CERF facility. The side shielding is removed to show the inside of the irradiation cave with the copper target set-up.

The secondary particles produced in the target traverse an 80 cm concrete shield on top. This roof shield produces an almost uniform radiation field over an area of 2 x 2 $m^2$ located at approximately 90º with respect to the incoming beam direction, divided in 16 squares of 50 x 50 $cm^2$. Each element of this grid represents a reference exposure location (concrete top, CT). The energy distribution of the particles, mainly neutrons, at the various exposure locations were obtained in the past by Monte Carlo simulations performed with the FLUKA [Ferrari et al. 2005, Battistoni et al. 2007] code. The neutron spectrum outside the concrete shielding is dominated by a peak at 100 MeV, a smaller evaporation peak at about 1 MeV and a low-energy tail due to backscatter radiation. The beam is delivered to the CERF facility from the SPS with a typical intensity of $10^8$ particles per SPS spill. The spill duration, i.e. the beam extraction time, varies along the years but during the measurements was equal to about 10 s over an SPS cycle of 48 s.

The beam monitoring was provided by an air-filled, parallel-plate, transmission type ionisation chamber (IC), which has been calibrated via the foil activation technique using the $^{27}Al(p,3pn)^{24}Na$ and $^{nat}Cu(p,x)^{24}Na$ monitor reactions [Ferrari et al. 2014]. The beam intensity measured by the IC was recorded every second in a log-file. The intensity is expressed in IC counts, since a current to frequency converter allows the output current to be converted in Transistor-Transistor Logic (TTL) signals, which are then acquired and counted by a National Instrument data acquisition device, NI DAQ USB 6341.

The foil activation experiments confirmed the validity of the calibration factor used in past years: 1 IC count corresponds to 22,000 ± 2,200 primary particles. The reliability of this value has also been verified via FLUKA simulations carried out in order to obtain the expected charge collected on the plates of the IC per primary particle. This allowed an extrapolated calibration factor of 22,172 ± 2,200 primary particles per IC count to be obtained, in excellent agreement with the value obtained via the foil activation experiment.

The measurements were performed by installing in turn LUPIN-BF in the 16 reference exposure locations on top of the concrete shield. Fig. 10 shows an example of the measurement set-up, where several detectors are exposed on the concrete roof.

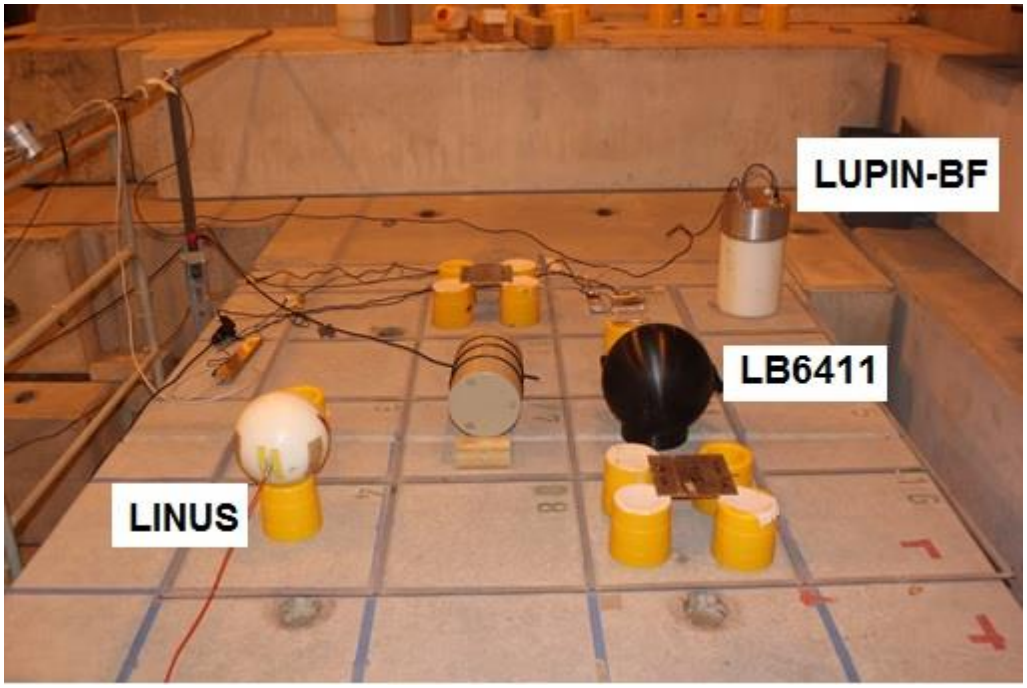


FIG. 10. Experimental set-up on the CERF concrete top shield.

The integration time of LUPIN-BF was set to 10 s in order to be synchronised with the SPS spill duration. An example of the signal output is shown in Fig. 11.

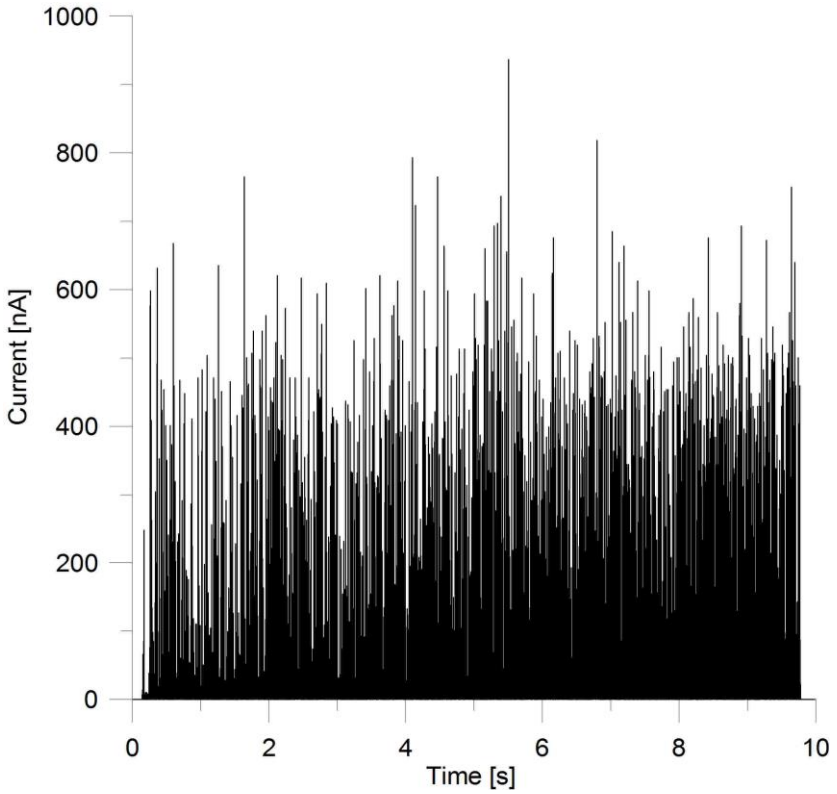


FIG. 11. Signal acquired with LUPIN-BF in the reference location CT16 at CERF.

The duration of the signal is equal to the spill duration of the SPS, i.e. about 10 s. The stray field is characterised by a huge number of current peaks very close one to the other, which result in an almost constant level of current throughout the entire spill. Each of the current spikes represents a neutron interaction in the detector and in some cases they represent pile upping interactions, which give rise to current peak up to 950 nA, clearly emerging in the signal. However, it cannot be excluded that some of the peaks have been generated by interactions of high-energy particles in the detector, which directly ionised the active gas or which resulted in a scattering event of atoms constituting the detector walls, which later deposited their energy in the gas. The results were obtained by integrating the *H*(10)* measured by LUPIN-BF in 15 minutes and by normalizing it to the integrated beam fluence, as obtained from the log files of the beam monitor, expressed in IC counts. These results were compared with the values foreseen by FLUKA simulations, see Table II.

Table II. Results of the measurements performed with LUPIN-BF in the CT reference locations at CERF, compared with the results derived from FLUKA simulations (uncertainty in parentheses).

| Location | CT1 | CT2 | CT3 | CT4 | CT5 | CT6 | CT7 | CT8 |
|---|---|---|---|---|---|---|---|---|
| LUPIN-BF (nSv/IC count) | 168 (51) | 203 (61) | n.a. | 177 (53) | 175 (53) | 224 (67) | 227 (68) | 197 (59) |
| FLUKA (nSv/IC count) | 216 (22) | 254 (25) | 253 (25) | 207 (21) | 225 (23) | 270 (27) | 270 (27) | 222 (22) |
| Ratio LUPIN-BF/FLUKA | 78% (8) | 80% (8) | n.a. | 86% (9) | 78% (8) | 83% (9) | 84% (9) | 89% (9) |
| Location | CT9 | CT10 | CT11 | CT12 | CT13 | CT14 | CT15 | CT16 |
| LUPIN-BF (nSv/IC count) | 169 (51) | 220 (66) | 232 (70) | 199 (60) | 149 (45) | n.a. | 193 (58) | 167 (50) |
| FLUKA (nSv/IC count) | 213 (21) | 267 (27) | 265 (27) | 207 (21) | 190 (19) | 223 (22) | 221 (22) | 182 (18) |
| Ratio LUPIN-BF/FLUKA | 79% (8) | 82% (9) | 88% (9) | 96% (10) | 78% (8) | n.a. | 87% (9) | 92% (10) |

n.a. = not available

The uncertainty on the measurements is due to the statistical uncertainty on the number of integrated counts and to the uncertainty on the reproducibility of the positioning, i.e. 2%, equal to 1/10 of the maximum difference between the reference value of $H^*(10)$ in a specific location and the adjacent ones. Since FLUKA simulations give a result that is normalised to the primary particles, the derived values have an uncertainty which is equal to the uncertainty on the calibration of the beam monitor, i.e. 10%.

There is a very good agreement between experimental and Monte Carlo results, though for some locations LUPIN-II slightly underestimates the $H^*(10)$. This underestimation reaches 15-20% for the locations placed on the left side of the concrete top, by taking as reference the picture shown in Fig. 10. This slight difference has been noticed in a similar experiment carried out with other rem counters in the same conditions and could be due to slight imprecisions of the geometry implemented in the FLUKA simulations, especially for what concerns the target position in the irradiation cave, as well as to the fact that the actual calibration factor of LUPIN-BF is higher when the stray field is reaching the detector from the bottom side, see Section 2.2.1.

The results obtained with LUPIN-BF in position CT7 were compared with the results obtained by other rem counters and neutron detectors in the same reference position. The detectors employed in this intercomparison, whose detailed description can be found in Appendix, were:

- conventional and extended range rem counters: LINUS, LB6411, Wendi-2 and BIOREM, whose response to neutrons can be enhanced by adding an external lead shell;
- other neutron detectors: RadEye™, in the $^{3}$He version, employed with its small-size polyethylene moderator to increase the efficiency to fast neutrons, and the ABC 1260 neutron dose-meter, a bubble detector using an active counting system, whose response can be extended to several hundred MeV with the addition of a 1 cm thick cylindrical lead shell placed around the detector cap.

The results are shown in Fig. 12.

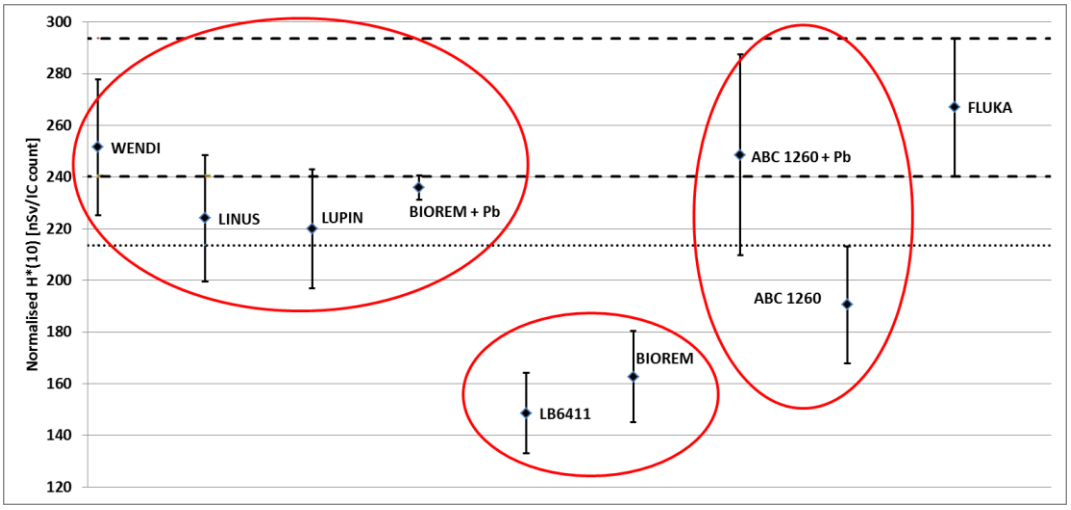


FIG. 12. Comparison between the *H*(10)* measured at CERF, grouped in detector classes: extended range (left) and conventional rem counters (centre), bubble detectors (right). The FLUKA value is also shown, together with the ±1σ (dashed line) and ±2σ deviations (dotted line).

The results obtained with the extended range rem counters, which include LUPIN-BF, are in good agreement within the range of uncertainties and agree within 1σ with the value obtained by FLUKA. The readings of the conventional rem counters are in good agreement within their uncertainties and underestimate *H*(10)*, as measured by the extended range instruments and as calculated by FLUKA, by about 40%. This is due to the reduced sensitivity of these detectors for neutrons with energies >10 MeV. The ABC detector behaves like a conventional rem counter when it is employed without the lead cap, otherwise its results are compatible with the extended range rem counters. The result of RadEye™ has been excluded from the plot because it overestimates the FLUKA value by more than a factor of two.

LUPIN-BF showed results in terms of integrated *H*(10)* which are compatible with what has been obtained by FLUKA simulations and by other extended range neutron detectors. Its reliable behaviour in high-energy fields derives from the fact that its response closely resembles the ICRP conversion curve from neutron fluence to *H*(10)*. The lead parts included in the detector assembly help improving its sensitivity above 20 MeV by spallation reactions of the type (n,xn) induced by high-energy neutrons. The multiple neutrons generated in these reactions are subsequently thermalised by polyethylene and diffuse until they reach the active part of the detector, thus improving its response. The small deviation of the measured from the simulated *H*(10)* for a few reference positions can be explained by the different calibration factor that should be applied to LUPIN-BF when it is exposed in a neutron field directed from the bottom to the top part of it. This variation of the calibration factor cannot be easily implemented and is due to the non-isotropic response of cylindrical neutron detectors. This issue could be partially resolved by reducing the height of the detector, thus trying to approach a quasi-spherical geometry. This could be done in two ways: by reducing the amount of polyethylene below the proportional counter or by reducing the active length of the proportional counter. However, if this would limit from one side the geometrical dependence of the calibration factor, it would add other limitations: a lower amount of polyethylene would consistently reduce the detector sensitivity for fast neutrons; moreover a reduced active length of the proportional counter would result in a reduced sensitivity in the entire neutron energy range. In conclusion, the measurement campaign confirmed the possibility of efficiently employing LUPIN in non-pulsed high-energy mixed fields, such as the one encountered around high-energy accelerators or in aircrafts at commercial flight altitudes.

### 2.2.3. Measurements in a reference pulsed field

A series of measurements was performed with both versions of LUPIN at the Helmholtz-Zentrum Berlin für Materialen und Energie GmbH (HZB) to test its performance in a reference pulsed neutron field of increasing intensity. The aim was to evaluate the linearity of the response of the detector, which was installed in a reference position 50 cm downstream of a tungsten target, as a function of the radiation burst charge impinging on it. The measurements were performed in the framework of a large intercomparison campaign organised by the Working Group 11 of the European Radiation Dosimetry Group (EURADOS), whose research is primarily focused on dosimetry in high-energy radiation fields.

The cyclotron used for the measurements is routinely employed for proton therapy of ocular tumours but, in addition to therapy, a small number of experiments for radiation hardness tests, detector tests and dosimetry are also performed. The beam line directed towards the treatment room, shown in Fig. 13, is equipped with a switching magnet that supplies the ion beam to the experimental room used for the measurements.

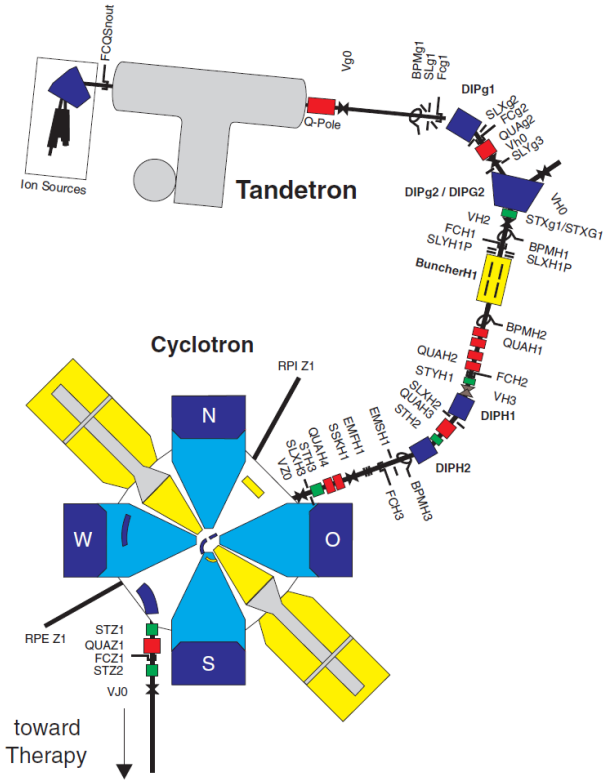


FIG. 13. The cyclotron complex at the HZB.

A 68 MeV proton beam accelerated by the cyclotron impinged on a 20 mm thick tungsten target. The choice of the target material was driven by the need of having the largest possible production of neutrons generated in spallation reactions from the primary beam. Therefore a high-Z material as tungsten, which is readily available, has been chosen. For treatment purposes the accelerator works in quasi-DC mode, whereas for this measurement campaign the proton beam was delivered in bursts by using a burst suppressor between the Van de Graaff injector and the cyclotron. The burst suppressor deflects the beam and sends it to the target only for the desired time. This technique allows generating radiation bursts with a time duration ranging from 50 ns to 1 ms with a maximum repetition rate of 100 kHz, whereas the beam current can vary between 0.5 pA and 300 nA. The possibility of varying these parameters allowed the intensity of radiation bursts to be spanned over five orders of magnitude. The

ion current was monitored on-line by measuring the signal of a transmission ionisation chamber installed upstream of the target and off line by a Faraday cup. This signal was employed to measure the proton charge impinging on the target. The detectors were placed on a trolley that was equipped with mechanical locks to ease the position reproducibility and that could be moved perpendicular to the optical bench axis.

The research centre provided the shape of the neutron spectrum emerging from the tungsten target and the value of the neutron and the photon yield, expressed in *H*(10)* per burst charge, expected in the reference position at 50 cm from the target. 96% of the *H*(10)* yield is due to neutrons with an energy below 10 MeV. This allows comparing conventional rem counters, which show a reduced sensitivity for neutrons with energy above 10 MeV, with extended range rem counters without the need of applying a correction factor. The photon *H*(10)* yield is two orders of magnitude lower than the neutron yield, thus assuring an effective photon rejection for all detectors.

Each detector was installed in the reference position and integrated the *H*(10)* for 10 minutes, an irradiation time long enough to allow the statistical uncertainty on the integrated counts to be reduced at a negligible value. The repetition rate was kept fixed to a frequency of 100 Hz. The integrated neutron *H*(10)* was divided by the total number of bursts that impinged on the target in order to get the neutron *H*(10)* per burst. This was compared with the value of the reference neutron *H*(10)* per burst, which was obtained by applying a conversion yield of 15.4 ± 1.0 nSv/pC to the burst charge, as provided by the research centre and as confirmed by a test carried out in a preliminary run performed before the main intercomparison campaign. This procedure was repeated for each detector and for several machine settings, whose complete list is given in Table III. It must be noted that the beam parameters were not exactly reproducible and therefore the burst charge could substantially vary from the values given in Table III. However, this did not affect the reliability of the measurements, since the exact reference *H*(10)* was always available, as derived by multiplying the output signal of the beam monitor by the conversion factor.

Table III. Accelerator settings used for measurements at HZB. The reference *H*(10)* per burst is calculated 50 cm downstream the target.

| Machine setting | Ion current [pA] | Burst current [nA] | Burst length [μs] | Burst charge [fC] | Reference *H*(10)* [nSv] |
|---|---|---|---|---|---|
| 1 | 0.5 | 5 | 1 | 5 | 0.077 |
| 2 | 1.5 | 15 | 1 | 15 | 0.231 |
| 3 | 3 | 30 | 1 | 30 | 0.462 |
| 4 | 5 | 50 | 1 | 50 | 0.770 |
| 5 | 10 | 100 | 1 | 100 | 1.54 |
| 6 | 25 | 250 | 1 | 250 | 3.85 |
| 7 | 50 | 500 | 1 | 500 | 7.70 |
| 8 | 75 | 750 | 1 | 750 | 11.6 |
| 9 | 100 | 1,000 | 1 | 1,000 | 15.4 |
| 10 | 250 | 250 | 10 | 2,500 | 38.5 |
| 11 | 500 | 500 | 10 | 5,000 | 77.0 |
| 12 | 1,000 | 1,000 | 10 | 10,000 | 154 |
| 13 | 3,000 | 800 | 40 | 32,000 | 493 |

The burst length varied from 1 μs to 40 μs but, for the purpose of the experiment, it can be considered that the neutron *H*(10)* has been delivered to the detectors in an infinitely small amount of time, being the highest burst length much smaller than the diffusion and thermalisation time of the neutrons in the moderator as will be shown in detail in Section 2.4. An example of the signal acquired with LUPIN-BF with machine setting 8 is shown in Fig. 14.

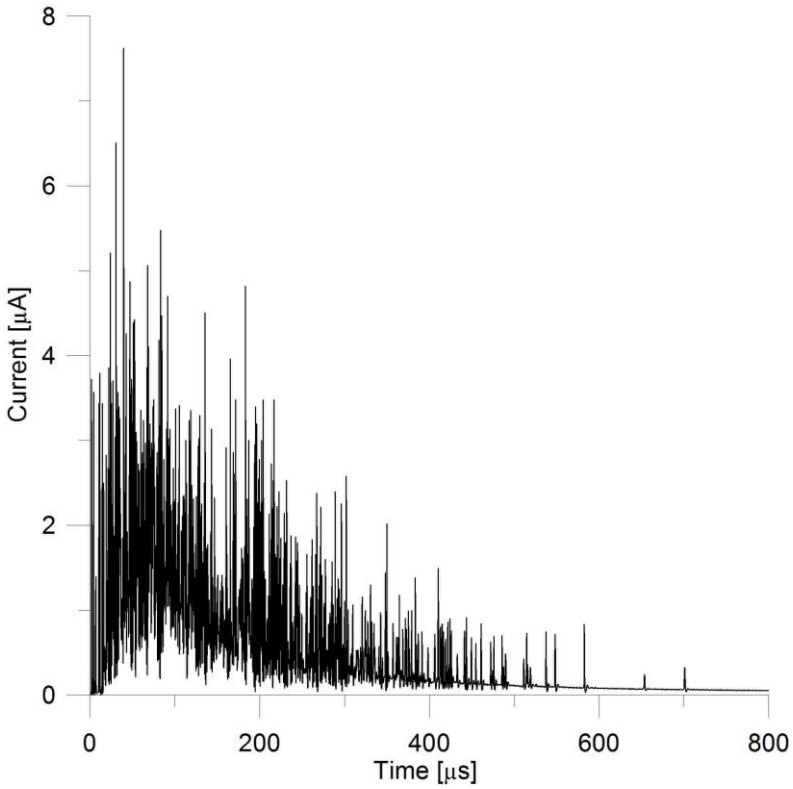


FIG. 14. Signal acquired with LUPIN-BF at HZB with machine setting 8.

Due to the extremely short proton burst length impinging on the target, the time structure of the signal acquired by LUPIN-BF is essentially dominated by the thermalisation and diffusion time of the neutrons in the detector moderator. This can be noticed by the fact that the signal reaches a peak after few tens of μs and then progressively decays, lasting for about 500 μs. If one assumes that the population of thermal neutrons in the moderator follows an exponential decay curve and that the number of neutron interactions becomes negligible after five decay constants, it can be derived that the decay constant of LUPIN-BF is approximately 100 μs, as explained in Section 2.4. The first few hundreds of μs of the signal are characterised by a considerable pile-up of the neutron interactions, with a maximum current peak of about 8 μA.

The results obtained with both versions of LUPIN are shown in Fig. 15. They are expressed in measured neutron *H*(10)* per burst as a function of the reference *H*(10)*. This latter has been calculated by applying the reference conversion factor to the burst charge. Where the uncertainty bar is not visible, it is smaller than the marker size.

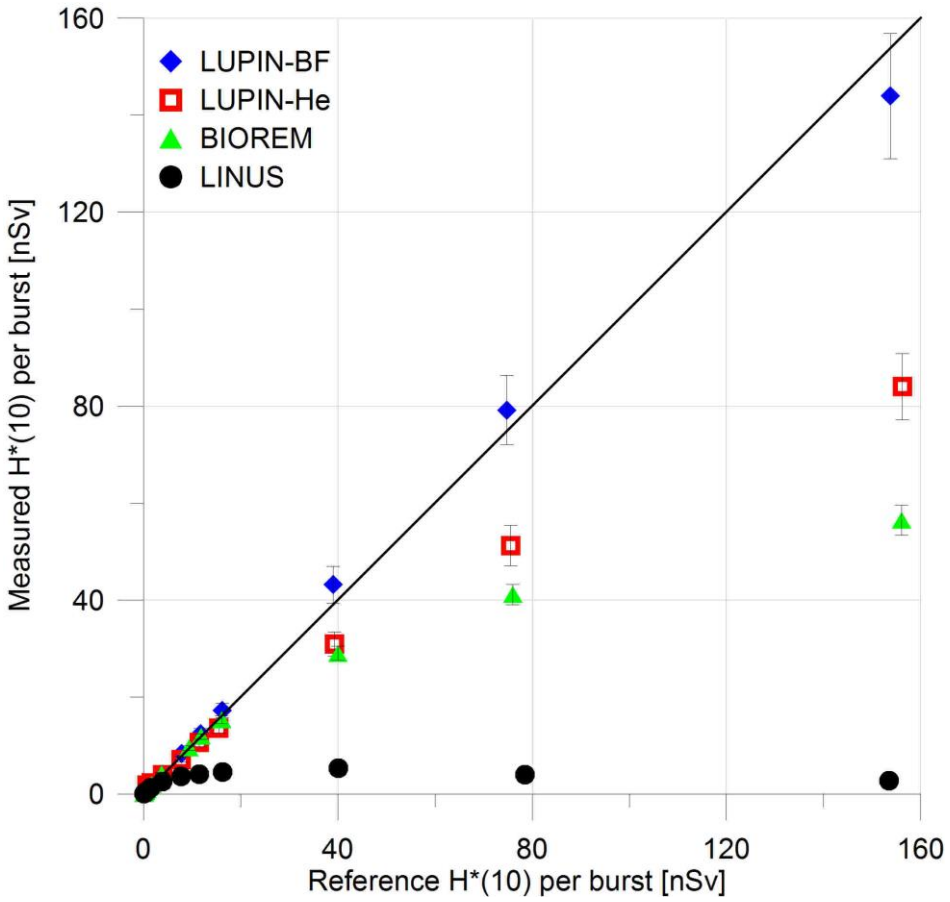


FIG. 15. Results obtained at HZB with both versions of LUPIN and two other rem counters for comparison: BIOREM and LINUS. The ideal behaviour is represented by the straight line.

For comparison the results of two other rem counters, typically employed for radiation protection measurements at CERN, are given on the same plot: LINUS and BIOREM. The first is an extended range rem counter, whereas the second is a conventional one, with limited sensitivity above 20 MeV but, as mentioned above, a direct comparison is possible in this experiment due to the negligible fraction of the neutron fluence above 10 MeV. A detailed description of the main characteristics of the two rem counters is given in the Appendix. The numerical results obtained with the four detectors are shown in Table IV. For some machine settings the results are not available: setting 13 was not initially foreseen and, due to the long beam tuning time needed, it was employed only for LUPIN-BF, i.e. the detector that showed the best performance for the other 12 settings. On the other hand some of the data obtained with settings 1, 2 and 3 were affected by poor statistics or acquisition problems and the corresponding results are not available.

Table IV. Results obtained with LUPIN-He, LUPIN-BF, BIOREM and LINUS at HZB, expressed in measured *H*(10)* per burst (uncertainty in parentheses).

| Setting | Ref. *H*(10)* [nSv] | LUPIN-He | LUPIN-BF | BIOREM | LINUS |
|---|---|---|---|---|---|
| 1 | 0.077 | n.a. | n.a. | 0.11 (0.01) | 0.09 (0.01) |
| 2 | 0.231 | n.a. | n.a. | 0.28 (0.01) | 0.24 (0.02) |
| 3 | 0.462 | n.a. | 0.73 (0.07) | 0.59 (0.03) | 0.46 (0.04) |
| 4 | 0.770 | 1.89 (0.18) | 0.99 (0.09) | 0.88 (0.04) | 0.83 (0.07) |
| 5 | 1.54 | 2.29 (0.20) | 1.62 (0.14) | 1.96 (0.12) | 1.32 (0.12) |
| 6 | 3.85 | 4.00 (0.32) | 4.13 (0.36) | 4.18 (0.26) | 2.63 (0.22) |
| 7 | 7.70 | 7.16 (0.68) | 8.35 (0.73) | 9.51 (0.47) | 3.63 (0.29) |
| 8 | 11.6 | 10.7 (0.9) | 12.5 (1.1) | 11.9 (0.6) | 4.11 (0.33) |
| 9 | 15.4 | 13.7 (1.1) | 17.3 (1.5) | 15.3 (0.8) | 4.54 (0.37) |
| 10 | 38.5 | 31.0 (2.5) | 43.2 (3.8) | 29.0 (1.5) | 5.38 (0.44) |
| 11 | 77.0 | 51.2 (4.2) | 79.2 (7.2) | 41.2 (2.1) | 4.06 (0.33) |
| 12 | 154 | 84.0 (6.8) | 144 (13) | 56.5 (3.1) | 2.77 (0.23) |
| 13 | 493 | n.a. | 402 (38) | n.a. | n.a. |

n.a. = not available

The total uncertainty is the sum of the statistical one on the integrated number of counts, conservatively assumed to be equal to 1%, the calibration one, derived from the neutron source used to calibrate the instruments, typically PuBe, AmBe or $^{252}$Cf, and the uncertainty on the beam monitoring, variable between 2% and 4%. The calibration uncertainty is not taken into account when one compares the readings of detectors calibrated with the same radioactive source, but here, since the detectors have been calibrated in several institutes with different neutron sources, it is necessary to take it into account for calculating the total uncertainty.

The results of LUPIN-BF are very close to the ideal behaviour for settings 1-12: the small deviations of the response from the linearity are included within the uncertainty. The LUPIN-He response is close to the linearity up to 20 nSv and starts to deviate for higher values, reaching a maximum under response of about 50% for the highest intensity. A higher deviation from linearity is shown by BIOREM, which measures roughly 40% of the reference *H*(10)* for the highest intensity.

LINUS shows a huge under response even for low values of reference *H*(10)* and its absolute response reaches a plateau before decreasing for values higher than 40 nSv per burst. This behaviour can be attributed to the fact that LINUS employs an acquisition chain that is paralysable, i.e. when the interaction rate increases the counting system becomes blind for most of the measuring time and therefore not capable to integrate counts,. For such a system, the measured interaction rate for an infinitely high true reaction rate tends to zero.

The measurement campaign allowed comparing the performance of several active neutron detectors in reference conditions, hardly reproducible in a typical radiation environment, characterised by an extremely short neutron burst with a negligible photon component, as well as with a negligible fraction of scattered radiation. Moreover, the availability of a reference conversion yield from burst charge to *H*(10)*, allowed a precise comparison of the measured with the reference neutron *H*(10)* value. Therefore the results obtained in these conditions provide a quantitative evaluation on the capability of a specific detector to efficiently operate in PNF.

According to the results obtained, one can divide the detectors in three groups, according to their operating principles:

- rem counters operating in pulse mode with a paralysable electronics, such as LINUS;
- rem counters operating in pulse mode with a non-paralysable electronics, the most common type, like BIOREM;
- LUPIN-BF and LUPIN-He.

The first group shows the most severe under response, even for low values of expected *H*(10)* per burst, making these detectors inappropriate for detecting PNF. The poor performance is not intrinsically related to the physical properties of the active gas, but it is only due to the signal processing performed by the acquisition chain. Therefore an improvement for these detectors could come from the replacement of the electronics used for the acquisition. The second group shows an underestimation of the response, which becomes more important as the expected *H*(10)* per burst increases. This is the typical behaviour of detectors affected by dead time losses, where the severity of the under response is directly related to the value of the dead time. As the expected *H*(10)* per burst increases, the measured *H*(10)* tends to an asymptotic value. If one looks at the measured interaction rate, this asymptotic value is given by the inverse of the system dead time. One way to improve their performance in PNF is to

reduce the dead time by changing, for example, the shaping time of the amplifier used in the acquisition electronics. However, most commercial detectors do not allow the user to change these settings, and this solution cannot be implemented. An alternative solution is to apply on the measured interaction rate a compensation factor obtained by the dead time correction formula for non-paralysable systems [Knoll 2010b]:

$$n = \frac{m}{1 - mD}, \tag{1}$$

where n is the true interaction rate, m is the measured interaction rate and D is the system dead time. This is, however, valid only in case of steady-state radiation fields of constant intensity, but not in the case of PNF, where, by definition, the interaction rate is not constant in time. The performance of both versions of LUPIN is better than all other detectors, especially in terms of expected *H*(10)* per burst above which the response starts to deviate from linearity. The LUPIN-BF response is essentially linear for the entire range of beam intensity, whereas LUPIN-He shows a moderate under response for the highest values of *H*(10)*. The good performance of both versions can be primarily attributed to the absence of dead time losses, given by its working principle. On the other hand, the slight saturation of LUPIN-He can be attributed to the space charge effect. This effect is generated when a large number of neutron interactions occur in the gas in a very short time: the space charge causes a reduction in the electric field around the anode and consequently a decrease in the multiplication factor. Its importance is therefore reduced if larger active volumes are employed [Rios et al. 2013], as it is the case for LUPIN-BF. A discussion on the dependence of this effect from the detector characteristics, as well as its quantification for the LUPIN case, will be comprehensively given in Section 2.3.

### 2.2.4. Measurements in an extremely intense radiation field

Measurements were carried out with LUPIN-BF at the High Radiation to Materials (HiRadMat) [Efthymiopoulos et al. 2011] facility at CERN in order to test its performance in an extremely intense stray field generated by a high-energy proton beam of very short duration impinging on a dump. The beam intensity was steadily increased during the experiment by more than three orders of magnitude, with a corresponding *H*(10)* due to neutrons in the measuring positions varying between a few nSv and a few μSv per burst, thus giving the opportunity to verify the detector response in the entire range of interest for applications involving machine and personnel protection in an accelerator

environment. The aim of the experiment was to evaluate the response linearity in extreme conditions as a function of the impinging burst intensity. Unlike in the measurements performed at HZB, described in Section 2.2.3., where the detector was exposed to a reference stray field, the radiation field in HiRadMat is characterised by a longer duration and by an important scattered component, a condition which is commonly found in the access tunnels of high-energy particle accelerators, i.e. a location where LUPIN-BF could find application as a radiation detector to be implemented in an on-line and centralised monitoring system.

HiRadMat is a newly constructed facility designed to provide high-intensity pulsed beams to an irradiation area where beam-to-material experiments can be performed. The facility has been constructed 35 m under the ground level at the existing tunnel of the old CERN WANF area [Astier et al. 2003]. The primary proton beam that reaches the irradiation area is extracted from the SPS. The nominal proton momentum is 440 GeV/c. The pulse consists of several bunches, whose number can be varied from 1 up to 288. The intensity of each bunch can be varied from $10^9$ up to $1.7 \cdot 10^{11}$ protons and the spacing between 25 ns and 100 ns. This gives a maximum pulse intensity of $5 \cdot 10^{13}$ protons per spill and a maximum pulse length of 28.8 μs, which is nevertheless much lower than the typical diffusion and thermalisation time of the neutrons in the moderator, as it will be shown in detail in Section 2.4. One pulse per SPS spill, approximately 48 s, can be extracted. The beam line optics allows for a flexible spot size from 0.5 $mm^2$ up to 2 $mm^2$. A layout of the experimental area is shown in Fig. 16, alongside with the code names of the tunnels.

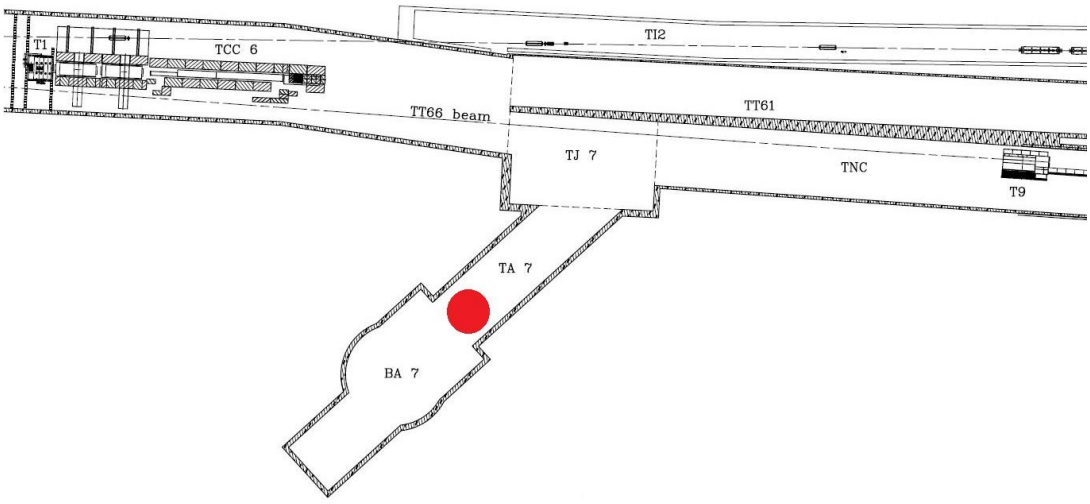


FIG. 16. Layout of the HiRadMat facility. The beam was impinging on the dump in the TNC tunnel. The red spot indicates the detector location.

For the purposes of the experiment, the proton beam was impinging directly on the beam dump, while the detectors were placed in the TA7 tunnel, just before the air-tight ventilation door that separates the experimental area from the access area. This was chosen in order to reduce the access time to the area in case of detector malfunctioning: in fact an access beyond the ventilation door would require a long flushing time for reducing air activation. A beam spot size of around 2 $mm^2$ and a bunch spacing of 50 ns were chosen. A list of the nominal intensities of the pulses to be extracted from the SPS and shot on the beam dump is given in Table V.

Table V. Nominal beam settings used during the measurements in HiRadMat.

| Beam setting | Pulse intensity [protons on dump] | Expected *H*(10)* per burst |
|---|---|---|
| 1 | $5 \cdot 10^9$ | 2.5-5 nSv |
| 2 | $10^{10}$ | 5-10 nSv |
| 3 | $2 \cdot 10^{10}$ | 10-20 nSv |
| 4 | $4 \cdot 10^{10}$ | 20-40 nSv |
| 5 | $7.5 \cdot 10^{10}$ | 37.5-75 nSv |
| 6 | $10^{11}$ | 50-100 nSv |
| 7 | $2 \cdot 10^{11}$ | 100-200 nSv |
| 8 | $4 \cdot 10^{11}$ | 200-400 nSv |
| 9 | $7.5 \cdot 10^{11}$ | 375-750 nSv |
| 10 | $10^{12}$ | 500-1000 nSv |
| 11 | $2 \cdot 10^{12}$ | 1-2 μs |
| 12 | $4 \cdot 10^{12}$ | 2-4 μs |
| 13 | $7.5 \cdot 10^{11}$ | 3.75-7.5 μs |

Each beam setting refers to the nominal values, while the intensities obtained during the measurements were slightly different and in a few cases some settings had to be skipped. An indication of the expected *H*(10)* per burst in the measuring area is also given, as obtained in a test run performed a few months before the main experiment. The *H*(10)* is due to neutrons only, since the photon component of the stray field is largely attenuated by the tunnel structures. This has been verified by dedicated FLUKA simulations, which demonstrated that the photon contribution to the total *H*(10)* accounts for less than

0.1% [Charitonidis et al. 2012]. The beam intensity is measured via a beam monitor affected by 3% uncertainty.

The LUPIN-BF response was compared with four active detectors routinely employed in the CERN Radiation Monitoring System for the Environment and Safety (RAMSES): BIOREM, Wendi-2, Argon and Hydrogen-filled Centronic ionisation chambers. A detailed description of the main characteristics of these detectors is given in the Appendix. All detectors were installed on a rotating structure, which has been designed in the form of a Ferris wheel, with five supports, each one attached to the skeleton in such a way that, as the wheel turns, the supports are kept upright by gravity. The structure was built of aluminium to minimize the total weight as well as to limit activation issues [Charitonidis and Harrouch 2013]. The presence of this structure allowed the five detectors to be tested for all the beam settings in five positions, so that the responses could be compared in the exact same conditions, in order not to be influenced by the high radiation gradient present in the area, as observed during the test run [Charitonidis et al. 2012]. The configuration scheme and a picture of the detectors mounted on the wheel are shown in Fig. 17, where LUPIN-BF was installed in position 1, Wendi-2 in position 2, BIOREM in position 3, the Ar-filled chamber in position 4 and the Hydrogen-filled chamber in position 5.

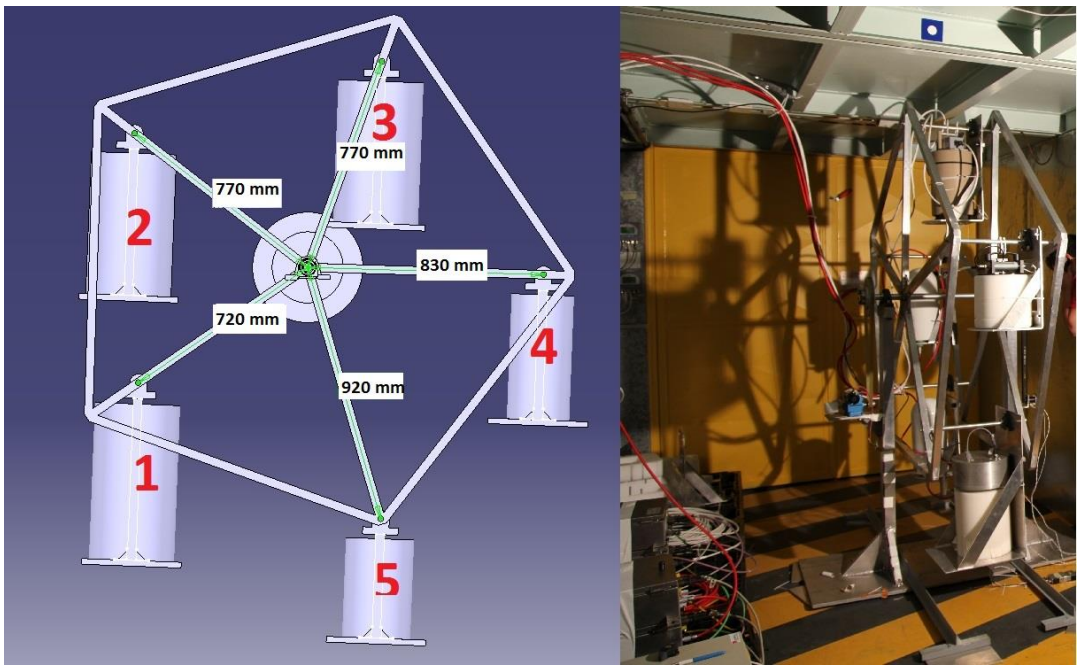


FIG. 17. Drawing (left) and picture (right) of the rotating structure installed at HiRadMat. The arbitrary numbers given to identify the positions are also shown.

Since the measurement area is located at the beginning of a bent tunnel which gives access to the facility, the neutron spectrum is extremely different from what exits the beam dump. In order to understand the different characteristics of the radiation stray field in the two areas FLUKA simulations have been performed to obtain the neutron spectrum in both areas. Fig. 18 and Fig. 19 show the simulated spectrum in a lateral position 2 m upstream the beam dump and in the measuring positions, respectively, together with the statistical uncertainties as derived from the simulations, the latter being higher for energies characterised by a very low neutron fluence.

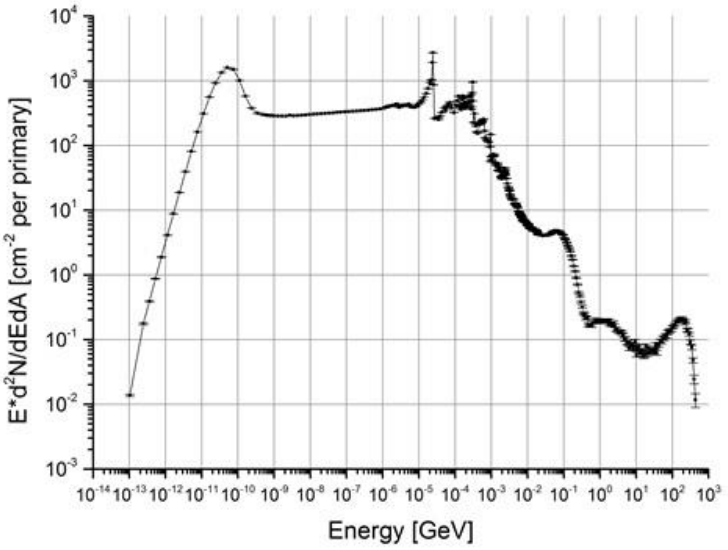


FIG. 18. Expected neutron spectrum, obtained via FLUKA simulations, 2 m upstream of the beam dump at HiRadMat, isolethargic view. The results are normalised per proton impinging on the dump.

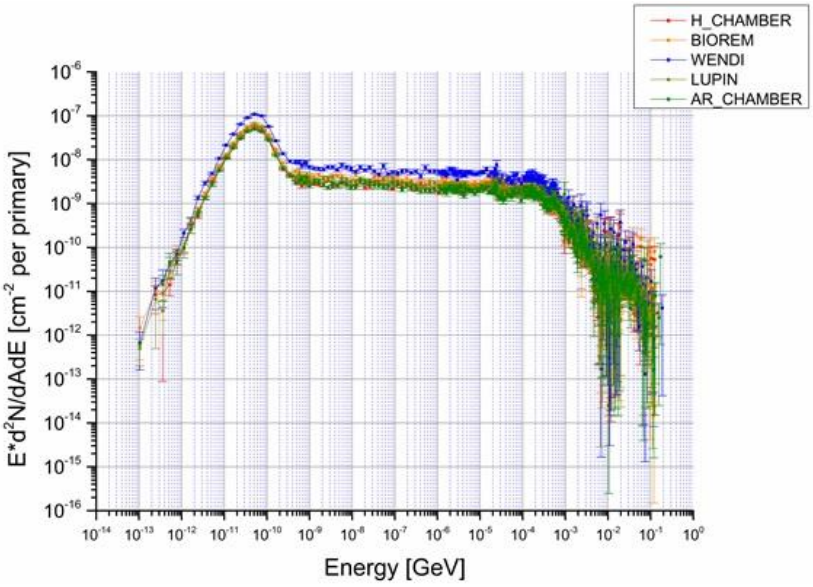


FIG. 19. Expected neutron spectrum, obtained via FLUKA simulations, in the measuring positions at HiRadMat, isolethargic view. The results are normalised per primary proton impinging on the dump.

The neutron spectrum close to the beam dump can be divided in six parts according to the neutron energy:

- a thermal peak generated by the neutrons which encountered a number of scattering events on the dump and on the tunnel concrete walls;
- an intermediate region from 10 eV up to 1 MeV;
- an evaporation component in the MeV region, caused by the particle-nucleus quasi-elastic interactions;
- a high-energy component above 10 MeV, which is due to the particle-nucleon high-energy interactions;
- a Maxwellian-shaped high-energy peak centred at about 100 MeV, an energy at which the (p,n) cross section value of the materials present in the facility show a minimum;
- a very high-energy peak, due to the backscattering of the high-energy neutrons produced in the dump. The tail of this peak reaches a maximum energy equal to the energy of the proton beam.

The thermal and evaporation neutrons are dominating the spectrum while the fluence integrated under the high-energy peak is three orders of magnitude lower. The high-energy neutrons produced in the dump are in fact forward peaked, while only a small fraction is backscattered at 180º, i.e. the angle at which the neutron spectrum has been scored. These backscattered neutrons continue travelling and scattering through the TNC, TJ7 and TA7 tunnels, see Fig. 16. This causes a huge modification in the spectrum which reaches the measuring area: the thermal component heavily dominates the spectrum whereas the neutrons produced in the dump have lost a significant fraction of their energy. Moreover, the majority of intermediate and high-energy neutrons backscattered from the dump follow a straight course and escape through the TJ7 and TJ6 tunnels. This explains the decrease of about six orders of magnitude in the total fluence and the strong reduction of the intensity of the evaporation peak at 1 MeV. Since the maximum energy of the neutron spectrum is well below 20 MeV, the response of the two rem counters employed in the measurements, BIOREM and Wendi-2, is approximately the same and can be compared without applying any correction factor. Fig. 20 shows the results obtained with the five detectors in position 1. The results were obtained by rotating five times the aluminium structure via a stepper motor in such a way the response of each detector could be compared in the same conditions. The results obtained in the other four positions are qualitatively very similar and do not add any

significant information, being the interest focused only on the loss of linearity of the detector response and not on the specific stray field conditions. The uncertainties are not shown in figure for clarity. The ideal behaviour of the detector response, i.e. the bisector of the first quadrant, is shown as a dotted line. For each detector a linear fit of the response is also given to guide the eye, especially in the low *H*(10)* region, where the points are widely spread due to the statistical uncertainty on the integrated number of counts.

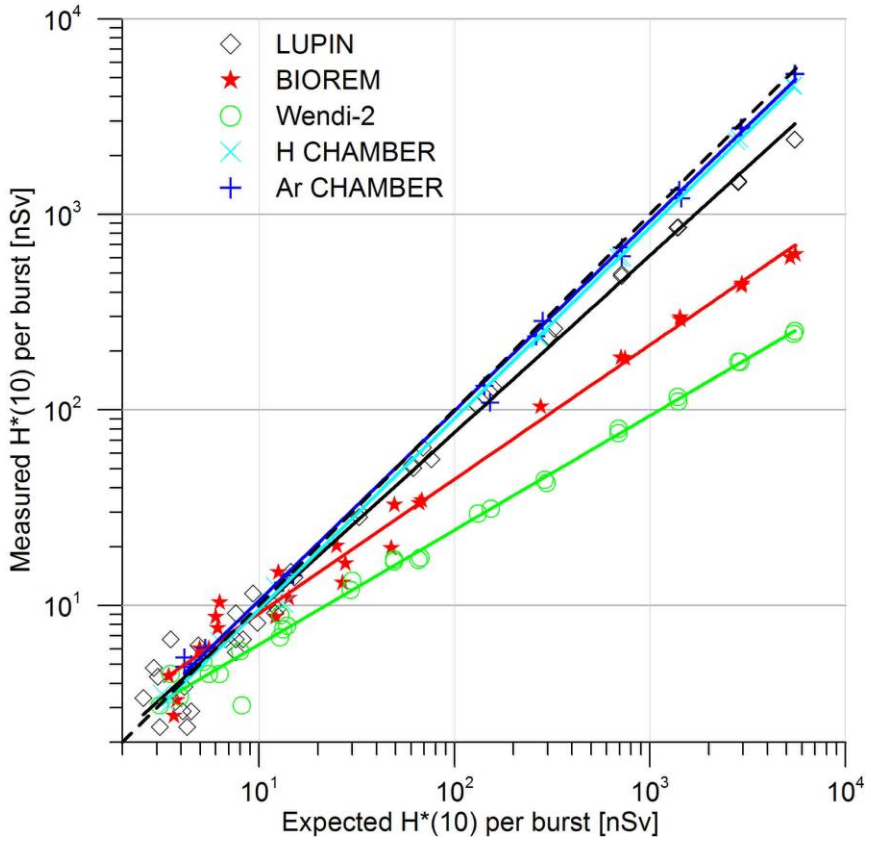


FIG. 20. Results obtained with the five detectors at HiRadMat, uncertainties not shown for clarity. The dotted line represents the ideal behaviour.

The response function is essentially linear over the entire *H*(10)* range for the Argon and Hydrogen-filled ionisation chambers, with a slight underestimation for values of expected *H*(10)* per burst higher than 1 µSv. For the other detectors the response is linear for low values of expected *H*(10)* and starts to saturate at higher intensities. The deviation from the ideal line is limited for LUPIN-BF, while it is of great importance for BIOREM and Wendi-2. Table VI shows the ratios between the measured and the expected *H*(10)* per burst averaged over the five positions for different values of expected *H*(10)* per burst. The ratios are not shown for values lower than 100 nSv per burst since the statistical uncertainties are too high to obtain a meaningful value.

Table VI. Ratio measured/expected *H*(10)* per burst for different values of expected *H*(10)* per burst obtained in the measurements at the HiRadMat facility.

| Detector | Expected *H*(10)* per burst | | | | | |
|---|---|---|---|---|---|---|
| | 100 nSv | 200 nSv | 500 nSv | 1 µSv | 2 µSv | 5 µSv |
| LUPIN-BF | 0.76 | 0.75 | 0.73 | 0.68 | 0.57 | 0.45 |
| BIOREM | 0.51 | 0.36 | 0.26 | 0.22 | 0.16 | 0.12 |
| Wendi-2 | 0.25 | 0.20 | 0.13 | 0.10 | 0.07 | 0.05 |
| Hydrogen chamber | 0.90 | 0.89 | 0.89 | 0.87 | 0.86 | 0.85 |
| Argon chamber | 1.00 | 0.98 | 0.97 | 0.97 | 0.97 | 0.96 |

The underestimation of the expected *H*(10)* is at maximum 4% for the Argon-filled chamber and 15% for the Hydrogen-filled chamber. The underestimation of LUPIN-BF is acceptable (< 30%) for expected *H*(10)* up to 1 µSv per burst, while for BIOREM and Wendi-2 it is already very important for 100 nSv: a factor of 2 for BIOREM and a factor of 4 for Wendi-2. At higher values of expected *H*(10)* the underestimation reaches one order of magnitude for BIOREM and Wendi-2, which cannot be considered reliable anymore, whereas for LUPIN-BF it is limited to a factor of 2. An example of a signal acquired with LUPIN-BF in position 1 with beam setting 13 is shown in Fig. 21. The acquisition window was set at 100 ms in order to include most of the signal due to scattered neutrons.

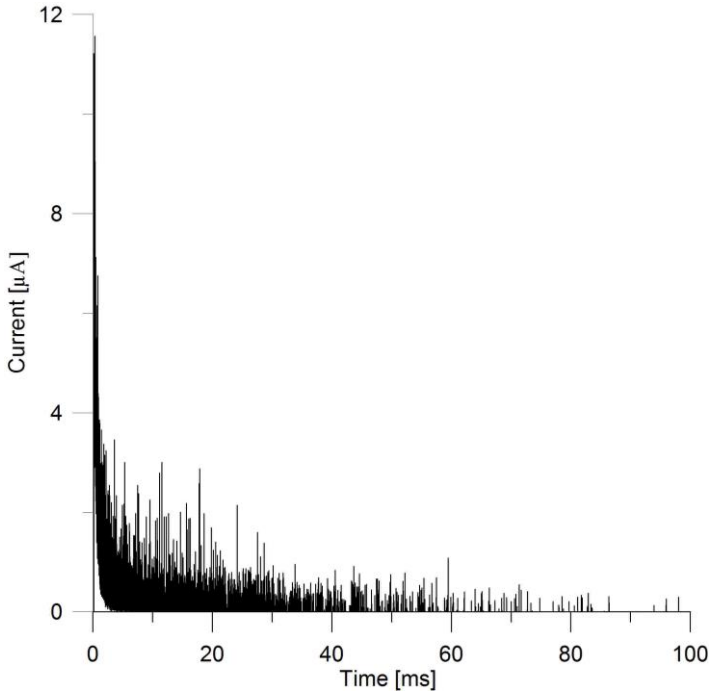


FIG. 21. Signal acquired with LUPIN-BF with beam setting 13 at HiRadMat.

The signal is spread out in 100 ms due to the multiple scattering events that the neutrons encountered along the tunnel structures. However, most of the charge is collected in the first few ms. Since the recorded signal is spread out in a time length much higher than the diffusion and thermalisation time of the neutrons in the detector moderator, the increase in intensity in the first tens of μs is not visible in the figure, as it was for the measurements performed at HZB, see Fig. 14, whereas in this case the first current peak is largely dominating the signal, reaching a maximum value of 12 μA. The rare peaks generated in the last part of the signal are due to neutrons, which underwent the highest numbers of scattering events. Given that the neutrons reaching the measuring area are mainly thermal, with a nominal speed of 2200 m/s, one can speculate that the neutron maximum path is about 220 m, i.e. 5 times the distance between the measuring area and the dump.

The measurements allowed comparing the performance of LUPIN-BF and four active neutron detectors usually employed in the CERN RAMSES system in stray field conditions characterised by an extremely high intensity per burst with a negligible photon component, but where a considerable fraction of the total *H*(10)* was due to scattered neutrons, degraded in energy due to the number of interactions that they encountered along the facility structures. The neutron spectrum which reached the area was evaluated via Monte Carlo simulations, which confirmed the possibility of comparing the results even with detectors characterised by different response functions to high-energy neutrons, i.e. conventional and extended range rem counters. The results provided a quantitative evaluation of the detector performance in these conditions, representative of what is usually found at the entrance of the access tunnels of radiation facilities or high-energy accelerators. This evaluation was especially focused on the deviation of the detector response from the linearity as a function of the expected *H*(10)* per burst.

According to their working principle, the detectors can be divided in three groups: ionisation chambers working in current mode, Argon and Hydrogen-filled; rem counters working in pulse mode, i.e. BIOREM and Wendi-2; LUPIN-BF. The slight underestimation of the ionisation chambers is caused by the incomplete ion collection caused by volume recombination, initial recombination and ion loss due to diffusion of ions to the collecting plates against the charge separating field. Among these processes only the losses due to volume recombination vary with measured *H*(10)* [Bohm 1976]. This is taken into account by the manufacturer, which foresees a possible maximum underestimation of the *H*(10)* of 15% when the ionisation chambers are dealing with a charge per pulse in the order of tens of

nC, i.e. what was detected for the highest intensities in this experiment [Latu 2007]. For the instruments working in pulse mode the underestimation is due to the dead time losses, that can become rather severe when high counting rates are encountered, as it was the case for this measurement campaign. The dead time value has been derived for the two detectors by applying the "two source method" [Knoll 2010b]. The obtained values are 1.0 ± 0.1 μs for BIOREM, very close to the TTL pulse width declared by the manufacturer, 1.2 μs [Thermo 2008], and 1.7 ± 0.2 μs for Wendi-2. This confirms the inverse proportionality between the observed underestimation and the dead time length. The underestimation observed in LUPIN-BF is due to the diminution of the gas multiplication factor of the proportional counter. Its quantitative evaluation will be treated in Section 2.3.

The solutions to be implemented in the ionisation chambers to extend their detection limit without being affected by any underestimation is to increase the voltage applied to the collecting electrodes and, if possible, increase the overall active volume. For the other instruments the solutions that could be adopted to extend their detection limits are the same described in the previous sections, i.e. a replacement of the acquisition electronics for the two detectors working in pulse mode with another one characterised by a lower TTL pulse width, and a larger active volume for LUPIN-BF. In conclusion, the measurement campaign confirmed the possibility of efficiently employing LUPIN in the extremely intense PNF typical of the entrance tunnels of high-energy particle accelerators, with maximum detection limits in the order of a few hundreds of nSv per burst, if no other complementary algorithms can be foreseen to compensate for the saturation effects.

### 2.2.5. Measurements in operational radiation protection conditions

A measurement campaign was performed with both versions of LUPIN and six active neutron detectors in selected locations around the CERN Proton Synchrotron (PS). The detectors employed in the campaign are used for routine measurements by the Radiation Protection group at CERN or are employed in the CERN RAMSES system. The attention was focused on the potential differences in the instrument readings due to dead time losses that are expected to affect most detectors in PNF. The aim of the measurements was to evaluate the response of LUPIN, compared to the other detectors, in three locations where the time structure of the losses is remarkably different and then to systematically intercompare their performance in a position where the radiation stray field is pulsed and very intense, i.e. where the highest pile-up effects and dead time losses are expected.

Fig. 22 shows a scheme of the PS complex, which is composed by 100 combined-function magnets arranged in a lattice and interleaved by 100 straight sections (SS).

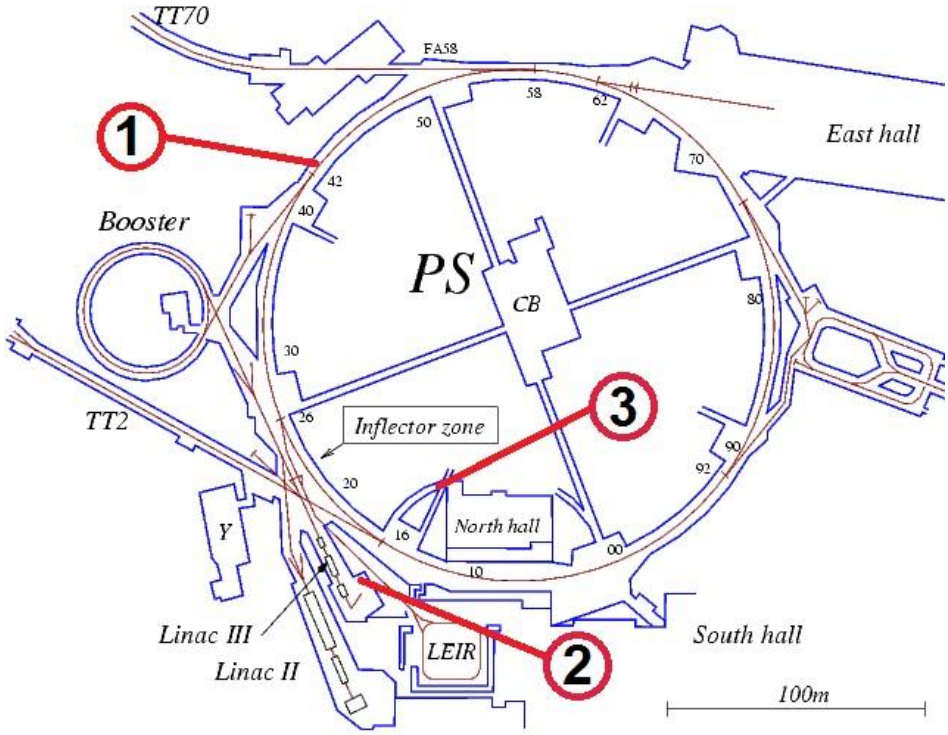


FIG. 22. The CERN PS accelerator complex. The small and big numbers identify some of the 100 straight sections and the three measuring locations, respectively.

During the measurements the proton beam used for the fixed target physics at the SPS was extracted from the PS at 14 GeV using the continuous transfer technique [Barranco and Gilardoni 2011]. In the extraction phase, comparatively large losses are observed all around the accelerator. These losses are due to particles scattered by the electrostatic septum used to slice the beam. The measuring locations were selected on the basis of the expected time structure of the losses in order to carry out the measurements in different stray field conditions:

- location 1, at ground level, on Route Goward, close to SS42 (beam injection); typical duration of the losses: 200-300 μs, smoothed by the ground shield (the street level is 6.4 m above the beam axis); fraction of lost beam: 1-5 %; in SS 42 the 1.4 GeV proton beam from the PS Booster is injected in the PS;
- location 2, inside the LINAC 3 building, close to SS16 (beam extraction); typical duration of the losses: 2.1 μs; fraction of lost beam: maximum 1%;

- location 3: at the beginning of the access tunnel to SS16 (beam extraction); typical duration of the losses: 2.1 μs; fraction of lost beam: 1%; the area is located at the accelerator level, just before an interlocked door.

In addition to the losses typical of each location, one has to consider that extraction losses are distributed on the overall PS and are always to be added up. These losses are due to the slicing process of the beam, which is extracted from the PS in five turns. Each of these turns lasts for 2.2 μs and the extraction losses have therefore a typical length of 11 μs. The pulse repetition rate is 0.83 Hz, i.e. one pulse every 1.2 s.

The instruments employed for the measurements were the following: both versions of LUPIN, two extended range rem counters, LINUS and Wendi-2, three conventional rem counters, LB6411, 2202D and BIOREM, and two Centronic IG5 ionisation chambers, filled with Argon and Hydrogen, see the Appendix for a detailed description of their main characteristics. The measurements were performed by installing the detectors in a reference location and by integrating the *H*(10)* for a period varying between 0.5 and 6 hours, in order to reduce at minimum the statistical uncertainty on the number of counts for the instruments working in pulse mode.

The measurements were performed in locations 1 and 2 with all detectors in parallel, by placing them close one to another. This was not possible in location 3 due to the high radiation gradient, where a more systematic intercomparison exercise was carried out. Six reference positions were selected along an interlocked door at the beginning of the access tunnel to SS16, whose width is approximately 4 m, see Fig. 23. Each position was 50 cm away from the adjacent one. The detectors were installed in a first configuration and then the positions were progressively interchanged in order to obtain a precise comparison of the responses in six slightly different conditions. During the measurements the same beam cycles were ran in the accelerator, thus assuring high reproducibility in terms of type, intensity and time structure of the losses. The measurements lasted 30 minutes for each configuration. The results were expressed in integrated *H*(10)* and normalised to the integrated proton fluence in the PS, as derived from TIMBER [Billen and Roderick 2006], a Java interface that allows obtaining data on the operation of the CERN accelerators in terms of settings, particle fluence and beam intensity. The results obtained with the conventional and the extended range rem counters can be compared without applying any correction factors because the maximum energy of the neutron spectrum in the area is well below 20 MeV. This will be shown in Section 4.3.2. via measurements performed with a neutron spectrometer.

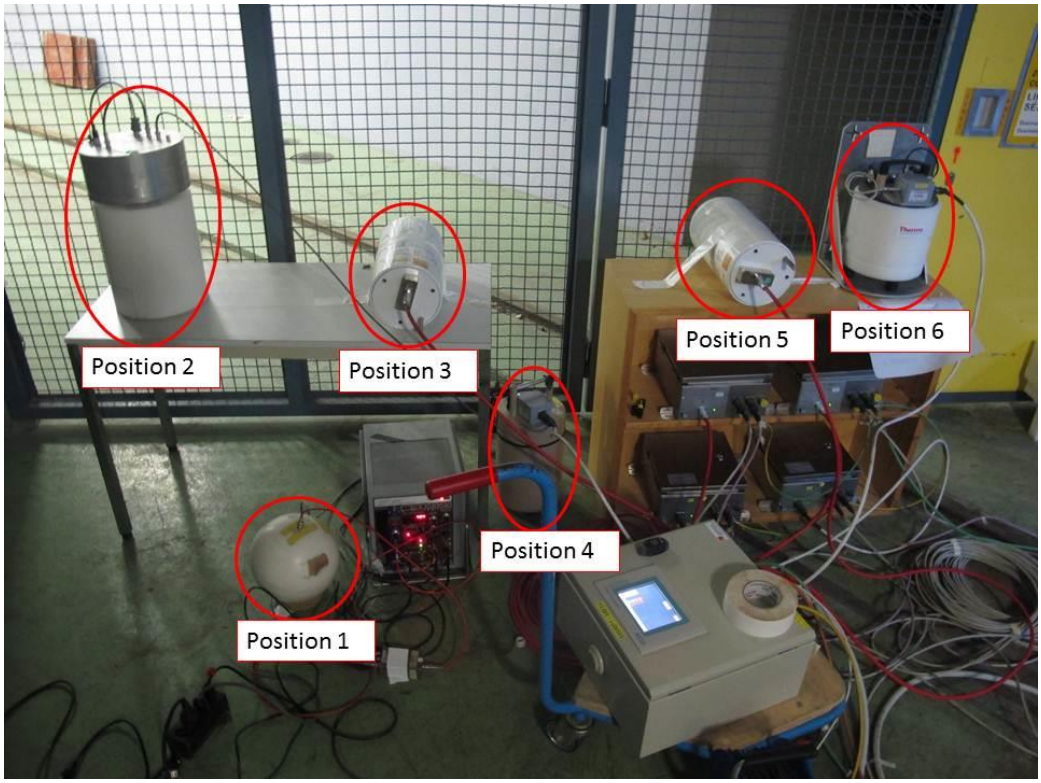


FIG. 23. Detectors installed in the six reference positions during the measurements performed at PS.

The results of the measurements are given in Table VII: for locations 1 and 2 the data did not need any normalisation because the measurements were performed in parallel in similar stray field conditions. The total uncertainty is the sum of the statistical (below 1%) and the positioning uncertainty (5%). The uncertainty on the calibration of the detectors has not been taken into account since it is a correlated uncertainty, as they have been all calibrated in the CERN laboratory by being exposed to the same PuBe source. The results of the measurement performed with Wendi-2 in location 1 are not available due to a malfunctioning of the detector. For the measurements carried out in locations 1 and 2 the 2202D and LB6411 were interchanged because of power issues with the first detector. LUPIN-He was employed in locations 1 and 2, whereas LUPIN-BF was used for the intercomparison exercise, since the latter is the version that should have the best performance in PNF, at observed in the measurements performed at HZB, see Section 2.2.3.

Table VII. Results of the PS measurements expressed as integrated *H*(10)* (locations 1 and 2, nSv) and as *H*(10)* normalised to the integrated proton fluence (location 3, nSv/$10^{13}$ protons).

| Detector | Location 1 | | | Location 2 | | |
|---|---|---|---|---|---|---|
| LINUS | 2310 (46) | | | 322 (17) | | |
| Wendi-2 | n.a. | | | 327 (18) | | |
| LUPIN-He | 2385 (26) | | | 326 (9) | | |
| 2202D / LB6411 | 1465 (38) | | | 240 (13) | | |
| Detector | Location 3 | | | | | |
| | Pos. 1 | Pos. 2 | Pos. 3 | Pos. 4 | Pos. 5 | Pos. 6 |
| LINUS | 9.4 (0.6) | 11.6 (0.7) | 10.6 (0.7) | 12.4 (0.8) | 10.4 (0.7) | 10.9 (0.7) |
| LUPIN-BF | 26.3 (1.5) | 34.7 (1.9) | 37.0 (2.1) | 36.5 (2.0) | 39.6 (2.2) | 31.9 (1.8) |
| H chamber | 21.7 (1.3) | 29.3 (1.7) | 34.8 (2.0) | 38.6 (2.2) | 31.2 (1.8) | 33.1 (1.9) |
| Ar chamber | 25.8 (2.0) | 36.3 (2.7) | 36.2 (2.6) | 37.2 (2.7) | 40.2 (2.9) | 43.4 (3.1) |
| BIOREM | 19.8 (1.2) | 23.0 (1.3) | 23.2 (1.3) | 24.8 (1.4) | 26.8 (1.5) | 22.0 (1.3) |
| Wendi-2 | 11.6 (0.7) | 12.6 (0.7) | 13.5 (0.8) | 12.5 (0.7) | 12.0 (0.7) | 11.9 (0.7) |

n.a. = not available

The results of the measurements carried out in location 1 show that the extended range rem counters, i.e. LINUS and LUPIN-He, have responses consistent within their uncertainties, while 2202D measures 30% less in terms of integrated *H*(10)*. As expected, due to the relatively long and smoothed time structure of the losses, the results are not affected by underestimation induced by dead time losses. This is confirmed by the fact that LINUS, which is characterised by a paralysable electronics, extremely sensitive to dead time losses, measures approximately the same value of LUPIN-He. The underestimation of 2202D can be explained by its low response for neutron energies below 20 MeV. The neutron spectrum expected in the area is in fact characterised by a peak at 80 MeV [Damjanovic et al. 2012]. The same effect can be observed for the measurements performed in location 2, where the spectrum is characterised by a high-energy peak. The conventional and extended range rem counters show different readings: approximately the same value for LINUS, Wendi-2 and LUPIN-He, but 30% less for LB6411. As for location 1, since the *H*(10)* rate in the area is very low, less than 1 μSv/h, the instrument readings do not show any considerable effect caused by dead time losses.

The results of the intercomparison performed in location 3 are shown in Fig. 24 for the six reference positions.

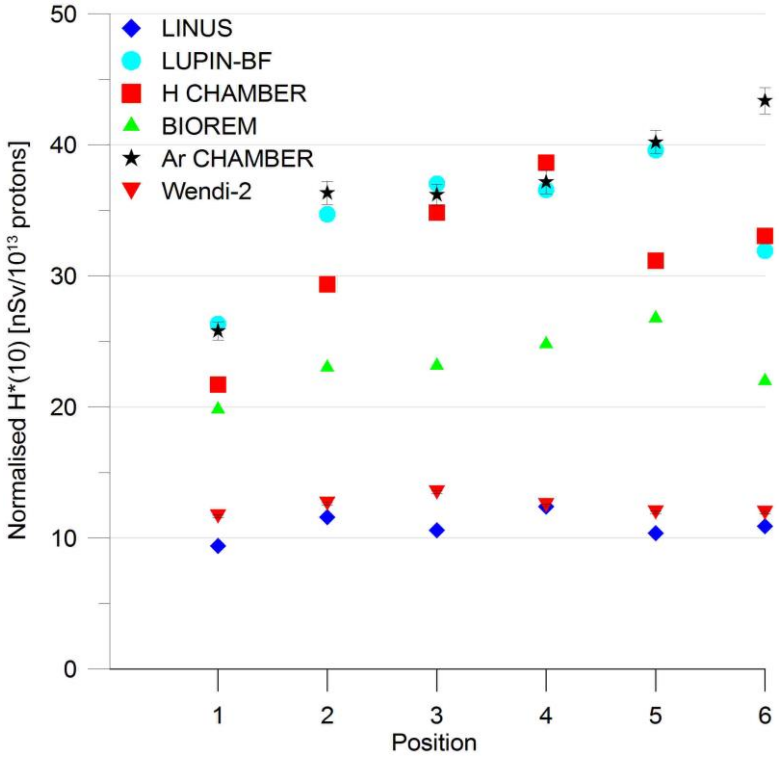


FIG. 24. Results of the intercomparison performed at PS in location 3, expressed as *H*(10)* normalised to the integrated proton fluence in the PS.

The results show that the detectors can be divided in three classes: the ionisation chambers and LUPIN-BF; BIOREM; LINUS and Wendi-2. The readings of the first class of detectors agree well within their range of uncertainties and are coherent with the FLUKA simulation results given by ref. [Damjanovic et al. 2012], i.e. an expected *H*(10)* of 20-40 nSv per $10^{13}$ protons accelerated in the PS. This calculated range spans over a factor of 2, because the value has been normalised to the protons lost in the machine, by assuming 1% of beam losses in the extraction point, whereas the actual lost fraction can substantially vary according to the different beam cycles. The underestimation of BIOREM is around 30% if we take as reference the mean *H*(10)* value measured by the first class of the detectors. The third class measures a value about 60% lower. To understand if the dead time losses can explain these underestimations one has to first estimate the true interaction rate and the intrinsic dead time of the two classes of detectors and then introduce these values in equation (1). The dead time of BIOREM and Wendi-2 are about 1.0 μs and 1.7 μs, respectively. The true interaction rate can be derived from the signal acquired with LUPIN in location 3, see Fig. 25.

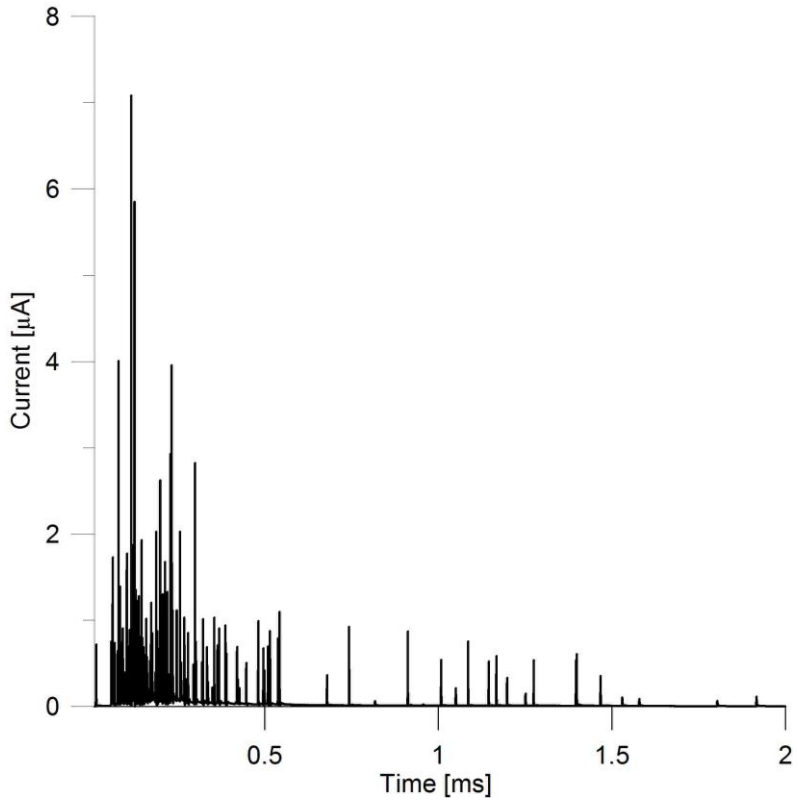


FIG. 25. Signal acquired with LUPIN-BF in location 3 at PS.

The signal is composed by a first part of 0.5 ms duration, where most of the neutron interactions are concentrated. The trend in time of this first part of the signal is governed by the thermalisation and diffusion time of the neutron in the detector moderator and the interaction rate is about $8.3 \cdot 10^5$ $s^{-1}$. This is the value to be taken into account for estimating the dead time losses, since the second part of the signal shows relatively rare interactions generated by neutrons that encountered scattering events against the walls of the access tunnel, which is approximately 40 m long. By taking this into account, the dead time losses can be estimated to be 45% for BIOREM and 62% for Wendi-2. The observed underestimations are slightly lower, but this could be due to the fact that a part of the acquired signal is due to scattered neutrons, which are detected up to few ms after the first interaction. The calculated underestimation is in fact conservative since it takes into account the estimated interaction rate in the first 0.5 ms, which is clearly different from the average interaction rate on the entire acquisition window.

The measurements allowed comparing the behaviour of both versions of LUPIN and of six active neutron detectors employed in the CERN RAMSES system in operational radiation protection conditions. The tests were performed in several radiation environments, with a typical time structure of the losses which was varying remarkably according to the different accelerator loss point. In the main

intercomparison exercise, performed in one of the most critical loss point of the entire PS, the neutron spectrum was not characterised by any high-energy component and this allowed performing a direct comparison of the performance of the instruments, regardless from their sensitivity in the high-energy range.

The comparison of the results obtained in the intercomparison exercise allowed dividing the detectors in three classes according to their dead time:

- detectors not working in pulse mode, and therefore not characterised by any dead time, i.e. the ionisation chambers and LUPIN;
- instruments characterised by a 1 μs dead time;
- detectors with a dead time of about 2 μs.

As expected, conventional rem counters underestimate the *H*(10)* by about 30% with respect to the extended range ones, when working in a stray field characterised by a high-energy peak; extended range rem counters agree well amongst them and with the reference FLUKA value when exposed in a non-pulsed high-energy field; all rem counters apart from LUPIN showed important dead time losses when exposed to PNF, which lead to consistent underestimations varying between 30% and 60%; LUPIN showed results coherent with the ionisation chambers and with the FLUKA values in all measurement locations.

The good performance shown in these different operational conditions by LUPIN is an indicator of its possibility to be employed as an *H*(10)* meter in the loss points of the CERN accelerators both as a portable detector for routine surveys and as a fixed monitor to be implemented in the radiation monitoring system. It could be efficiently employed to measure the background radiation during the accelerator shutdown, as well as in the most severe conditions and in the critical loss points when the accelerator is running. Its performance is similar to the one of the ionisation chambers, which work in current mode and are therefore intrinsically not characterised by dead time losses, but it shows many other advantages:

- it is a relatively light and portable instrument, whereas ionisation chambers require special cables and several electronics modules to transport and analyse the low current signal;

- it works with a single calibration factor, which is valid in all conditions, whereas ionisation chambers need a proper conversion factor to be set up for each radiation environment, see Appendix for more details about their operation mode;
- as opposed to ionisation chambers, LUPIN is not limited in its transport by safety constraints, which are a direct consequence of the pressurisation of the internal gas, especially for the Hydrogen case.

### 2.2.6. Neutron/photon discrimination in steady-state fields

The capability of efficiently discriminating a neutron from a photon signal is a desirable property in a neutron detector, since neutron fields are usually accompanied by a non-negligible photon component. This issue is solved in proportional counters by discriminating the amplified signal which enters the SCA on the basis of its height. Photons may in fact interact in the counter walls and create secondary electrons that subsequently ionise the gas and lead to the collection of ions and electrons on the detector electrodes. However, because the stopping power for electrons in gases is low, an electron will deposit only a small fraction of its energy in the counter. Therefore the photon-induced interactions can be easily discriminated by the neutron-induced ones by setting a proper lower threshold: the SCA will generate a TTL signal as an output to be transmitted to the counter only if the incoming signal peak is higher than the threshold. This discrimination technique is efficient in steady-state mixed fields, whereas in mixed pulsed fields the photon interaction rate can be high enough to generate pile-up interactions, which lead to a total energy deposition comparable to the energy deposited by the neutron-induced reaction products. This case will be treated in detail in Section 2.2.7. Due to the special working principle of LUPIN this discrimination technique is only applicable for determining the MCC in the calibration process (see Section 2.2.1.), whereas during normal operation another discrimination technique must be put in place. If the standard acquisition mode of LUPIN is used, the charge indirectly deposited by the photons would be taken into account for the calculation of the total deposited charge and, as a consequence, for the calculation of the total number of neutron interactions. However the energy deposited by the secondary electrons in the gas usually represents a negligible fraction of the charge deposited by the neutron-induced reaction products. The standard neutron/photon discrimination technique applied in the LUPIN acquisitions, which will be called from now on for simplicity technique D1 (discrimination 1), is based on the subtraction from the acquired signal, for the calculation of the total number of interactions, of a background current averaged over the samples acquired in the 10 μs

before the beginning of the acquisition, the so-called pre-trigger samples. Fig. 26 shows the concept at the basis of this technique.

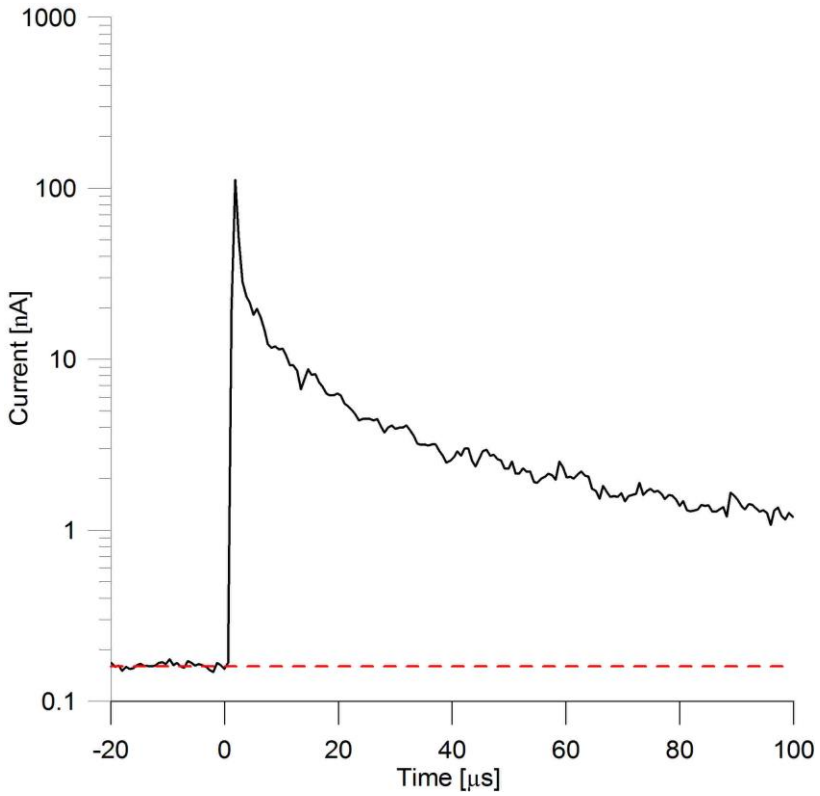


FIG. 26. Principle of the neutron/photon discrimination technique D1 applied in LUPIN.

This allows subtracting the contribution of the photon component of the stray field to the total charge. Technique D1 is efficient when the photon background has a moderate importance but also in case of negligible background: it allows in fact subtracting the value of the fixed current of 160 pA, whereas it cannot work with high background, due to heavy fluctuations of the current signal. A technique D2 has been developed to face situations of high background, where the photon-induced charge deposition in the detector is high if compared to the neutron-induced one, in order to subtract from the total charge the contribution of the charge deposited by the secondary electrons. The efficiency of technique D2 have been studied by reproducing these conditions at the Italian National Centre for Accreditation (ACCREDIA) located at the *Politecnico di Milano*.

LUPIN-BF was exposed in a mixed neutron/photon field generated by a $^{137}$Cs and an AmBe source. The $^{137}$Cs source was installed in an irradiator and LUPIN-BF was placed in a reference position located 2 m away from the source. The photon *H*(10)* rate in this position was equal to 25 mSv/h, but it rapidly went down to about 1 μSv/h by closing a shutter embedded in the irradiator. At the same time

a portable AmBe source was placed at 1 m from LUPIN-BF in order to detect a neutron interaction rate of about 10 $s^{-1}$. The acquisition time was set to 10 ms. This radiation environment resembles a situation in which the detector is exposed to a low intensity neutron field accompanied by an intense photon background. Thanks to the shutter and the portable neutron source, the stray field was easily changed from a situation with negligible photon field to the conditions of mixed neutron/photon field described above. The results and the applications of the discrimination technique are shown here for LUPIN-BF but are also valid for LUPIN-He.

If LUPIN-BF is employed in this radiation environment with its standard acquisition method, the charge deposited in the gas by the secondary electrons heavily overcomes the charge deposited by the products of the neutron-induced reactions. This is because the detector is integrating the total charge and cannot discriminate its origin. This can be observed by evaluating the detected interaction rate when the detector is exposed to the neutron field only or to the mixed field. Two acquisitions of about 30 minutes each were performed in both conditions. Two tests were carried out in the first case and the detected interaction rate was 19.4 ± 4.4 $s^{-1}$ and 20.5 ± 4.5 $s^{-1}$. When the shutter was opened the effect of the photon field immediately increased the background current from its design value of 160 pA, see Section 2.1, to a value fluctuating around 400 pA. The tests carried out in the second case gave a detected interaction rate of 495 ± 22 $s^{-1}$ and 496 ± 22 $s^{-1}$.

In these conditions technique D1 cannot be efficiently applied due to the huge fluctuations of the current baseline signal that do not allow a stable average value to be determined in the 10 μs before the beginning of the acquisition. Technique D2 is based on the concept that, in a radiation environment characterised by a low neutron field and a high photon background, LUPIN will acquire for most of the time charge indirectly generated by photons. The idea is to integrate the charge only in the small fraction of time in which the neutron interactions are detected. This could be done in principle by setting a proper trigger on the current level. However, several tests showed that when the photon stray field is very intense the fluctuations are extremely important and could easily overcome a trigger level set to low current values. On the other hand, if the trigger value is set to high values, a considerable fraction of the products of the neutron-induced reactions would not be acquired, especially in the case of important wall effects, where the deposited charge falls in the low part of the charge spectrum, see Fig. 5 and Fig. 6. However the signal indirectly generated by photons has a very small increasing slope if compared to the neutron-induced one, which usually reaches its peak in tens of μs. This suggested

the idea of setting a trigger on the derivative of the current signal. A small modification has been introduced in the acquisition interface in order to calculate the derivative of the original current signal, which is defined as follows:

$$\frac{dI_n}{dt} = \frac{1}{2\delta t}(I_{n+1} - I_{n-1}) \quad , \tag{2}$$

where $I_{n-1}$, $I_n$ and $I_{n+1}$ are the current values of the samples n-1, n and n+1, respectively, and δt is the time delay occurring between the acquisition of one sample and the following, which is determined by the sampling frequency. During the measurements the sampling frequency was 10 MHz, which means a δt of 100 ns. A trigger level is set on the derivative signal and the total number of neutron interactions is determined via a peak detection analysis. This was performed via a function embedded in the LabVIEW program but it could be performed with any other acquisition interface, since its operating principle is simple and based on two steps:

1) the acquisition starts when the current derivative exceeds a trigger value, conveniently set by the user;
2) in order for the acquisition to be counted as a neutron interaction, the derivative value must stay higher than the trigger value for a certain number of samples, as defined by the user.

For the measurements performed at the *Politecnico di Milano* the trigger was set to 0.5 mA/s and the minimum number of samples above the trigger value in order for the acquisition to be recognised as a neutron interaction was set to 10. The efficiency of technique D2 was tested by exposing LUPIN-BF first to the AmBe source only and then to the AmBe and the $^{137}$Cs sources contemporaneously. Two 30 minutes tests were performed in the first case and the detected interaction rate was 19.6 ± 4.4 $s^{-1}$ and 20.8 ± 4.6 $s^{-1}$. The tests carried out in the second case showed an interaction rate of 19.4 ± 4.4 $s^{-1}$ and 20.5 ± 4.5 $s^{-1}$, thus compatible within the range of uncertainties with the first case. This confirmed the efficiency of technique D2, which allowed a complete rejection of the photon background. In this situation the background was due to the 662 keV photons emitted by $^{137}$Cs via the transition to the ground state of the $^{137m}$Ba isotope.

Techniques D1 and D2 described in this section allow LUPIN to efficiently operate in presence of a steady state photon background by discriminating the photon from the neutron-induced signal in the proportional counter. Technique D1 can be applied in situations of low or moderate background,

whereas technique D2 can be employed in situations of extremely high photon background. The peculiarity of technique D2 is that it reverts LUPIN into a detector operating in pulse mode, with the difference that the trigger level is set on the derivative of the current signal. The reliability of the two techniques has been tested via measurements performed in mixed neutron/photon fields which showed that the photon background can be completely discriminated from the neutron interactions, even when the neutron interaction rate in the detector is very low. The techniques have been implemented in an acquisition software written via the LabVIEW program, but their simplicity allow them to be easily implemented, if needed, in any other acquisition interface. The only difficulty lies in the selection of the best discrimination technique to be adopted in a given radiation environment. However, since the user usually knows the main characteristics of the radiation field before performing the measurements, the best discrimination technique can be easily selected with limited *a priori* information. As a matter of fact, technique D1 works extremely well in most typical conditions, whereas technique D2 finds application only in rare conditions, where the neutron detection would be almost unfeasible with any other active instruments.

### 2.2.7. Neutron/photon discrimination in pulsed fields

As mentioned in Section 2.2.6. a special discrimination technique must be adopted when LUPIN is exposed in mixed pulsed fields. Techniques D1 and D2 cannot in fact work properly in case of a background photon field characterised by a pulsed structure, which can produce in the proportional counter a charge equivalent to many neutron interactions. This is a typical radiation environment found around particle accelerators operated with pulsed beams, operating for both scientific and medical purposes. Technique D3 is based on the principle that photons do not need to be thermalised before interacting in the proportional counter, whereas neutrons need a thermalisation and diffusion phase in the moderating assembly in order to reach an energy at which the reaction cross section in the gas is sufficiently high. Assuming that the photons that accompany the neutron field reach the surface of the moderator at the same time of the neutron component, they interact in the proportional counter in the following hundreds of ns, whereas the thermalisation and diffusion process needed for neutrons introduces a minimum delay of few μs, with a variation of the thermal population characterised by an exponential decay whose constant is in the order of 100 μs. Moreover, if both the photon and the neutron component of the field are pulsed, the release of the charge due to the photons ends few μs after its arrival on the detector surface, whereas the neutron contribution ends after several hundreds of μs. For

the calculation of the number of neutron interactions technique D3 takes into account only the charge released in the proportional counter at least 5 μs after the beginning of the acquisition, which is controlled by setting a trigger level on the current signal. The charge collected in the first 5 μs is not considered for determining the number of neutron interactions since it can be attributed to the photon field. A small number of neutron interactions is nevertheless detected in the first μs: this can be due to thermal neutrons that did not interact in the moderating assembly or to fast or intermediate energy neutrons that induced a reaction in the gas even if the reaction cross section exponentially decreases for energies above the thermal one.

In order to verify the reliability of technique D3 measurements have been performed in radiation environments with conditions similar to the ones described above: the first campaign was performed at the *San Raffaele* hospital in Milan, where LUPIN-He was installed close to an electron LINAC operating at 18 MV in order to detect the secondary neutrons originated by the photons interactions in the accelerator structures; the second series of measurement was carried out at the Paul Scherrer Institute in Villigen (Switzerland) around the injector test facility which serves as the principal test and demonstration plant for the Swiss Free Electron Laser (SwissFEL) project [Pedrozzi 2010].

In the first case LUPIN-He was exposed out-of-beam in two reference positions on a treatment couch, at a distance of 32 cm and 100 cm from the beam isocentre, while the electron beam was impinging on the couch itself with an intensity of 400 M.U. per minute, an irradiation field of 5 x 5 $cm^2$ and was operating at 18 MeV, i.e. well above the energy threshold of 7 MeV needed to have a considerable photoneutron production in the accelerator structures. The LINAC used for the measurements was a Varian Clinac™ DHX Dual Energy. The LINAC was operating at a frequency of 182 Hz and a burst length of about 1.5 μs. The signals detected by LUPIN-He with an acquisition window of 500 μs are shown in Fig. 27 for both reference positions.

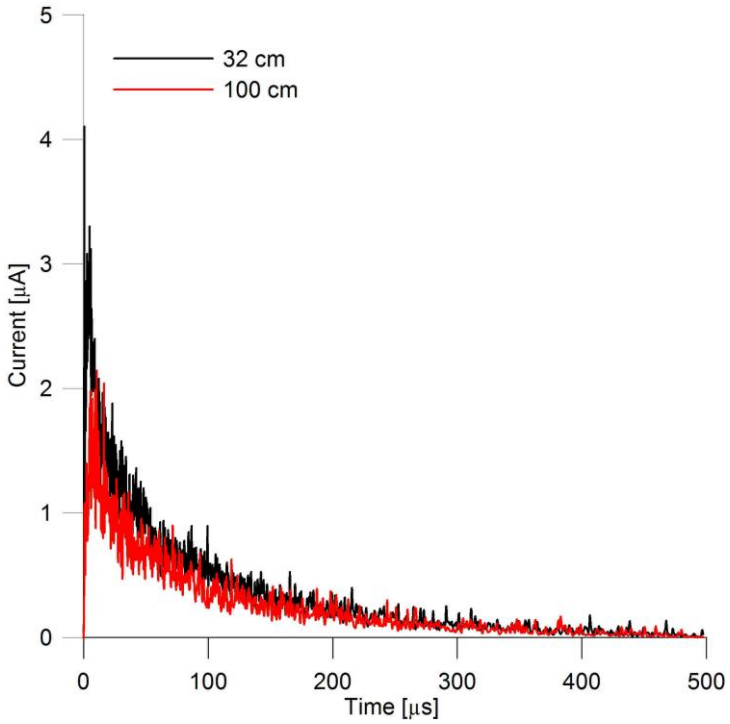


FIG. 27. Signals acquired with LUPIN-He in both reference positions around the medical LINAC at the *San Raffaele* hospital.

The signal shows a prompt peak after 1 µs, which is due to the photon interactions, whereas the neutron signal is characterised by a rapid increase and a subsequent exponential decay, which ends after approximately 500 µs. The small and periodic fluctuations of the signal are due to an internal modulation of the accelerator coming from noise produced by the motors of the multileaf collimators. Technique D3 can be efficiently applied in this radiation environment because the photon contribution is clearly limited to the first few µs, whereas in the same time window the signal that can be attributed to neutron interactions is negligible, conservatively assumed equal to few neutron interactions. A further confirmation that the charge integrated after the first 5 µs is due to neutron-induced reactions only is given by the fact that the *H*(10)* integrated in the signal in the two reference positions, i.e. 582 nSv at 32 cm and 226 nSv at 100 cm, is compatible with the value of *H*(10)* expected from the production of secondary photoneutrons in this condition, i.e. in the order of one thousandth of the dose released to the tumour in the isocentre, as it can be found in literature, see for example [Barquero et al. 2002, Vanhavere et al. 2004, Domingo et al. 2010].

In the second case LUPIN-BF was used to measure the neutron *H*(10)* in 12 reference positions along the injector test facility of the SwissFEL, see Fig. 35 below, in the view of its employment as BLM for the future facility, as it will be comprehensively discussed in Section 3.2.2.

The accelerator was operating at 230 MeV with a repetition rate of 10 Hz. The bunch length was a few ps, with a charge of 200 pC each, corresponding to about $10^9$ electrons per bunch. The beam was stopped in a dump consisting of a steel block shielded by concrete. An example of the signal acquired with LUPIN-BF in one of the reference position is shown in Fig. 28.

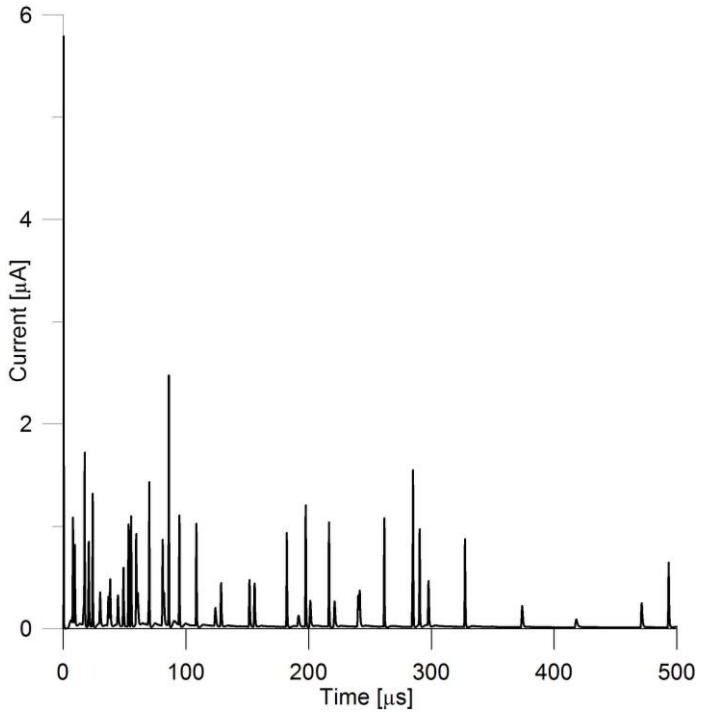


FIG. 28. Signal acquired with LUPIN-BF at the test injector facility at PSI.

As expected, due to the extremely short length of the electron bunches, the first part of the signal is dominated by a prompt photon peak, whereas the neutron produced in the particle interaction with the accelerator structures are characterised by a minimum delay of about 10 μs. In this case the typical exponential decay which governs the variation in time of the thermal neutron population in a moderating assembly is not visible due to the low neutron interaction rate. Technique D3 can be efficiently applied since the prompt photon peak triggers the acquisition, while the charge integration starts with a delay of 5 μs, thus completely excluding the photon contribution. The neutron interactions in the first 5 μs are completely absent due to the low interaction rate. The reliability of technique D3 was evaluated via a statistical method: the $\chi^2$ test [Knoll 2010a] was applied off-line to the data obtained in several acquisitions with conditions similar to the one showed in Fig. 28. The number of neutron interactions detected in each acquisition has been verified to be a Poisson-distributed random variable, thus confirming that the residual charge obtained by neglecting the first 5 μs of the acquisition can be attributed to neutron interactions only.

Technique D3 allows LUPIN to efficiently operate even in conditions of mixed photon/neutron pulsed fields, by mean of a simple time based discrimination method. This peculiarity makes LUPIN capable to be employed as radiation protection monitor or as a detector for beam diagnostics in particle accelerators characterised by short bunches or high intensity beams. At the state of the art technique D3 is applied via the LabVIEW program, but, due to its simplicity, it could be implemented in other acquisition interface. Moreover, unlike technique D2, its implementation in the acquisition process does not need to be determined on an *a priori* information on the radiation environment, because, even in absence of an important photon contribution, the suppression of the charge acquired in the first 5 μs does not introduce considerable differences in the calculation of the number of neutron interactions.

### 2.3. Correction of the space charge effect

As observed in some of the measurements campaigns described in the previous sections, notably in Sections 2.2.3 and 2.2.4, even if both versions of LUPIN are working with a special operation mode that avoids the limitations usually related to the presence of a dead time, an appreciable underestimation of the neutron *H*(10)* can be still be observed for extremely intense neutron bursts. Since this cannot be correlated to dead time losses, its origin must be found in another physical effect, i.e. the reduction of the multiplication factor of the proportional counter. This reduction is caused by the space-charge shielding of the externally applied electric field, in turn caused by the charges produced during a neutron burst in the gas. In order to fully understand the causes of this effect and to quantify it for LUPIN, the discussion has to start from some basic concepts of the theory of electron gas multiplication in proportional counters.

The electric charge generated by a neutron interaction in a proportional counter depends on the energy deposited by the reaction products in the gas through ionisation. As mentioned in Section 1.1., the energy imparted to the reaction products both in the case of an $^{3}He$ or a $BF_3$ proportional counter is essentially equal to the Q-value of the reaction induced by the neutron in the gas. This is equal to 764 keV for the $^{3}He(n,p)^{3}H$ reaction and 2.310 MeV or 2.792 MeV for the $^{10}B(n,\alpha)^{7}Li$ reaction, depending the $^{7}Li$ atom is left in its excited or ground state, respectively. The reaction products ionise the gas and produce a number of electrons and positive ions, which is proportional to their energy and depends on the average energy needed to produce an electron-ion pair in the gas, also called the energy dissipation per ion pair or W-value. The deposited energy is equal to the Q-value only when the particles can deposit their entire energy in the gas without colliding with the

detector walls. This corresponds to the absence of the so called wall effect and results in the peaks of the spectra shown in Fig. 5 and Fig. 6. The W-value is substantially greater than the gas ionisation potential because the reaction products lose their energy in the gas not only via ionisation processes but also via other mechanisms that do not contribute to the production of electron-ion pairs, such as, for example, excitation processes. The W-value depends on the energy and the type of the radiation involved, and on the physical properties of the gas, and it usually varies between 25 and 40 eV for most proportional counters. If Θ is the energy imparted to the reaction product and W is the gas W-value, then the maximum number of electron-ion pairs $n_0$ initially created in the gas, in case of negligible wall effects, can be estimated as

$$n_0 = \frac{\Theta}{W} \quad . \tag{3}$$

The total charge eventually generated by these original $n_0$ pairs is dependent on the multiplication factor characteristic of the proportional counter. If M is the multiplication factor and e is the electron charge, then the total generated charge Q is equal to

$$Q = n_0 \cdot e \cdot M \quad . \tag{4}$$

If we assume that all the charge generated in the gas is collected on the detector electrodes, the total number of neutron interactions N can be calculated for LUPIN as:

$$N = \frac{Q}{MCC} \quad , \tag{5}$$

where MCC is the mean collected charge, obtained via the calibration process described in Section 2.2.1. From now on the assumption is made that the proportional counter has a cylindrical geometry, like in the case of the $BF_3$ counter used in LUPIN-BF. However, all the concepts and the conclusions made on the basis of the following calculations are qualitatively valid even for a spherical geometry, as it is the case for the $^3$He counter used in LUPIN-He. If we assume that the multiplication process in the gas happens through electron collisions only, thus neglecting any photoelectric effect, and that no electron is lost for negative ion formation, than the multiplication factor M can be expressed

as the solution to the Townsend equation, which governs the avalanche formation [Knoll 2010c], for a cylindrical geometry:

$$\ln M = \int_{E(a)}^{E(r_C)} \alpha(E) \frac{dr}{dE} dE \,, \tag{6}$$

where E(r) represents the absolute value of the electric field in position r, calculated as the radius from the centre of the anode wire, $r_C$ is the critical radius beyond which the electrical field is too low to support further gas multiplication, a is the anode radius and α(E) is a function which depends from the gas type and the magnitude of the electric field. The integral is calculated from the surface of the anode wire, i.e. from r = a, to the maximum distance from the anode wire where the electric field is high enough to still support the multiplication process, i.e. up to r = $r_C$. The expression of α(E) is quite complicated and several options are given in literature, but all of them agree on the fact that it is directly proportional to the electric field E. This assumption is sufficient for the aim of this discussion. Then, by introducing the expression of the electric field in cylindrical geometry in equation (6) and by assuming that α(E) shows a directly proportionality from E, one obtains the following expression for the multiplication factor M:

$$\ln M = \frac{\ln 2 \cdot V}{\ln\left(\frac{b}{a}\right) \cdot \Delta V} \cdot \ln\left( \frac{V}{K \cdot p \cdot a \cdot \ln\left(\frac{b}{a}\right)} \right), \tag{7}$$

where V is the applied voltage, b is the cathode radius, p is the gas pressure, K is the minimum value of E/p below which the multiplication process cannot be supported and ΔV corresponds to the potential difference seen by an electron as it moves between successive ionisation events. K and ΔV are constant values for both gas mixtures employed in the $BF_3$ and $^3He$ counters used for LUPIN.

Equation (7) is valid for proportional counters employed in typical radiation environments. The problem arises when they are employed in extremely intense PNF, like in the measurement campaigns described in Sections 2.2.3 and 2.2.4. During the neutron burst we can assume that a neutron interaction happens in the detector immediately after the previous one. If the second neutron interaction happens in the gas while the ions generated in the first interaction are not yet collected on the cathode, then there is an area in the gas with a net positive space charge. This charge screens the electric field,

thus reducing the multiplication factor and, consequently, the total collected charge. It must be noted that the contribution of electrons, which are mostly generated close to the anode and whose collection speed is 1,000 times longer than ions, is limited to the very beginning of the signal, whereas the biggest contribution is due to the migration of the slow positive ions towards the cathode. As a consequence, the LUPIN *H*(10)* underestimation is proportional to the interaction rate.

In order to quantify the screening effect generated by the net positive charge in the gas, which results in the reduction of the multiplication factor, one has to analyse the problem of depositing a given charge density ρ during the neutron burst. This charge density can be calculated as:

$$\rho = n_0 \cdot M \cdot \frac{N_i}{v}, \tag{8}$$

where $N_i$ is the number of neutrons interacting in the burst and *v* is the detector active volume. A comprehensive explanation of how to derive the dependence on the variation of the electric field on the charge density induced by the neutron interactions in the burst is given in ref. [Rios et al. 2013]. For the aim of this discussion only the final results of the analysis are reported. The conclusions are that, assuming that all positive ions are generated close to the anode wire in the region where r << b, the effective change in the potential is given by the following expression:

$$\delta V = \frac{\rho e b^2}{4\pi\varepsilon_0}, \tag{9}$$

where $e = 1.6 \cdot 10^{-19}$ C is the electron charge and $\varepsilon_0 = 8.854 \cdot 10^{-12}$ F/m is the electrical permittivity of free space. This must be introduced in equation (7) in order to obtain the value of the reduced multiplication factor M' which takes into account the reduction of the electric field generated by the presence of a net positive charge:

$$\ln M' = \frac{\ln 2 \cdot (V - \delta V)}{\ln\left(\frac{b}{a}\right) \cdot \Delta V} \cdot \ln\left(\frac{V - \delta V}{K \cdot p \cdot a \cdot \ln\left(\frac{b}{a}\right)}\right). \tag{10}$$

In order to express the value of the reduced multiplication factor M' as a function of the number of neutrons interacting in the burst, one has to introduce expression (8) in (9) and expression (9) in (10).

In order to further simplify the mathematical expressions, three functions B, C and D can be defined as follows:

$$B = \frac{\ln\left(\frac{b}{a}\right)\cdot\Delta V}{\ln 2}, \tag{11}$$

$$C = K\cdot p\cdot a\cdot\ln\left(\frac{b}{a}\right), \tag{12}$$

$$D = \frac{\Theta}{W}\cdot\frac{eb^2}{v\cdot 4\pi\varepsilon_0}. \tag{13}$$

The expression for the reduced multiplication factor M' then becomes:

$$M' = \frac{1}{\exp\left[-\frac{V}{B}\cdot\ln\left(\frac{V}{C}\right)\right]+\frac{D}{B}\cdot N_i\cdot\left[1+\ln\left(\frac{V}{C}\right)\right]}, \tag{14}$$

from which it is clear that as the number of neutron interactions in the burst $N_i$ increases, the reduction in the multiplication factor becomes more important. For the aim of this study it is also convenient to express equation (7) in a simpler form by profiting from functions B, C and D:

$$M = \exp\left[\frac{V}{B}\cdot\ln\left(\frac{V}{C}\right)\right]. \tag{15}$$

Expression (14) allows relating the reduction of the gas multiplication factor to the number of neutron interactions in the burst. This can be used for both versions of LUPIN to compensate for the *H*(10)* underestimation even in presence of an extremely intense PNF. This technique could be implemented only if all the variables shown in expression (14) are known, i.e. the applied voltage V, the number of neutron interactions in the burst $N_i$ and the functions B, C and D. Whereas V and $N_i$ can be easily derived, the calculation of B, C and D is trickier. D depends from the energy released to the reaction products and from physical properties of the detector, and can therefore be calculated with little effort. In the case of LUPIN-BF: $\Theta$ = 2.31 MeV, W = 33.7 eV, b = 12.5 mm, as derived from the detector specifications, and v = $7.36\cdot10^{5}$ $m^3$. D is then equal to $2.09\cdot10^{-4}$ V. B and C depend not only

from physical properties of the detector, but also from ΔV and K. The calculations of these two variables require performing complicated experiments that are beyond the aims of this study. However the value of B and C can be derived via an alternative method.

By profiting from the properties of LUPIN, one can acquire a spectrum in charge similar to the ones shown in Fig. 5 and Fig. 6, from which one can derive the value of charge deposited by the reaction products in the gas Q. By knowing the W-value of the gas and the energy Θ imparted to the reaction products by the neutron-induced reactions, one can use expressions (3) and (4) to derive the value of the multiplication factor M. This multiplication factor can be derived for several values of applied voltage V. This has been done by exposing LUPIN-BF at the *Politecnico di Milano* to an AmBe neutron source. The voltage applied to the detector was increased from 360 V to 1300 V in several steps and the peak value of the deposited charge Q was derived from the spectrum in charge. This allowed deriving the value of M for all the values of applied voltage V, as shown in Table VIII.

Table VIII. Multiplication factor calculated for LUPIN-BF for several values of applied voltage.

| Applied voltage [V] | Peak deposited charge Q [C] | Multiplication factor |
|---|---|---|
| 360 | $3.50 \cdot 10^{-15}$ | 1.00 |
| 400 | $6.70 \cdot 10^{-15}$ | 1.09 |
| 600 | $1.74 \cdot 10^{-14}$ | 3.32 |
| 800 | $6.34 \cdot 10^{-14}$ | 9.84 |
| 1,000 | $2.80 \cdot 10^{-13}$ | 79.1 |
| 1,120 | $4.19 \cdot 10^{-13}$ | 82.2 |
| 1,200 | $6.29 \cdot 10^{-13}$ | 100 |
| 1,300 | $1.52 \cdot 10^{-13}$ | 144 |

One can now solve expression (15) iteratively by using the values given in Table VIII. The values for B and C for LUPIN-BF have been found to be 297.2 V and 349.7 V, respectively.

The number of neutron interactions in the burst $N_i$ can be easily derived from the LUPIN-BF readings for each value of applied voltage V. This allows calculating the value of the reduced multiplication factor M' from expression (14). One then knows the correction factor M/M', which is by definition bigger than 1, and can compensate the LUPIN-BF readings to take into account the space

charge effect and further extend the linearity of the detector response to higher intensities. A test has been performed by calculating the correction factor M/M' for the measurements performed at HZB, described in Section 2.2.3., in order to apply a proper correction factor to the LUPIN-BF readings and verify the linearity of the corrected data. This test was performed only with the data obtained in this measurement campaign due to the fact that the neutron burst was impinging on the detector in an extremely short time, from 1 μs to a maximum of 10 μs, i.e. lower than the charge collection time, whereas in all other campaigns the burst was composed by a prompt fraction and a delayed part, thus making incorrect the computation of all neutron interactions in the value $N_i$.

The number of neutron interactions in the burst $N_i$ was derived for each measurement directly from the LUPIN-BF readings. This can be related to the value expressed in Table IV by dividing the *H*(10)* by the detector conversion coefficient from neutron interactions to *H*(10)*, calculated as described in Section 2.2.1. The multiplication factor M, the reduced multiplication factor M' and the correction factor M/M' have been calculated for machine settings 5-13. All the values are shown in Table IX.

Table IX. Correction factor M/M' calculated for all machine settings of the measurement campaign performed at HZB.

| Machine setting | Number of neutron interactions $N_i$ | Reduced multiplication factor M' | Multiplication factor M | Correction factor M/M' |
|---|---|---|---|---|
| 5 | 3.38 | 125.1 | 125.2 | 1.001 |
| 6 | 8.60 | 124.9 | 125.2 | 1.002 |
| 7 | 17.4 | 124.6 | 125.2 | 1.005 |
| 8 | 26.0 | 124.3 | 125.2 | 1.007 |
| 9 | 36.0 | 124.0 | 125.2 | 1.010 |
| 10 | 90.0 | 122.1 | 125.2 | 1.026 |
| 11 | 165 | 119.6 | 125.2 | 1.047 |
| 12 | 300 | 115.4 | 125.2 | 1.085 |
| 13 | 838 | 101.2 | 125.2 | 1.238 |

The values have not been calculated for machine settings 1-4 because the number of neutron interactions in the burst was too low and the correction factor M/M' would have been equal to 1. The correction

factor has been applied to the *H*(10)* value measured by LUPIN-BF for each machine setting in order to compensate for the observed underestimations. The plot of the measured and corrected *H*(10)*, expressed as a function of the reference *H*(10)* per burst, is shown in Fig. 29.

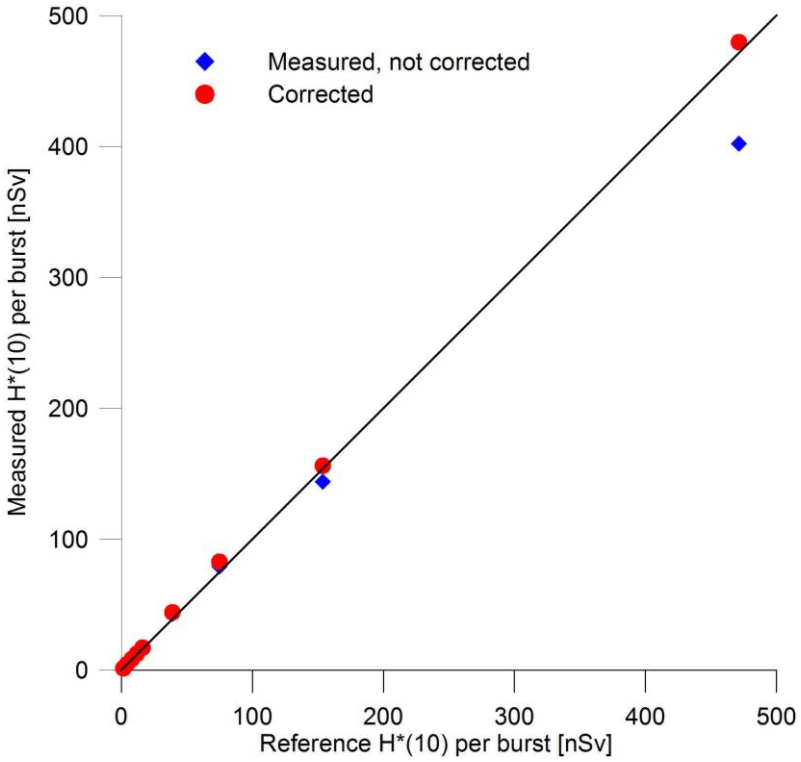


FIG. 29. Results obtained at HZB with LUPIN-BF expressed in measured and corrected *H*(10)* as a function of the reference value per burst. The linear response is represented by the black line.

The compensation introduced by the correction factor allows the LUPIN-BF response to stay linear in a range which is about one order of magnitude higher than what was observed in the non-corrected readings. Its linearity is in fact extended from about 80 nSv per burst to about 500 nSv per burst. The correction does not significantly modify the values measured for machine settings 5-10, since the number of neutron interactions was limited. In some cases the corrected *H*(10)* value slightly overestimates the linear response, but the difference is included in the range of the measurement uncertainties.

The analysis on the presence of a net space positive charge in the proportional counter caused by a huge number of neutron interactions in the same burst allowed deriving a correction factor that can be employed to correct the LUPIN readings. The correction factor derives from the estimation of the reduction of the gas multiplication factor and it is proportional to the number of neutron interactions in the burst. This can be used to compensate the *H*(10)* underestimation when the detector is exposed to

extremely intense PNF. The reliability of this technique has been demonstrated by applying the correction factor to the data acquired with LUPIN-BF in the measurement performed at HZB, where the detector was exposed to extremely short neutron bursts, whose length varied between 1 μs and 10 μs. This correction allowed the detector response to extend its linearity by about one order of magnitude, up to 500 nSv per burst, i.e. up to the maximum reference *H*(10)* per burst that could be obtained during the campaign. It is probable that this technique could extend the response linearity up to higher values, even if this needs to be proved in specific reference conditions that are difficult to be reproduced in practice.

The compensation technique can be easily implemented in the acquisition software, since the only parameter that must be known in order to apply the proper correction is the total number of neutron interactions in the burst. This value can be easily derived by dividing the total integrated charge by the MCC. However, since the usefulness of this compensation technique is limited to situations where the intensity of the neutron field reaches extremely high values, a proper threshold must be implemented in the software in order to activate the compensation algorithm only when the interaction rate overcomes a certain level, in the order of $10^5$ $s^{-1}$.

### 2.4. Neutron die-away time in the moderating assembly

As mentioned in the previous sections, the trend in time of the signals acquired with both versions of LUPIN cannot be explained if one does not introduce the concept of thermalisation and diffusion of the thermal neutrons in the detector moderating assembly. These processes are governed by a constant characteristic of each moderator, called neutron die-away time. This section will treat this topic by starting from a historical introduction about past studies and then by analysing the data obtained with LUPIN in the measurement campaigns described in the previous sections. An example on how this constant could be used to develop a new acquisition technique and to improve the performance of any thermal neutron detector working in pulse mode will also be given, by starting from a direct evidence which has been observed in the measurements performed at HZB, comprehensively described in Section 2.2.3.

A strong effort was put in the past in the research of techniques that would allow efficient operation of neutron detectors in PNF without being affected by dead time losses. A theoretical study performed by Leake et al. [Leake et al. 2010] proposed the adoption of a technique to compensate for

the underestimations shown by *H*(10)* neutron detectors in PNF. This technique is based on the hypothesis of the existence of a neutron die-away time, τ, that would govern the slowing down and the subsequent exponential decay of the thermal neutrons produced in the moderating assembly of a thermal neutron detector. There is a long history of studies speculating the existence of τ: Von Dardel and Sjostrand were the first who postulated in 1954 the presence of a neutron diffusion parameter in water moderators [Von Dardel and Sjostrand 1954]. A similar hypothesis was made by Leake in 1966 and by Dinter in 1976 in their analysis of the results of measurements performed with spherical neutron detectors [Leake 1966, Dinter and Tesch 1976]. Thomas et al. in the 80s suggested that the variation in time of the population of thermal neutrons entering a detector surrounded by a moderator could be governed by an exponential decay [Thomas et al. 1984]. More recently Woznicka et al. calculated the value of τ for spherical moderating materials with varying diameters [Woznicka et al. 2000]. In the last years Monte Carlo codes were used to determine the value of τ for polyethylene moderators of various shapes and dimensions [Justus 2011]. In spite of the number of theoretical studies on this topic, there is a lack of experimental results supporting the evidence of the presence of τ and about the application of a τ-based detection technique.

The importance of the knowledge and of the experimental verification of the value of τ lies in the fact that it can be used to reconstruct the total number of neutron interactions generated in a detector by a neutron burst of duration t, where $t << \tau$, a condition that is always fulfilled in PNF. The population of thermal neutrons n(t) entering at a time t the detector, which is hosted in a moderating assembly, varies as follows:

$$n(t) = n(0) \cdot e^{-t/\tau}, \tag{16}$$

where t = 0 corresponds to the time when the first thermal neutron interaction is detected. This implies that the thermal neutron populations has its maximum value at t = 0, which is of course not true, but this assumption is acceptable since it introduces negligible approximations. By assuming that the acquisition is triggered at t = 0 and by knowing the value of τ, if n(t) can be correctly measured at any time t, the value of n(0) can be extrapolated and the total number of thermal neutron interactions N generated by the burst in the detector can be calculated as follows:

$$N = \int_0^{\infty} n(t) = \int_0^{\infty} n(0) \cdot e^{-t/\tau} = n(0) \cdot \tau \quad . \tag{17}$$

In practice $t = \infty$ means $t \approx 5\tau$. This technique is valid under the assumption that the detector has a significant interaction cross section only for thermal neutrons and can be applied with any detector, regardless from its geometry and its dead time. In fact, after a certain time t = t' the detected neutron interaction rate m will become low enough to reduce at minimum the underestimation induced by dead time losses and this will allow the calculation of n(0) and consequently of N. If we assume that the non-paralysable dead time model can be used [Knoll 2010b] and if we tolerate a difference between the detected and the true interaction rate of x (in percentage), then the value of t' can be determined as the time at which the measured interaction rate falls below the value m', calculated as follows:

$$m' = \frac{1-x}{D} \quad , \tag{18}$$

where D is the detector dead time. x should be fixed in the same order of magnitude of the measurement uncertainty. As an example, if $D = 10^{-6}$ $s^{-1}$ and x = 0.1, then $m' = 10^{-5}$ $s^{-1}$.

In order to verify the reliability of this technique, its main principle has been applied off-line to some of the data acquired during the measurement campaign performed at HZB. The value of τ has been derived from a recent study, see ref. [Justus 2012], where Monte Carlo simulations have been performed to derive its value for typical moderating assembly. τ was found to be equal to 70 μs for Wendi-2 and 140 μs for a 10-inch diameter spherical polyethylene moderator when the detector is exposed to a narrow high-energy pulsed beam. This value depends from the neutron spectrum which impinges on the detector and can substantially vary if the detector is exposed to different radiation environments. The 70 μs value has been assumed to be valid also for BIOREM, which has a moderating assembly very similar to Wendi-2, except for the absence of the tungsten layer. The assumption is acceptable since the layer of high-Z material is needed to improve the detector sensitivity to high-energy neutrons, but it does not substantially influence the variation of the thermal population in the entire assembly. Therefore, its absence does not introduce significant modifications in the τ value. On other hand the 140 μs value has been considered to be applicable to LINUS, whose moderator has a diameter of 25 cm, i.e. about 10 inches. For the analysis the dead time D of Wendi-2 has been assumed to be

equal to 1.7 μs for Wendi-2 and 1.0 μs for BIOREM, as calculated in Section 2.2.4., and 15 μs for LINUS.

For the purpose of the analysis the neutron burst has been considered to be concentrated in an infinitely short time in order to consider the maximum interaction rate at t = 0 and to simplify the calculations. This is however a reasonable assumption, since the burst length of the primary beam was included in the range 1-10 μs for machine settings 1-12 and was equal to 40 μs for machine setting 13 (employed only for LUPIN-BF), i.e. much lower than the total length of the detector signal, which can be approximated to be equal to $5 \cdot \tau$, i.e. 350 μs for cylindrical detectors and 700 μs for spherical detectors. Under this assumption the trend of the neutron interaction rate in the proportional counter is characterised by an exponential decay with a maximum at t = 0. In order to obtain the expression of the variation in time of the neutron interaction rate in the proportional counter one needs to know the value of n(0), as can be derived from expression (16). This was derived by first calculating the total number of neutron interactions generated in the proportional counter by the burst, which has been obtained by dividing the value of the reference $H^*(10)$ per burst for each machine setting by the calibration factor of each detector. Then n(0) has been obtained via expression (17). The interaction rate has been evaluated for discrete time values, at $t = t' + k \cdot \Delta t$, where t' = 2.5 μs, $\Delta t$ = 5 μs and k = 1,2,… 200, i.e. from t = 2.5 μs to t = 1.025 ms. This interaction rate will be from now on defined as the "true" interaction rate n to be distinguished from the measured interaction rate m. m is lower than n because of the dead time losses and it has been calculated via expression (1) for each time value. An example of the different trend in time of the true and the measured interaction rate is shown in Fig. 30 for Wendi-2 for machine setting 9.

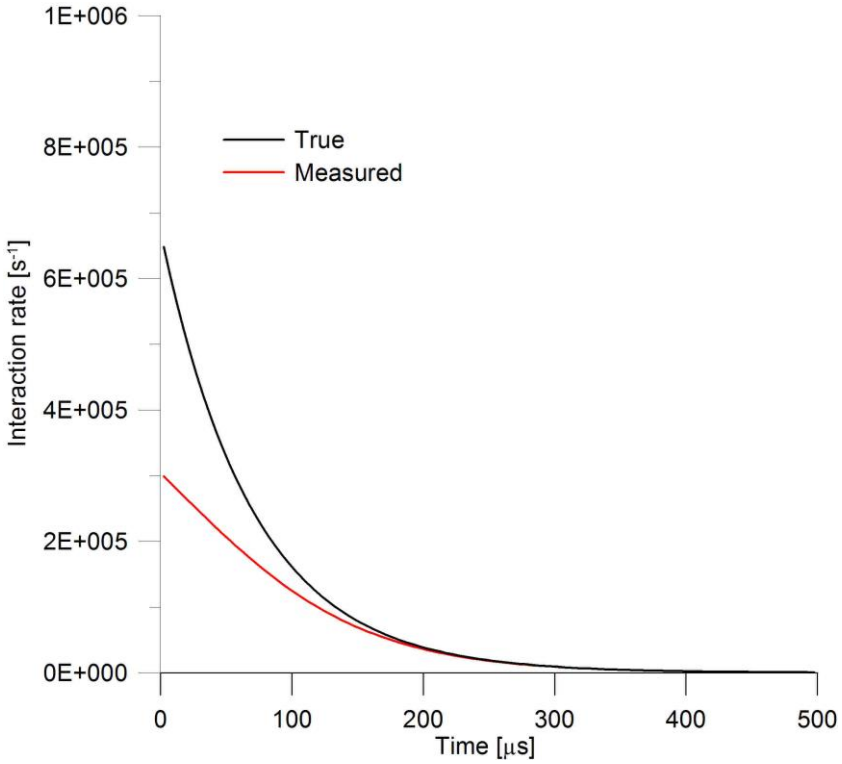


FIG. 30. True and measured interaction rate as calculated for Wendi-2 for the measurements carried out at HZB with machine setting 9.

It is clear that the true interaction rate is characterised by an exponential decay, while the measured interaction rate is decreasing with a different trend. This is due to the fact that the highest difference between measured and true interaction rate is found when the true interaction rate is higher, i.e. in the first part of the signal. If one takes the measured interaction rate m and multiplies it by the time width $\Delta t$ of each bin, i.e. 5 μs, the number of measured counts can be derived. If this number is integrated from $t = 0$ up to $t = 5 \cdot \tau$ one can obtain the total number of measured counts for each beam setting and, by multiplying this value by the detector calibration factor, the integrated *H*(10)*. This has been done for all the machine settings employed in the measurement campaign and compared with the data actually measured with Wendi-2 and BIOREM. The comparison is shown for both detectors in Fig. 31.

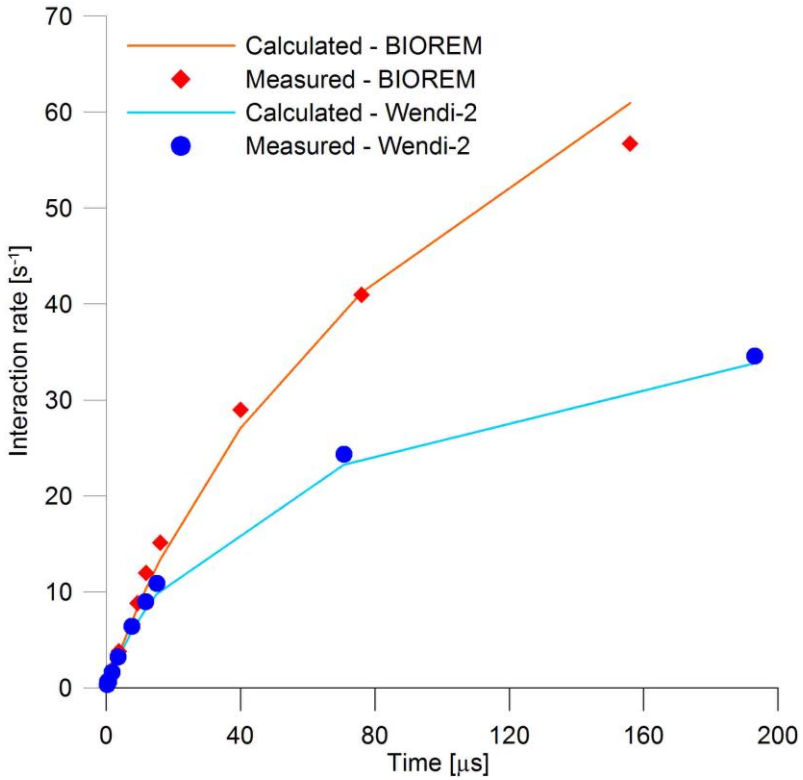


FIG. 31. Comparison between the *H*(10)* measured by Wendi-2 and BIOREM at HZB for machine settings 1-12 and the *H*(10)* calculated via the analysis based on the neutron die-away time in the detector moderator.

The measured data have been represented via blue or red marks, while the calculated values have been linked by a coloured line. The agreement between measured and calculated data is excellent over the entire *H*(10)* range, apart for the last point for the BIOREM data, where the calculated value slightly overestimates the measured one. This means that the assumptions made above on the value of the dead time and of the value of τ are acceptable and that the simplified model of the variation of the thermal population in the moderating assembly is reliable.

The calculations cannot be carried out for LINUS since it is an instrument working via a paralysable electronics, for which the true interaction rate n is linked to the measured interaction m via the following expression:

$$m = n \cdot e^{-n\tau} \quad . \tag{19}$$

The value of n can be derived for each machine setting only in an iterative way, which makes things more complicated. Moreover, the neutron interaction rate for machine settings 10-12 was high enough that, due to the high dead time characteristic of LINUS, the curve shown in Fig. 31 for BIOREM and

Wendi-2 would reach a maximum for machine setting 10 and would then start to decrease. These two combined specificities introduce complications that do not allow a reliable model based on the neutron die-away time to be derived.

For both versions of LUPIN the calculation of the total number of counts measured for each machine setting cannot be performed since the instrument is not characterised by a dead time. Moreover, it has been shown in Section 2.3. that the only effect which is limiting the operation of LUPIN for very high interaction rate is related to the space charge effect. Nevertheless, the trend in time of the thermal neutron population in the LUPIN-BF moderating assembly can be extrapolated from Fig. 14, where it is clear that the output signal lasts for about 500 μs. If one considers that the exponential decay reaches extremely low values after 5 time constants, then the τ value of LUPIN-BF can be approximated to be equal to about 100 μs, a value slightly higher than the one found for Wendi-2, i.e. 70 μs. The LUPIN-BF moderator is similar to the Wendi-2 one, except for the fact that the tungsten layer is replaced by a lead one and that the diameter is 25 cm instead of 23 cm. This higher diameter reflects in a longer diffusion time of the neutrons in the moderator before they reach the proportional counter and can explain the slightly higher value for τ. The same conclusions can be obtained by observing Fig. 25 and Fig. 27. The first signal has been obtained in a critical loss point of the CERN PS, where the losses were characterised by an extremely short time structure, and has a total length of about 500 μs. The second signal has been obtained with LUPIN-He at the *San Raffaele* hospital in Milan. Its length is approximately 500 μs, which means a τ value equal to about the same value as for LUPIN-BF, in contrast to what has been derived from ref. [Justus 2012] for a 10 inch spherical moderator, i.e. 140 μs, very similar to the moderating assembly of LUPIN-He. This difference can be explained with the fact that τ was calculated for a detector exposed in a high-energy neutron field, whereas the measurements carried out at the *San Raffaele* hospital were characterised by a low-energy field. The energy of the primary beam was in fact slightly above the threshold needed to generate photoneutrons in the structures surrounding the accelerator. A lower average energy of the neutron field clearly reflects in a lower time needed for the neutron thermalisation and, therefore, in a lower value of τ.

This analysis based on the neutron die-away time could result in an implementation of an acquisition software for a generic active neutron detector working in pulse mode for which the τ value could be calculated under controlled irradiation conditions, given that its main variations could be due to a different average energy of the impinging neutron field. The critical parameter from which this

technique depends is the critical interaction rate m', as defined in expression (18). The software should work in such a way that when the detector is not exposed to PNF the standard acquisition chain is used and the counting is performed in pulse mode. When the acquisition is carried out in PNF, the acquisition should switch in an alternative mode, which reconstructs the number of counts integrated in the neutron burst from the tail of the signal. In order to determine which part of the signal should be considered for this reconstruction, the software should analyse the average delay present between one interaction and the following for at least 50 samples. If this average delay is below 1/m', then a count integrator should be activated, in such a way that at the end of the neutron burst the software can apply expression (17) for the signal profile reconstruction.

The presence of a neutron die-away time in thermal neutron detectors have been hypothesised by many authors in the past in order to develop new acquisition techniques when they are exposed in PNF, but no papers are present in the literature about experimental evidence of the presence of this constant $\tau$. Through results obtained during the measurements performed at HZB, an analysis has been performed which proves the existence of the neutron die-away time for Wendi-2 and BIOREM when they are exposed to extremely short neutron bursts. This neutron die-away time strongly governs the production of the signal in the proportional counter, especially for neutron bursts characterised by a very short duration. In relation to this, the application of a promising technique which can reconstruct the signal profile by calculating the total number of neutron interactions from the tail of the signal has been proposed. Its validity is demonstrated by the calculations performed for the HZB measurements but its implementation requires further investigations in order to characterise the variation of $\tau$ as a function of the energy of the impinging neutron field.

**Chapter summary**

In this chapter the LUPIN detector has been presented by describing its working principle and its physical characteristics and by underlying the difference existing with a conventional rem counter. Its performance has been tested in several measurement campaigns, which have been presented by describing the facility in which the measurements have been performed, the experimental set-up and the most significant results. The main outcome of each of these campaigns has been defined, by giving an explanation of the characteristics of the observed response and by presenting an overview of the possible the solutions to be implemented in order to improve the detector performance. The explanation of the physical effects at the basis of the partial saturation of the response observed in extreme stray

field conditions has also been given, by focusing the attention on the possible corrections to be implemented in the acquisition algorithm in order to compensate for the space charge effect. A discussion has also been devoted to the description of the neutron die-away model that governs the variation of the thermal neutron population in a detector moderator and that can be used to compensate the dead time losses in a generic neutron rem counter.

# 3. A versatile beam loss monitor

The electronics employed in LUPIN showed to be an excellent solution for solving the typical issues encountered by a rem counter when it is working in PNF. LUPIN shows a linearity of the response up to several hundred nSv per burst and this working range covers all the applications where the detector can be employed for radiation protection purposes. Nevertheless the results obtained in the different measurement campaigns, comprehensively described in Chapter 2, show that the same electronics could be employed not only for a rem counter, but also for a Beam Loss Monitor (BLM) or, more generally, of a detector to be used for machine protection in an accelerator complex. A BLM is in fact exposed to stray fields whose intensity is much higher than the typical radiation environments where radiation protection instrumentation is employed. This is due to the fact that BLMs are installed in areas where the access to the workers is forbidden during the accelerator operation. This chapter describes the potential advantages of LUPIN in its application as a BLM and as a complementary instrument for supporting least intrusive beam monitoring techniques around particle accelerators. Section 3.1. introduces the characteristics that an ideal BLM should have in order to be employed around an accelerator complex. Section 3.2. shows the results obtained in measurement campaigns performed in two facilities where LUPIN has been tested in selected positions in order to test its performance as a BLM. Section 3.3. speculates the potential application of LUPIN as a detector supporting least intrusive beam monitoring techniques. It must be underlined that the tests described in this chapter have been performed with the same prototype employed for the measurements described in Chapter 2, but in principle the future development of the detector could follow two separate paths. The first is to employ the LUPIN electronics to realise a detector with a simpler moderating assembly, composed by polyethylene only, due to the fact that the inserts of boron, cadmium and lead have been designed to model the detector response on the shape of the ICRP conversion coefficients curve, and that requirement is not needed for this application. The second solution is to employ LUPIN in its present configuration in order to profit from the different information that can be derived at the same time from the detector, both for radiation protection purposes and for machine protection. The assessments and the description of the measurements are given below for LUPIN-BF only, since the choice fell on the version of the detector that showed the best performance in terms of response linearity. This is in fact the main requirement needed for the application as a BLM whereas the typical advantage

of LUPIN-He, i.e. the isotropic response, is not interesting since it does not introduce any significant feature.

### 3.1. Introduction

The aim of a BLM is to detect an unintentional interaction of beam particles accelerated in the storage ring with the surrounding structures, thus causing the emission of radiation. A great variety of BLMs exist: ionisation chambers (ICs) [Stockner et al. 2007], scintillators [Payne and Whitehead 2006], PIN diodes [Shiltsev 1998], secondary emission monitors [Kramer et al. 2007], Cherenkov light detectors [Mallows et al. 2012]. The ideal solution for a BLM to be adopted in an accelerator complex is usually a mix of different detectors and in most cases the characteristics of the instruments must be customised on the basis on the accelerator design and the needs of the facility [Wittenburg 2008]. The potential use of an instrument based on the electronics used for LUPIN has been considered by evaluating its performance on the basis of the features required by Zhukov [Zhukov 2010] for an ideal BLM to be employed in a generic accelerator and by comparing them with the typical features of an IC.

An ideal BLM is a radiation detector that:

- can efficiently measure over a wide dynamic range of the incoming radiation burst in order to be employed for the detection of the beam losses foreseen by the accelerator design, typically characterised by low intensity, and unforeseen losses, typically characterised by a high intensity and a short duration;
- is sensitive only to radiation caused by a beam loss and can discriminate it from background radiation and from radiation induced by other causes;
- allows the direct determination of the absolute amount of lost particles or the relative fraction of lost beam with reasonably low uncertainties;
- can resolve the time structure of the beam losses;
- can determine the spatial distribution of the beam losses in order to derive the section of the accelerator where the interaction between the particles and the surrounding structures occurred.

A detector working with the electronics of LUPIN easily satisfies the first requirement: it can in fact efficiently measure over a wide dynamic range of the impinging radiation burst, being able to

detect a neutron burst intensity varying over more than six orders of magnitude with an underestimation lower than 30%. As observed in the measurements described in Chapter 2, it can detect a neutron flux of few $cm^{-2} \cdot s^{-1}$ generated by the cosmic background, the radiation burst caused by the loss of a small fraction of the beam interacting with the accelerator structures, as well as a fast and intense radiation burst generated by an instantaneous and complete loss of the beam in a single impact. An IC can meet this requirement as well, even if problems arise and special solutions must be adopted when the current to be measured is too low, e.g. dedicated electronics and low-noise cables for transporting the signal. The second requirement refers to synchrotron radiation and cavity X-rays only, i.e. sources of radiation that do not involve a direct interaction of the primary particles with the materials employed in the accelerator components. These sources of radiation can be well discriminated by the stray field caused by a beam loss due to the excellent photon/neutron discrimination properties of LUPIN, described in detail in Section 2.2.6. for its use in steady-state fields and in Section 2.2.7. for mixed pulsed fields. For an IC the discrimination capability is strongly related to the type of gas used: for an air-filled IC the interaction of neutrons in the gas is essentially negligible, whereas for other gases, such as pressurised Argon or Hydrogen, the interaction probability is significant and the collected signal cannot be discriminated on the basis of the particle that ionised the gas. In this case an efficient discrimination between the two sources of radiation cannot be carried out efficiently. According to the third requirement, the order of magnitude of the intensity of the beam losses can be conveniently derived from the integrated amount of charge collected by LUPIN. This correlation cannot be achieved with high precision, but usually the attention is mainly focused on the distinction between small and severe losses rather than on the precision of the measurement. The time structure of the losses can be derived with LUPIN by analysing the signal and by taking into account that for neutron bursts of short duration its trend in time is essentially governed by the neutron die-away time in the moderating assembly, as comprehensively explained in Section 2.4. The spatial distribution of the losses cannot be obtained with LUPIN, because the detector is equally sensitive to radiation bursts generated by the interaction of lost particles in different parts of the accelerator, close or remote, being incapable of determining with a low uncertainty the point where the losses originated. However, one could compare the signals obtained by two LUPIN detectors placed at a given distance around the beam line in order to derive information on the originating point of the losses. The intensity of the signal is in fact much higher than what can be obtained with an IC. This is explained by the neutron ability to penetrate the structures surrounding the

beam line, the usual materials being iron, copper and steel, which effectively attenuate photons but not neutrons. This results in a much higher efficiency of LUPIN if compared to an IC. Other advantages offered by LUPIN as a BLM are:

- its high sensitivity in terms of nSv per count (see Section 2.2.1.), which is comparable with all commercial rem counters;
- its cost, comparable with a high precision IC;
- the determination of its calibration factors (see Section 2.2.1.), that depend solely on the detector geometry of voltage applied to the proportional counter, as supplied by the internal power generator.

It is also interesting to roughly estimate the sensitivity of LUPIN as a BLM in terms of collected charge per unit of absorbed dose generated by the impinging radiation field, expressed in C/Gy, and to compare it with the typical sensitivity of the other BLM technologies. This is a trivial calculation when the BLM is based on photon detection, but it requires slightly more attention in this case since LUPIN is based on neutron detection. The average collected charge per single neutron interaction can be easily derived from Table I, since it is equal to the MCC. This value can be rounded for simplicity to 250 fC for LUPIN-He and 600 fC for LUPIN-BF. The *H*(10)* calibration factor can also be derived from Section 2.2.1. It is equal to $3.64 \pm 0.26$ $nSv^{-1}$ for LUPIN-He and $2.13 \pm 0.17$ $nSv^{-1}$ for LUPIN-BF. This results in a sensitivity of $9.10 \cdot 10^{-4}$ C/Sv for LUPIN-He and $1.28 \cdot 10^{-3}$ C/Sv for LUPIN-BF. In order to get a value which is comparable with other techniques based on photon detection, these values must be converted in collected charge per absorbed dose. It would in fact be senseless to make the comparison in terms of collected charge per unit of dose equivalent, since this is a pure radiation protection quantity and the interest is here focused in the application of LUPIN as a BLM. Since this is a rough estimation, we can assume an average radiation weighting factor for neutron of 10 Sv/Gy, as taken from ICRP 103 [ICRP 2007], which results in a sensitivity that varies from $9.10 \cdot 10^{-3}$ C/Gy for LUPIN-He to $1.28 \cdot 10^{-2}$ C/Gy for LUPIN-BF. The average sensitivity of LUPIN is therefore equal to $10^{-3}$ C/Gy. Table X compares this sensitivity with the values typical of the most employed BLM technologies, as estimated in ref. [Fröhlich 2008] for typical detector dimensions and collection efficiency.

Table X. Estimated sensitivity of different BLMs, sorted from the most to the less sensitive one.

| Detector | Estimated sensitivity [C/Gy] |
|---|---|
| PMT with organic scintillator | $2 \cdot 10^{2}$ |
| Bare PMT (Cherenkov light) | $4 \cdot 10^{-3}$ |
| LUPIN | $10^{-3}$ |
| Ionisation chamber | $7 \cdot 10^{-5}$ |
| Long ionisation chamber | $2 \cdot 10^{-5}$ |
| PIN diode | $6 \cdot 10^{-6}$ |
| PMT with Cherenkov fibre | $2 \cdot 10^{-6}$ |
| Secondary emission monitor | $5 \cdot 10^{-10}$ |

It can be noted that the sensitivity of the different technologies varies by about 12 orders of magnitude, as it is extremely dependent on the energy deposited by the particle, the electronics gain, the active mass and the collection efficiency of each detector. As a general rule, one can assume that a higher sensitivity corresponds to a higher probability of detecting low intensity losses and in discriminating them from the background signal. At the same time a high sensitivity could constitute an issue in terms of dead time losses induced by the signal pile up and in poor radiation hardness, which is directly correlated with the radiation damage typical of each material. Both versions of LUPIN show a sensitivity which can be considered as moderately high if compared to the other BLM technologies and this can be considered a positive characteristic. Moreover, the drawbacks of the high sensitivity do not constitute an issue for LUPIN since the pile up of the signal does not cause dead time losses and the radiation hardness is not a limitation for proportional counters, since it has been proven that both $BF_3$ and $^{3}He$ can be employed for extremely high integrated neutron fluence without suffering from significant limitations [Tomoda and Fukasuka 1984].

### 3.2. Measurements

The measurements described in this section constitute preliminary tests performed in two facilities where there is a real need of a BLM system to be installed for machine protection and where the choice has not been made yet on the final solution to be adopted. LUPIN is a possible candidate for this application and it has therefore been tested in reference locations where typical conditions of beam losses in the accelerator have been reproduced. Section 3.2.1. and Section 3.2.2. will describe the main

characteristics of the facility where the measurements have been performed, show the signals obtained and sum up the advantages and the drawbacks of the potential use of LUPIN as BLM. As a general principle, LUPIN can become an interesting solution to be employed as BLM in an accelerator complex where the need of the facility is not only to have an efficient system for beam diagnostics but, more generally, a system capable of providing at the same time data on the beam losses and information that can be used for radiation protection purposes.

### 3.2.1. Measurements at a medical accelerator

LUPIN has been tested in order to verify its potential to become a BLM at the Italian National Centre for Oncological Hadrontherapy (CNAO) in Pavia, Italy. In this accelerator complex protons and carbon ions are first accelerated in a LINAC up to 7 MeV and are then injected into a synchrotron in order to reach a maximum energy of 250 MeV for protons and 250 MeV/u for carbon ions. The beam is then used to irradiate tumours in three treatment rooms. An additional beam line is also available for material testing and detector developments. A picture of the synchrotron vault, taken from ref. [Rossi 2011], is shown in Fig. 32.

FIG. 32. The CNAO synchrotron.

The performance of LUPIN has been tested here since its development was originally triggered by the need of an instrument to be employed for the CNAO synchrotron both as a rem counter for personnel protection, and as a BLM. From the point of view of the beam diagnostics, the typical scenarios that

can be encountered around the CNAO synchrotron, and more generally around a synchrotron, are the following:

- instantaneous and complete loss of the beam in a single impact;
- continuous loss of a fraction of the beam, typically in the order of 1% of the nominal intensity, along the entire accelerator, as usually foreseen in the machine design.

The first scenario results in the production of an intense neutron burst caused by the interaction of the beam with the structures surrounding the accelerator, mainly magnets and pipes, and the shielding. The neutron fluence has been estimated to be in this case about $10^5$ n/cm$^2$ at 1 m from the interaction point for the CNAO accelerator [Nakamura and Heilbronn 2006]. The second scenario causes the production of neutron bursts of lower intensity due to the reduced fraction of beam, which is lost in the interaction point. LUPIN is in principle able to correctly detect the intensity of the radiation bursts produced in both cases. In the event of a sudden and short beam loss, the time width of the signal in the detector is dominated by the neutron die-away time of the neutrons in the moderating assembly. This helps reducing the instantaneous interaction rate in the proportional counter and thus reducing the underestimation issues. On the other hand, once the die-away time of the moderating assembly is known, there are no major issues in deriving the original time structure of the impinging burst.

Since the measurements were performed in the commissioning phase of the facility, the tests could be carried out only with the LINAC fully operating. LUPIN-BF was therefore installed in a reference location at 1 m from a copper Faraday cup hit by a 7 MeV proton beam accelerated by the injector LINAC. This test was performed to check the behaviour of the detector in a situation that resembles the first scenario described above. An example of the signal acquired in this campaign is shown in Fig. 33.

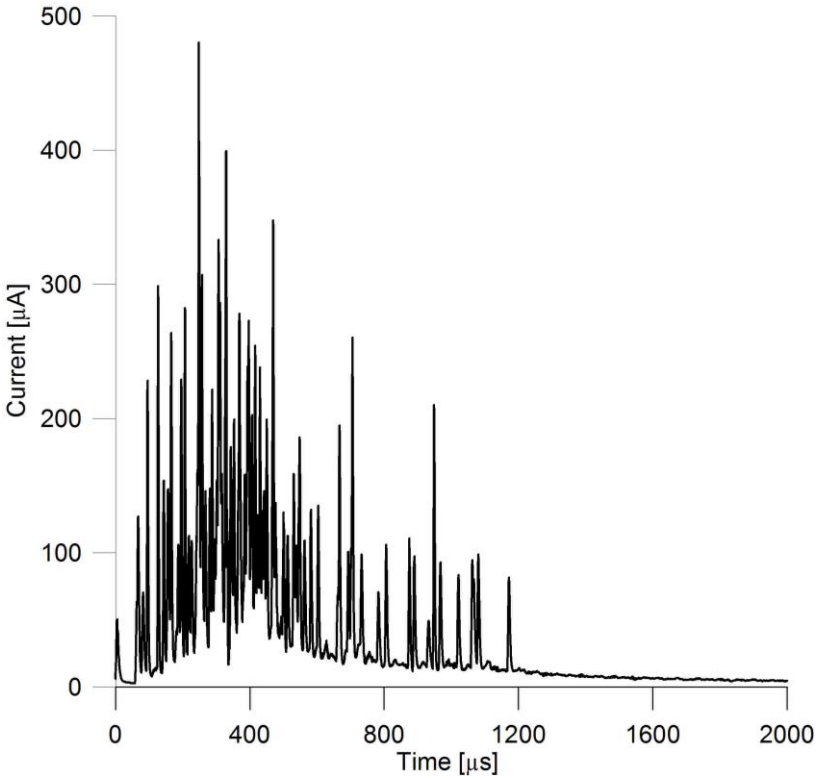


FIG. 33. Signal acquired with LUPIN-BF at CNAO.

The acquisition window was set to 2 ms. The signal is characterised by a first low intense prompt peak which reaches about 80 nA, generated by the pulsed photon field which is accompanying the neutron burst. The interaction rate then progressively increases. It must be noted that the photon field will always accompany the neutron burst in all interactions between the beam and the accelerator structures. However, since the discrimination properties of the detector have been comprehensively discussed in Section 2.2.6. and Section 2.2.7., for the following discussion it will be assumed that LUPIN is able to discriminate the neutron from the photon signal. The maximum interaction rate is reached after 300 μs when the current goes up to 480 nA, then the signal is slowly decreasing, following an exponential decay curve. This signal decrease is not governed by the neutron die-away time because the thermal neutron population in the moderator is too low and the diffusion effects are very limited. It is instead dominated by the typical behaviour of the logarithmic amplifier, which shows a fast response when the input current is high, whereas its characteristic time constant becomes extremely high when the input is of limited intensity, as it is the case for the last part of the signal of Fig. 33, and in general for the tail of all signals acquired by LUPIN when the intensity of the impinging burst is low. The peaks observed in the signal after 1 ms are due to scattered neutrons that interacted in the proportional counter after having encountered many scattering events in the moderator or on the surrounding structures. After

subtracting the current background and by neglecting the first 10 μs signal, dominated by the prompt photon peak, the total charge collected in the burst has been calculated to be equal to 231.0 pC. By dividing this value by the MCC, as indicated in Table I for LUPIN-BF when the acquisition window is set to 2 ms, one obtains the total number of neutron interactions, i.e. 378. By assuming that all the neutrons have been detected in the first ms after having triggered the acquisition, the average interaction rate is $3.78 \cdot 10^5$ $s^{-1}$. For comparison, a neutron meter with a dead time of 5 μs would detect this interaction rate by introducing an underestimation of about 65%, thus making impossible its use for this application if a high reliability of the derived data is required.

In view of the use of LUPIN as a versatile monitor for radiation protection purposes, it is important to derive a value expressed as an average *H*(10)* rate. Under the assumptions made above, the *H*(10)* integrated in the burst is 178 nSv, i.e. still in the range where the detector shows a good response linearity, whereas the mean *H*(10)* rate averaged over the first ms of the signal is equal to 640 mSv/h. This is of course a value which is not relevant for radiation protection purposes, since these radiation levels can be attained only during the beam operation, when the access to the synchrotron vault is forbidden to the operators, but the LUPIN characteristics make it suitable to measure up to these extremely high radiation levels without encountering saturation issues. It is therefore obvious that for a lower *H*(10)* rate the underestimation of the real interaction rate would be negligible.

LUPIN can be considered as a potential choice for the installation of a BLM system for the CNAO synchrotron. This has been confirmed by preliminary tests performed by installing the detector in a reference position close to a Faraday cup hit by the 7 MeV proton beam accelerated by the LINAC. A solution which is currently under study is to install 10 LUPIN detectors in a symmetrical configuration around the synchrotron, at 1 m far from the accelerator lattice, radially spaced by an angle of 36°. This would result in a linear distance of about 8.3 m from one detector to the closest one and in a maximum path that a neutron should travel in a linear direction from the interaction point to the BLM of 4.2 m. A sketch of the possible detector locations to be adopted around the synchrotron is shown in Fig. 34, where the drawing has been taken from ref. [Rossi 2011].

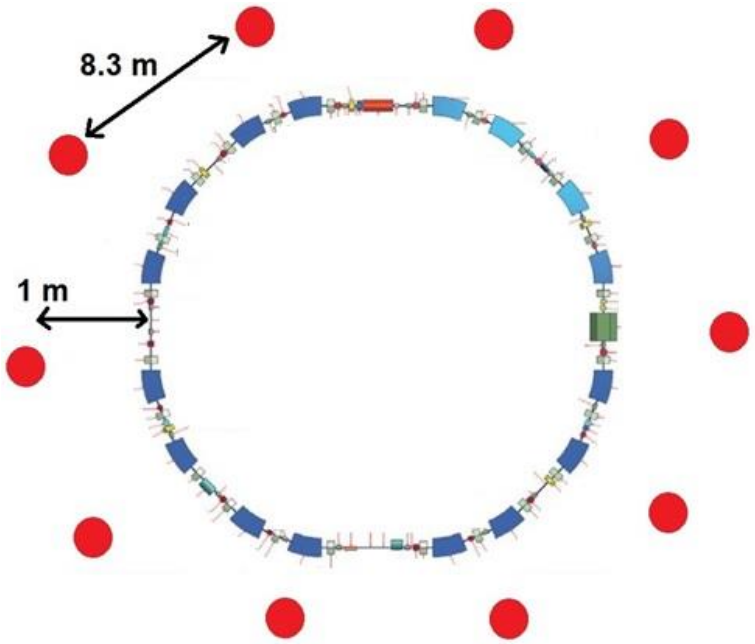


FIG. 34. The CNAO synchrotron lattice. The red marks show the 10 locations where LUPIN could be installed to operate as BLM.

A neutron burst generated by the interaction of the fraction of lost beam with the structures of the synchrotron will generate a signal in at least one of the detectors, and most likely in more than one. From the signals obtained from different detectors one can derive the exact loss point and can reconstruct its time profile. The distance between each detector has been chosen large enough so that a burst, which is interacting in a detector cannot generate a signal in the closest one, even taking into account the perturbing effects generated by the moderating assembly. Moreover the configuration has been chosen in order to reduce the contribution of moderating effect of the impinging neutron bursts caused by the building walls.

A measurement campaign has been performed as part of this project with LUPIN-BF in the commissioning phase of the CNAO synchrotron. The reproduced radiation environment resembles the typical exposure condition of the detector in case it would be employed in the future as a BLM. Indeed the possibility of successfully employing LUPIN as a monitor for personnel protection and as a BLM for beam diagnostics and machine protection in the synchrotron vault is real and should be carefully evaluated as an alternative to the conventional BLM that cannot provide any information on the *H*(10)* rate and must therefore be complemented by another set of detectors to be used for radiation protection only. This would allow providing information which are typically derived from different monitors via the use of a single detector technology. Further investigations are however needed in order to

understand how to derive from the signal of each detector installed along the accelerator the exact information on the position of the losses and on their temporal structure. Moreover, the detectors should be connected to a central monitoring system and a dedicated study should be performed in order to identify the problems related to the acquisition interface for such a complex system with a lot of information being collected by many channels in parallel.

### 3.2.2. Measurements at a FEL machine

A measurement campaign has been organised to test LUPIN at the injector test facility of the future SwissFEL at PSI in Villigen, Switzerland. The facility is constituted by a 230 MeV injector accelerator driven by an S-band radio frequency photo-injector. During the measurements the accelerator was operating at 230 MeV with a repetition rate of 10 Hz. The bunch length was a few ps, with a charge of 200 pC each, corresponding to about $10^9$ electrons per bunch. The beam was stopped on a dump constituted by a steel block shielded by concrete. The facility has been built, amongst other reasons, to allow a detailed verification and optimisation of the SwissFEL injector with the related instrumentation, and will be reused as injector for the future accelerator complex. LUPIN could be employed as a BLM in the future SwissFEL and, more generally, in one of the many FEL accelerators currently under construction worldwide, because of the typical short duration and high intensity of the accelerated particle bunches, which generate intense and pulsed radiation bursts when interacting with the surrounding structures in case of beam losses.

LUPIN could be employed in order to provide information useful both for radiation protection and for beam diagnostics. It could be installed in the critical points of the machine, where the probability of losing a fraction of the beam is highest, in order to be employed as a versatile device, acting as the same time as a BLM and as a rem counter. One of the priorities of the facility is in fact to have a BLM system capable of providing accurate information not only on the location, the intensity and the temporal structure of the beam losses, but also on the *H*(10)* rate detected close to the critical points of the beam line. This is due to the fact that the research centre must guarantee to the Swiss authorities that the neutron *H*(10)* rate on the non-classified areas located on top of the future accelerator will be lower than the legal limits. This is usually done by installing monitoring stations in the concerned areas. However, this is not possible for the SwissFEL accelerator since the entire construction has been built in the context of maximising the integration into the natural environment surrounding the research centre. Therefore radiation monitors cannot be installed in the non-classified area on top of the

accelerator, which are currently owned by the Aargau canton and used as public garden, but only in the locations which directly belong to the institute. The only solution is then to derive the radiation protection information from monitors located in the accelerator bunker. The *H*(10)* rate outside the shielding will be derived from the data acquired by these detectors, opportunely corrected by the attenuation factor introduced by the shielding thickness. The calculations will be complemented by dedicated Monte Carlo simulations where the entire accelerator geometry has been carefully reproduced. These strict requirements limit the choice of the instrument to be adopted for the BLM system to *H*(10)* meters, and therefore to neutron rem counters, for two main reasons: the instrumentation usually employed for machine protection cannot provide information on any radiation protection quantity, including the *H*(10)* rate; the radiation which will reach the surface will be mainly constituted by neutrons due to the much higher attenuation factor introduced for photons by the several tens of meters of ground thickness.

The measurements were performed in 12 reference locations with LUPIN-BF and four other rem counters in order to intercompare their readings: BIOREM, LB6411, Wendi-2 (see Appendix for a description of their main characteristics) and a prototype under development by Berthold specifically conceived to work in PNF, based on the activation of $^{12}C$ [Klett et al. 2010]. Since the performance of LUPIN-BF has been compared many times in the measurement campaigns described in Section 2 with the detectors used for these measurements, and the analysis on the different readings would not add supplementary useful information, only the results related to LUPIN-BF will be given here. It is enough to report that the response of LUPIN-BF, as expected, showed to be linear in a range of the impinging radiation bursts much wider than all the other detectors under test.

The locations were selected in the accelerator bunker on a parallel line running laterally at 1 m distance from the beam line: one position close to the electron gun, four positions close to the accelerating structures, three next to the bunch compressor, one near the diagnostic section and three around the beam dump. A sketch of the facility, together with the measuring locations and the abbreviations used to identify them, is shown in Fig. 35.

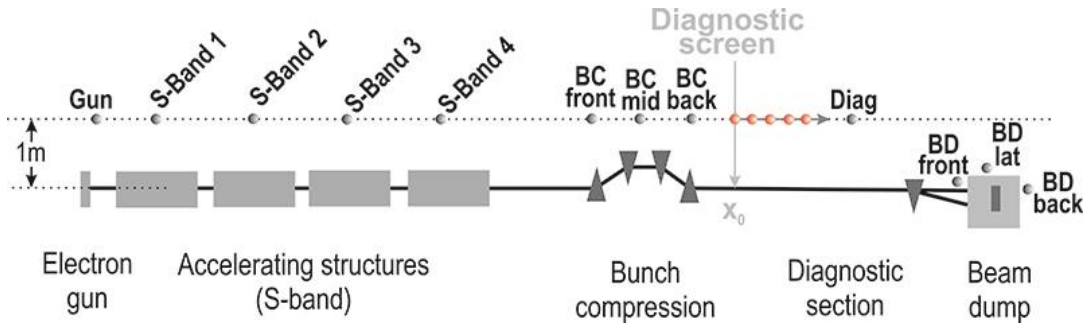


FIG. 35. Sketch of the SwissFEL injector test facility, with the 12 measuring locations shown on top (BC = Bunch Compressor, BD = Beam Dump).

The tests have been carried out by running the accelerator at the maximum intensity foreseen in its design in order to reproduce the most severe conditions of stray field in the bunker. For each position two sets of measurements were performed: the first by operating the machine in standard conditions; the second by switching off the laser and the gun, in order to assess the intensity of the stray field generated by dark current, which is one of the limiting factors in the operation of radio frequency gun-based linear accelerators, due to the possible activation and damage of accelerator components and the possibility of inducing quenches in superconducting cavities [Monaco et al. 2006]. An example of the signal acquired with LUPIN-BF in position BC-back with both laser and gun switched off is shown in Fig. 36.

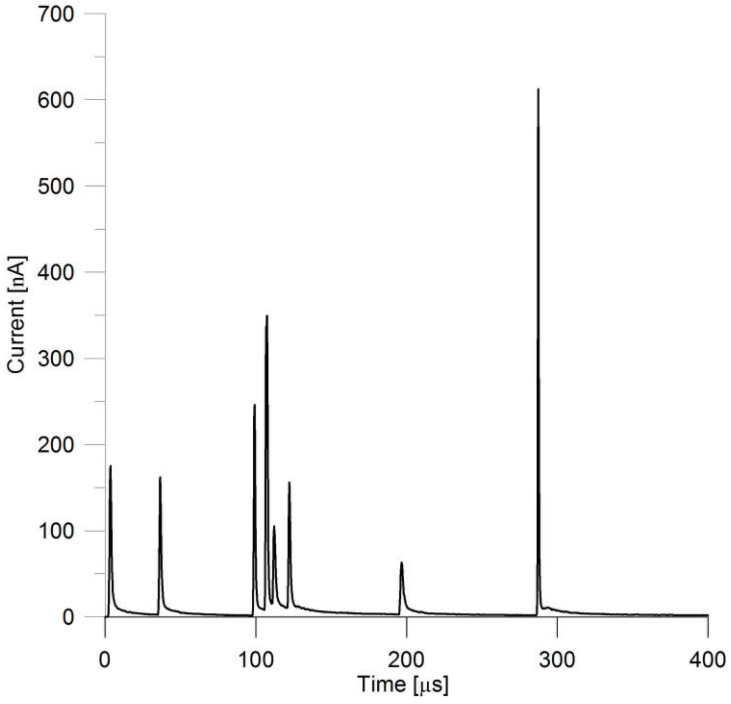


FIG. 36. Signal obtained with LUPIN-BF at PSI in reference position BC-back, dark current.

The acquisition window was set to 400 µs. As expected, the intensity of the stray field generated by the dark current is limited, with a maximum peak of the current signal equal to 620 nA. The total integrated charge is 4.7 pC and it can all be attributed to neutron-induced events, since at such low intensity the photon component of the stray field is widely attenuated by the structures surrounding the bunch compressor. The number of neutron interactions, which is equal to 8, can be here derived in two ways: by dividing the integrated charge by the MCC or by counting the current spikes, since the interaction rate is very limited and the photon contribution is negligible. Fig. 37 shows the signal acquired in the same location but with normal machine operating conditions. The acquisition has been performed by setting a trigger level.

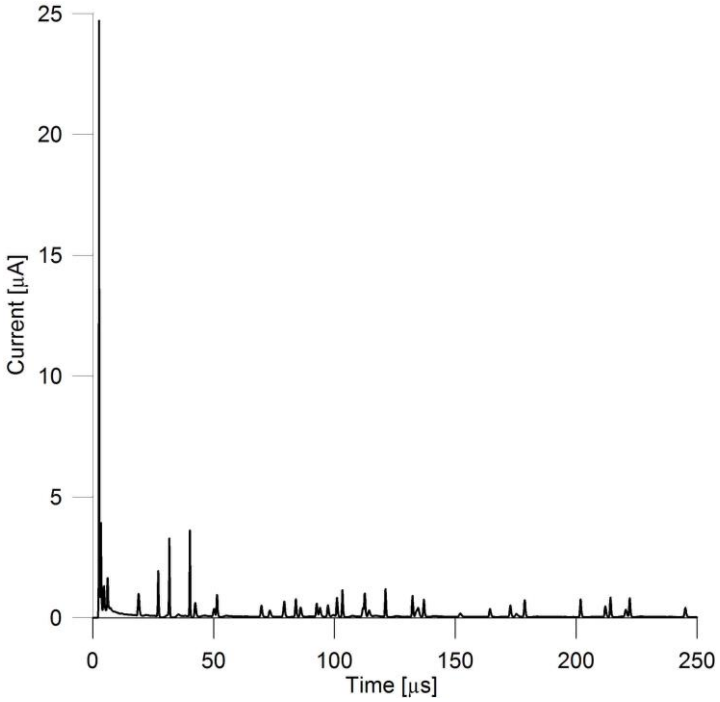


FIG. 37. Signal obtained with LUPIN-BF at PSI in reference position BC-back, normal operating conditions.

The acquisition window was set to 250 µs, as the expected interaction rate was much higher than in the previous case. The signal shows a very intense prompt photon peak which reaches a maximum of 25 µA and which lasts for a few µs after the acquisition start. This intense spike is present only in machine operating conditions as it cannot be generated by the low intensity losses generated by dark current. The following low intensity peaks are due to neutrons interactions, which are detected in LUPIN with a certain delay since the photons do not need to diffuse and to be thermalised in the moderating assembly before interacting in the gas whereas the neutrons do. The interaction rate progressively decreases after

50 μs and no major pile up effects can be observed. As a general rule, in these irradiation conditions each peak observed in the signal corresponds to a single neutron interaction. The rare peaks observed in the last part of the signal are due to neutrons that encountered many scattering events on the facility structures or on the detector moderator before being thermalised and subsequently detected in the gas.

As in the case of the CNAO synchrotron, the radiation bursts can be originated by low intensity losses foreseen by the accelerator design or by instantaneous and unforeseen losses of the accelerated bunch of particles. In addition, the losses can be generated here also by the so-called dark current typical of FEL accelerators. The first scenario losses originate from particles lost during the imperfect beam compression process in the bunch compressor. These particles interact with the accelerator structures thus producing a pulsed neutron burst accompanied by a photon field. This will be one of the main causes of beam losses in the SwissFEL and therefore the importance of testing the detector performance in these conditions is crucial. The typical feature of all losses generated in the SwissFEL, and more generally in a FEL accelerator, is the pulsed structure of the losses, due to extreme compression of the beam bunches. As comprehensively explained in Section 2.2.7., the discrimination between the neutron and photon induced signal can be performed on the basis of the detection time of the particles in the proportional counter. The photon component can be subtracted by excluding the first 10 μs in the calculation of the total integrated charge. By applying this technique the neutron *H*(10)* averaged in the signal can be derived for obtaining information used for radiation protection for the personnel working in the facility and for the external non-classified areas. The integrated charge due to neutrons is 27.7 pC, corresponding to 45 neutron interactions and an *H*(10)* averaged over the 300 μs of about 259 mSv/h. From this value the final monitoring system should be able to derive an estimation of the *H*(10)* value present on top of the facility, in order to guarantee to the authorities that the maximum limits are not exceeded. This will have to be based on empirical calculations performed by knowing the shielding thickness, complemented by the results obtained from Monte Carlo simulations.

The measurements performed at the injector test facility at PSI showed that LUPIN is an excellent candidate for the future BLM system that will be installed in the SwissFEL accelerator complex. In fact, due to its unique properties, it will be capable of providing information both on the intensity and the position of the beam losses in the accelerator, in order to identify possible problems or component malfunctioning, and data useful both for the protection of the personnel working in the facility and to extract information for the dose delivered to the public on top of the facility. Moreover,

its ability to operate over a wide dynamic range, allows it to precisely derive the intensity of the beam losses induced by both the particles accelerated in normal operating conditions and by the dark current. 30 LUPIN detectors could be potentially installed in the new SwissFEL once the commissioning will be completed. This is an estimation based on the number of critical points where the physicists expect the highest losses to happen accord to the machine design. Further investigations are needed in order to understand how the data obtained from the LUPIN detectors could be analysed in order to extract information on the location, the intensity and the time structure of the losses, how these data could be used to derive information on the dose delivered to the public, and how the instruments could be efficiently integrated in the central monitoring system

### 3.3. Supporting non-intrusive beam monitoring

In the view of the potential applications of LUPIN around particle accelerators as a BLM and as a versatile monitor providing information to be used for radiation protection purposes, its use as complementary detector for non-intrusive beam monitoring techniques should also be considered. This application is attracting widespread interest in the last years, since its implementation could result many advantages that could reflect on the accelerator operation and efficiency. For example, if we restrict the field to hadrontherapy accelerators, one of the problems still open is the development of effective non-intrusive devices for online beam monitoring. The ideal detector should produce negligible effects on the few nA clinical beam and should have a beam current measurement resolution of few percent [Badano et al. 1999]. Up to present this has not been possible, since existing interceptive monitors interfere with the beam, thus causing significant beam disruption at therapeutic kinetic energies. At the same time non-interceptive instrumentation is not sensitive enough to detect average beam intensities varying from a few pA to a few nA, with extracted beam duration of the order of 1 s [Badano et al. 2007], i.e. the typical characteristics of a clinical beam extracted from hadrontherapy accelerators. This open issue will lead in the future to the development of a comprehensive system constituted by different detectors to be integrated into the treatment beam line. This system should in principle be able to detect all the beam parameters such as position, intensity and dose profile in a non-intrusive way.

The development of this system should foresee the presence of a monitor installed around the beam line axis in order to collect data from the halo constituted by the particle surrounding the accelerated beam, whose shape is typically Gaussian, and another detector located around the accelerator in order to extract information from the radiation bursts generated by the beam losses after

the interaction of the primary beam with the surrounding structures. An example of the first type of detector could be the instrument proposed in a recent study by Cybulski et al. [Cybulski et al. 2012]. Through an innovative method the LHCb VErtex LOcator (VELO) detector has been integrated into a treatment beam line at the Clatterbridge Centre for Oncology, a hadrontherapy accelerator where a 60 MeV proton beam is used for eye cancer therapy. The operating principle of this detector is based on the fact that the proton halo region hit rate which impinges on the VELO monitor can be related via a conversion curve to the absolute beam current. Thereby, halo signal-dose mappings shall be determined to allow for a true online monitoring system during patient treatment. However, studies to determine the reliability of this signal cross correlation are still ongoing. The second detector could be constituted by LUPIN-BF that, acting as an efficient BLM, could precisely measure the location of the beam losses in the accelerator, and the intensity and the temporal structure of the radiation bursts generated by their interaction with the surrounding structures. From these data it could then extract useful information on the beam intensity, and could hence act as a cross-check monitor to complement the information obtained by the main on-line monitoring system, playing at the same time an essential role for beam diagnostics, for radiation protection purposes and for the machine protection system.

It cannot be excluded that these two detectors should be complemented by other instrumentation primarily used for other purposes but whose data could be efficiently employed to extract precious information on the main characteristics of the primary beam. This is however a pure speculation for the time being, since the design and the implementation of such a system would require a first conceptual phase, followed by test to be performed in dedicated measurement campaigns and the related optimization of the different components of the system.

**Chapter summary**

This chapter describes the potential application of LUPIN as a versatile BLM around particle accelerators. Two measurement campaigns are presented, in which the detector has been tested in order to verify its capability of detecting PNF: the first performed around a synchrotron used for proton therapy and the second carried out in an FEL accelerator. The potential application of LUPIN as a detector supporting least intrusive beam monitoring techniques was also discussed, by presenting the possibility of implementing it in a more complex detector phantom in order to derive from the accelerated beam the highest number of parameters possible by limiting at minimum the perturbing effects.

# 4. Neutron spectroscopy

Among the several applications for which the electronics used in LUPIN could be efficiently employed for radiation protection purposes, a very promising one consists in using it as the analysing electronics for a multi-sphere spectrometer, usually called Bonner Sphere Spectrometer (BSS). Indeed the usual acquisition chain adopted for analysing the signal obtained with a BSS consists of a preamplifier, an amplifier, a single channel analyser (SCA) and a counter, from which the total number of counts acquired from each sphere is then derived. This electronics is affected, as for every conventional neutron rem counter, by the saturation effects induced by dead time losses and therefore it cannot be efficiently employed in PNF and, more generally, in conditions of intense neutron fields characterised by a very high interaction rate in the proportional counter. The electronics employed in LUPIN directly collects the signal from the proportional counter and converts it to the number of neutron interactions, i.e. to the number of counts, following the procedure explained in Section 2.1. The BSS takes its name from one of authors who published the first paper about its description [Bramblett et al. 1960] and it is one of the most employed instruments for neutron spectrometry, which shows a number of advantages if compared to other methods like wide energy range and isotropic response. The technique consists in using a thermal neutron detector surrounded by several moderating spheres of varying size. If the BSS employs a $^{3}$He proportional counter as the thermal neutron detector, the system shows additional advantages such as high sensitivity, simple acquisition electronics and good discrimination properties when employed in mixed neutron/photon fields [Esposito and Nandy 2004]. The neutron spectrum is derived by unfolding the counts obtained from the spheres, normalised to a reference quantity, with their response matrix. The response matrix is calculated via a Monte Carlo code and it is expressed as the number of counts per unit of fluence as a function of the impinging neutron energy. Obtaining accurate results from a BSS is strictly related to a good estimation of the measuring uncertainty and to the availability of a well-established response matrix, calculated on a consistent number of energy bins and verified in reference neutron fields. In addition, attention must be paid to the correct use of the unfolding code [Barros et al. 2014]. The BSS currently owned by the radiation protection group at CERN has been modified in order to use the LUPIN electronics to analyse the collected signal so that the system could be efficiently employed for measuring the neutron spectrum in PNF. Section 4.1. describes the present CERN BSS and shows how the response matrix has been

calculated. Section 4.2. explains the modification introduced in the system in order to extend its use in PNF. Section 4.3. reports the data obtained in two measurement campaigns with the present CERN BSS and the modified one, in which the results have also been compared with measurements performed with neutron *H*(10)* meters.

### 4.1. The CERN Bonner Sphere Spectrometer

The CERN BSS consists of seven spheres, as shown in Fig. 38: five polyethylene spheres with outer diameter of 81, 108, 133, 178 and 233 mm, complemented by two other spheres, nicknamed *Ollio* and *Stanlio*, where cadmium and lead inserts were introduced in order to reduce the sensitivity to thermal neutrons and increase it for high energies, up to the GeV range. The spheres are usually identified by mentioning the polyethylene diameter and the two nicknames, *Ollio* and *Stanlio*. The 81 mm sphere can be employed with an outer 1 mm thick cadmium shell to suppress its response to thermal neutrons, thus effectively making the response matrix composed by eight, partially independent, functions. The system also includes aluminium supports that keep the sphere in a stable measuring position, some polyethylene fillers and the electronics for acquiring the signal.

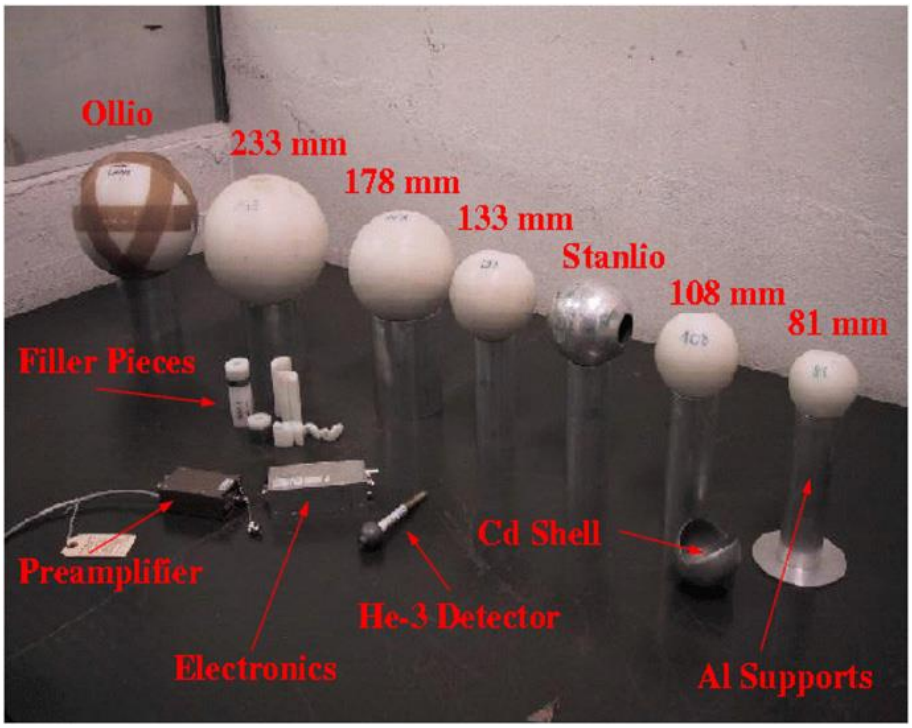


FIG. 38. The CERN BSS: spheres, supports, detector, filler pieces and electronics.

The geometry of the 81 mm sphere is shown in Fig. 39. For the other four polyethylene spheres the geometry is very similar, except for the polyethylene thickness, which is obviously different.

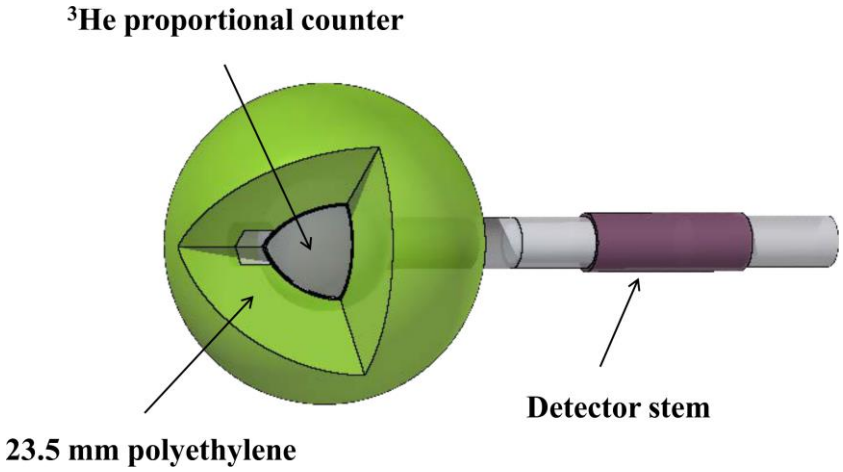


FIG. 39. Geometry of the 81 mm sphere of the CERN BSS.

For simplicity the moderating material is represented as a single uniform piece of polyethylene surrounding the $^3$He proportional counter. Indeed it is composed of several pieces: a hollow sphere and four fillers. The sphere is partially hollow (cylindrical cavity of 40 mm diameter) in order to host at its centre the counter and its stem, which contains the cable for providing the high voltage to the counter and for transporting the signal to the preamplifier. The residual voids are filled with four fillers in which the counter is enclosed before being inserted in the sphere: two enclose the spherical part, whereas two enclose the stem and have variable length depending on the sphere diameter. These have been slightly modified compared to the past system described in ref. [Birattari et al. 2010] in order to accommodate an additional rubber layer which is present in the new version of the $^3$He counter, indicated in violet in Fig. 39. The geometries of *Ollio* and *Stanlio* are given in Fig. 40.

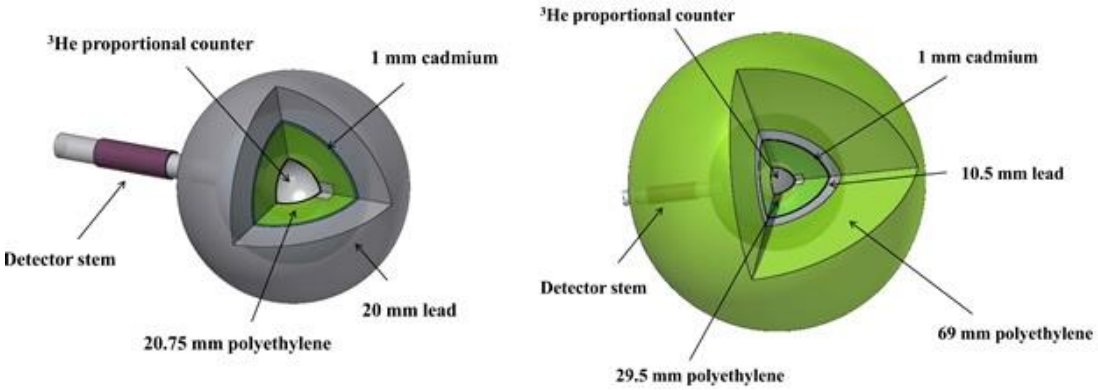


FIG. 40. Geometry of *Ollio* (right) and *Stanlio* (left) of the CERN BSS.

The fillers used for *Ollio* and *Stanlio* are composed of polyethylene, cadmium and lead and are designed in order to create uniform shells of material surrounding the $^3$He counter once it is inserted in the sphere.

The polyethylene density to be used in the Monte Carlo simulations for calculating the response matrix was measured via the water displacement technique and was found to be equal to 0.96 ± 0.01 g/cm$^3$. The lead purity was also checked via measurements performed with a portable optical emission spectrometer, PMI-MASTER Pro by Oxford Instruments, which provided a composition averaged over five samples of 99.8 % Pb, 0.05 % Sn and negligible contamination of other materials. A lead purity of 100% was then assumed for the simulations, as this approximation introduces negligible uncertainties. The $^3$He proportional counter is the same used for LUPIN-He, i.e. a spherical Centronic SP9He3/152/Kr $^3$He, characterised by a nominal pressure of 1520 mmHg (202,650 Pa) and 200 mmHg (26,664 Pa), respectively. However the actual pressure is 1748 mmHg (233,047 Pa), to which 912 mmHg (121,590 Pa) of Krypton is added as a quench gas [Sutter 2011]. An air gap of 0.5 mm exists between the counter and the fillers, intended as the average difference between the external radius of the counter and the internal radius of the filler.

The latest available version of the response matrix of the CERN BSS was calculated with the 1998 version of the FLUKA Monte Carlo code. The results showed limitations in terms of relatively high statistical uncertainties and reduced number of energy bins below 20 MeV. These issues are due to the limited computing power of the time and to limitations of that version of FLUKA, whose libraries had only 72 values of cross sections for neutron energies below 20 MeV, whereas the latest version has 260 values of approximately equal logarithmic width, 31 of which in the thermal region. Dedicated simulations were performed with the version 2011.2b.5 in order to recalculate the response matrix, by following the same methodology explained in ref. [Birattari et al. 2010]. The response of a sphere is defined for each energy $E_i$ of the impinging neutrons as:

$$R(E_i) = \frac{N_{atom} \cdot \sum_{E_j=0eV}^{E_j=\infty} \Delta x(E_j) \cdot \sigma(E_j)}{F_u} \qquad (20)$$

where $N_{atom}$ is the $^3$He atomic density (cm$^{-3}$), $\Delta x(E_j)$ is the track length of the neutrons in the proportional counter (cm), calculated by FLUKA for each energy $E_j$ of the neutrons entering the active volume, $\sigma(E_j)$ is the cross section of the reaction $^3$He(n,p)$^3$H (cm$^2$), and $F_u$ is the normalisation quantity, i.e. the fluence of neutrons impinging on a surface perpendicular to the sphere (cm$^{-2}$): $F_u = 1/4 \cdot r^2$, where r is the sphere radius. Thanks to a FLUKA routine, the user obtains the result of equation (20) for the 260 energies by

running one simulation. Above 20 MeV any additional energy $E_i$ needs a dedicated simulation to be run. The gas mixture density was 0.004369 g/cm$^3$. The cross section applied to hydrogen in polyethylene was the default one for $CH_2$, as defined by FLUKA, and free gas natural carbon for carbon. Two PHYSICS cards were used, one for coalescence and one for the new evaporation model. The response functions have been calculated for neutron energies up to 2 GeV and are showed in Fig. 41. The Monte Carlo statistical uncertainties are not shown for clarity.

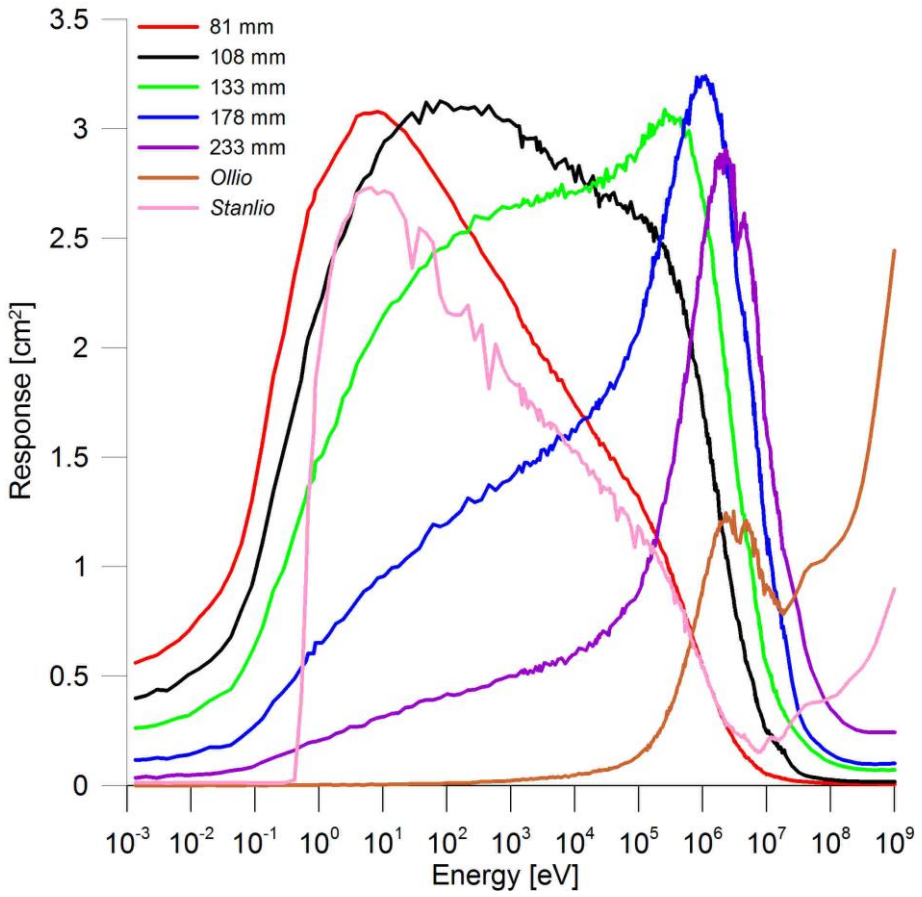


FIG. 41. Response functions calculated for the CERN BSS with the FLUKA code, expressed in counts per unit of fluence as a function of the impinging neutron energy.

The results of the simulations did not significantly change neither the shape nor the values of the response functions obtained in the past, but improved the energy resolution and consistently reduced the statistical uncertainties over the entire energy range.

### 4.2. The BSS-LUPIN

The CERN BSS has been employed in the past in several radiation environments but its use has always been avoided in PNF due to the dead time losses that would affect the measurements and would lead to an underestimation of the number of integrated counts. This issue is particularly severe in the case of the electronics used for acquiring the signal of the CERN BSS, since it can be modelled as a paralysable system. In principle correction algorithms capable of deriving the true interaction rate from the measured one exist also for non paralysable systems. They are based on the following expression:

$$m = n \cdot e^{-nD} \tag{21}$$

where m is the measured interaction rate, n is the true one and D is the dead time [Knoll 2010b]. However, the correction algorithms can be applied only in case of steady-state radiation fields of constant intensity, but not for measuring in PNF, where, by definition, the interaction rate is not constant in time. In order to extend the use of the CERN BSS in radiation environments characterised by the presence of PNF, the LUPIN electronics has been employed to analyse the signal obtained from the proportional counter an to derive the integrated number of counts from each sphere without being affected by dead time losses. This profits from the same working principle at the basis of LUPIN-He, except for the fact that the integrated number of counts is not be proportional to the neutron *H*(10)* but it is used in the unfolding procedure to derive the neutron spectrum in the measuring area. As in LUPIN-He, an electrostatic shielding must surround the $^{3}$He counter in order to avoid noise pick up. Therefore the geometry of each sphere needs to be slightly modified in order to host at its centre an aluminium cylinder of 1 mm thickness which surrounds the proportional counter and the fillers. The system with this modified geometry has been called BSS-LUPIN. Fig. 42 shows the geometry of the 233 mm sphere.

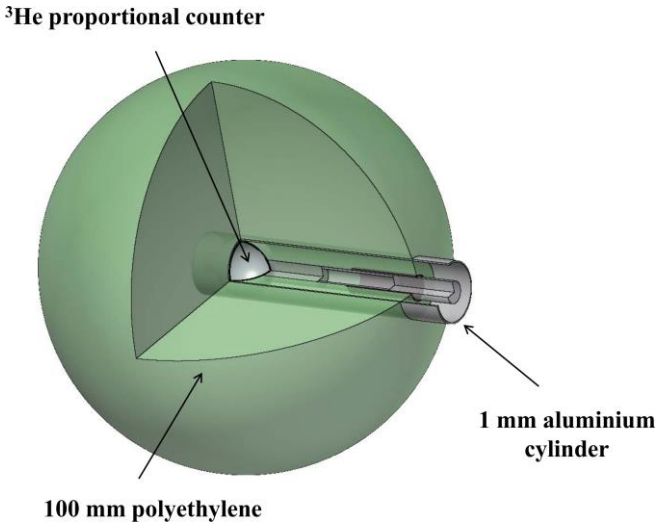


FIG. 42. Geometry of the 233 mm sphere of the BSS-LUPIN.

The geometry for the other six spheres is very similar since the only difference is the insertion of the 1 mm tube and the corresponding reduction of the diameter of the polyethylene fillers. FLUKA simulations showed that the insertion of the aluminium cylinder in the spheres does not significantly change the response matrix. Fig. 43 shows a comparison between the response function calculated for the 81 mm sphere employed for the CERN BSS and the BSS-LUPIN.

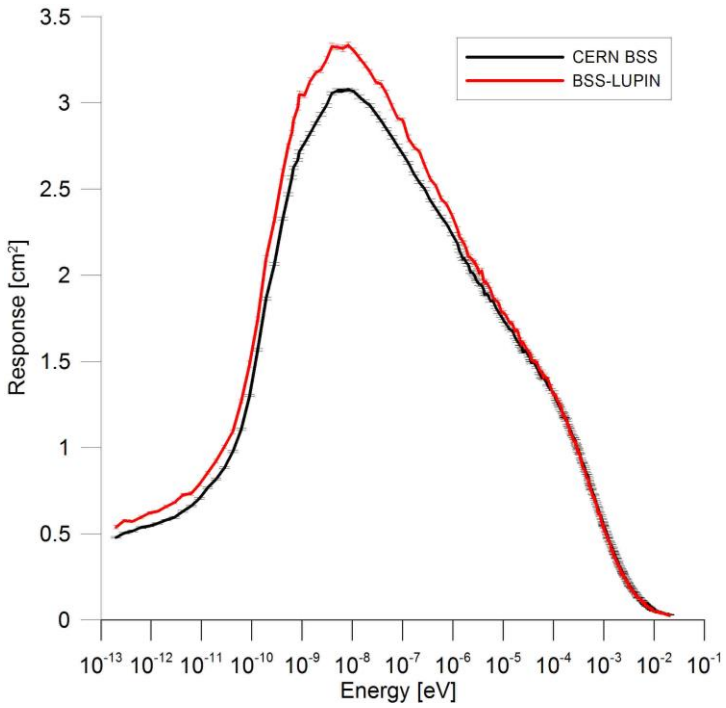


FIG. 43. Comparison between the response function obtained for the 81mm sphere for the CERN BSS and for the BSS-LUPIN.

This is the only case in which the insertion of the aluminium tube slightly increases the sensitivity for energies of few eV. This is reasonable since aluminium has a high neutron transmission factor, even if the interaction probability is enhanced below 200 keV due to cross section resonances [Reillo 2008]. On the other hand, the geometry in which the neutrons traverse the biggest relative fraction of aluminium thickness on the overall path needed to reach the $^{3}$He counter is the 81 mm sphere.

### 4.3. Measurements

The BSS-LUPIN has been employed to measure the neutron spectrum in two measurement campaigns in order to test its reliability. The first one was performed in a proton therapy centre inside a treatment room in selected positions, while the second campaign took place at the CERN Proton Synchrotron close to the beam extraction area. In the first case the stray field was not pulsed but the interaction rate was very high so that the conventional CERN BSS could have been affected by dead time losses, whereas in the second case the radiation environment was characterised by the presence of a PNF. In the latter case both systems, the BSS-LUPIN and the standard CERN BSS, were used in the same reference position, so that a direct comparison between the obtained results became possible.

#### 4.3.1. Measurements in a proton therapy centre

A series of measurements was carried out at the *Westdeutsche Protonentherapiezentrum*, a proton therapy centre located in Essen, Germany, in selected positions inside a fixed beam treatment room. The measurements were performed in the framework of a larger intercomparison of passive and active instrumentation, whose results have been compared with Monte Carlo simulations. The attention will be focused here only on the results obtained with the BSS-LUPIN and with two rem counters employed for comparison, i.e.Wendi-2 and LB6411, see Appendix for a comprehensive description of their working principle. Fig. 44 shows a sketch of the treatment room and the reference positions selected for the intercomparison. The measurements were performed with BSS-LUPIN in positions 1a, 1b, 2a and 1g.

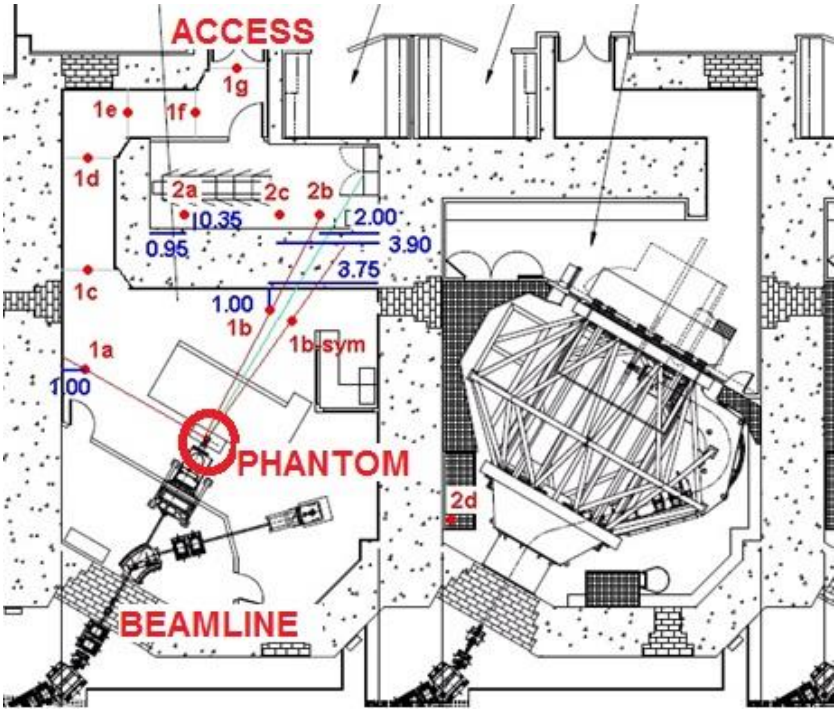


FIG. 44. Fixed beam treatment room at the proton therapy centre in Essen. The red spots indicate the reference positions.

Positions 1a and 1b are located in the treatment hall: 1b is in the same direction of the beam line, where the highest intensity of the stray field is expected, whereas position 1a is placed at 90º aside. Position 2a is located in a technical room shielded from the main hall by a concrete wall: the expected stray field intensity is therefore lower and characterised by a lower average energy. Position 1g is located at the beginning of the access maze, where only scattered neutrons can be detected and where the expected stray field intensity is the lowest. All positions are located beyond an interlocked door and are not accessible during treatment. The measured neutron spectrum should nevertheless provide information on the characteristics of the stray neutron field beyond the shielding, where the operators usually perform their work. The measurements were performed by placing in turn the seven spheres of the BSS-LUPIN in each of the positions at the beam isocentre height. Fig. 45 shows the experimental set-up for the measurement performed with the 233 mm sphere in position 1a: the sphere and its support are installed on a trolley and the signal is collected via a Bayonet Neill-Concelman (BNC) cable which brings it beyond the interlocked door where the acquisition PC was installed.

FIG. 45. Experimental set-up for the measurement performed with the 233 mm sphere in position 1a at the Essen proton therapy centre.

A 230 MeV proton beam was delivered on a Poly-methyl methacrylate (PMMA) phantom placed on the treatment coach. The counts were integrated for each sphere until the statistical uncertainty fell below 1% and were normalised to the intensity of the proton beam, which was monitored by an ionisation chamber. The results are given in Table XI.

Table XI. Data obtained with BSS-LUPIN at the Essen proton therapy centre, expressed in counts normalised per proton delivered on the phantom (uncertainty in parentheses).

| Sphere | Position | | | |
|---|---|---|---|---|
| | 1a | 1b | 1g | 2a |
| 81 mm | $2.05 \pm 0.10 \cdot 10^{-7}$ | $3.56 \pm 0.18 \cdot 10^{-7}$ | $1.10 \pm 0.06 \cdot 10^{-9}$ | $7.68 \pm 0.39 \cdot 10^{-7}$ |
| 108 mm | $2.94 \pm 0.15 \cdot 10^{-7}$ | $4.64 \pm 0.23 \cdot 10^{-7}$ | $1.06 \pm 0.05 \cdot 10^{-9}$ | $8.93 \pm 0.45 \cdot 10^{-7}$ |
| 133 mm | $3.09 \pm 0.15 \cdot 10^{-7}$ | $5.12 \pm 0.26 \cdot 10^{-7}$ | $8.88 \pm 0.45 \cdot 10^{-10}$ | $9.22 \pm 0.47 \cdot 10^{-7}$ |
| 178 mm | $2.50 \pm 0.13 \cdot 10^{-7}$ | $4.44 \pm 0.22 \cdot 10^{-7}$ | $5.93 \pm 0.30 \cdot 10^{-10}$ | $7.94 \pm 0.40 \cdot 10^{-7}$ |
| 233 mm | $1.63 \pm 0.08 \cdot 10^{-7}$ | $3.45 \pm 0.17 \cdot 10^{-7}$ | $3.37 \pm 0.18 \cdot 10^{-10}$ | $5.82 \pm 0.30 \cdot 10^{-7}$ |
| *Stanlio* | $1.38 \pm 0.07 \cdot 10^{-7}$ | $2.32 \pm 0.12 \cdot 10^{-7}$ | $4.33 \pm 0.23 \cdot 10^{-10}$ | $4.37 \pm 0.23 \cdot 10^{-7}$ |
| *Ollio* | $5.67 \pm 0.03 \cdot 10^{-7}$ | $1.95 \pm 0.10 \cdot 10^{-7}$ | $1.08 \pm 0.61 \cdot 10^{-10}$ | $2.68 \pm 0.14 \cdot 10^{-7}$ |

The total uncertainty is the sum of the statistical one and the uncertainty on the calibration of the beam monitor, 5%. The data have been unfolded by using three unfolding codes specifically conceived for analysing data obtained by multi-sphere systems: MAXimum Entropy Deconvolution (MAXED) [Reginatto and Goldhagen 1999], GRAVEL [Reginatto and Goldhagen 1999] and FRascati Unfolding Interactive Tool (FRUIT) [Bedogni et al. 2007]. The first two codes, available in the PTB U.M.G. package [Reginatto et al. 2004], require an *a priori* estimation of the neutron spectrum, called guess spectrum, whereas the third relies on a parametric approach which requires the user to define the radiation environment where the measurements are performed by selecting it from a list, and to approximately know the central energy of the spectrum peaks and the relative weight of the neutron fluence integrated under each energy region. For these measurements the high-energy hadron accelerator environment was chosen, by centring the peaks at thermal energy, 5 MeV and 100 MeV. The guess spectrum needed by MAXED and GRAVEL was obtained via simulations performed with the MNCPX [Briesmeister 2000] Monte Carlo code provided by the proton therapy centre. The uncertainties have been calculated for MAXED via the IQU_FC33 program implemented in the U.M.G. package, which, given a solution spectrum generated by the code, considers variations in the measured data and in the guess spectrum and uses standard methods to perform sensitivity analysis and uncertainty propagation. On the other hand, FRUIT performs the uncertainty propagation, for both approaches, by randomly generating a large number ($> 10^3$) of sets of BSS counts and by using the quadratic combination of the counting uncertainty and of the response function as the amplitude of the Gaussian perturbation.

Fig. 46 shows the solution spectra for position 1a, compared to the guess spectrum obtained via the MNCPX code. The fluence is expressed in unit of lethargy and normalised to the number of delivered protons as measured by the beam monitor.

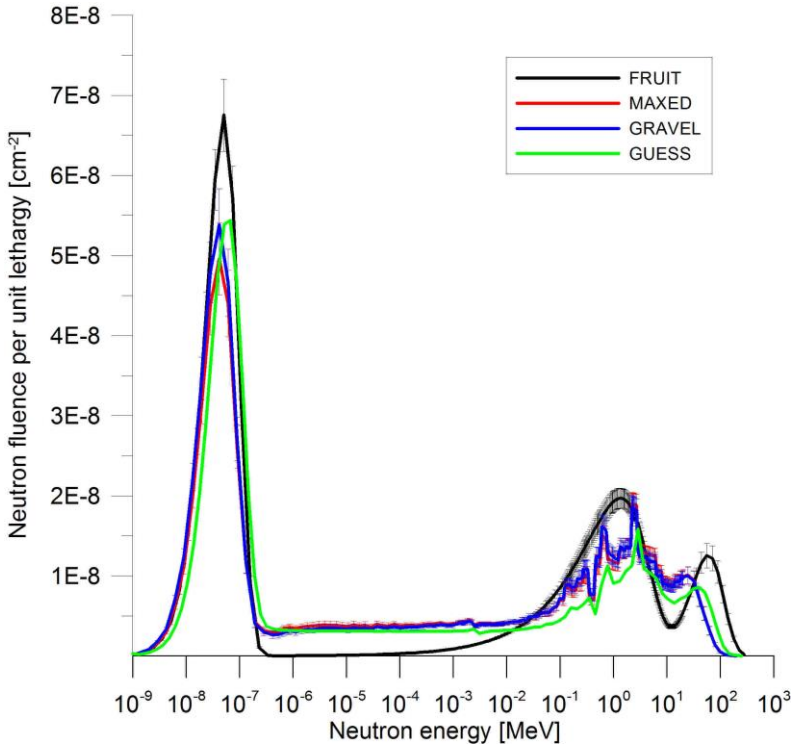


FIG. 46. Neutron spectrum calculated for position 1a at the Essen proton therapy centre with MAXED, GRAVEL and FRUIT, compared with the guess spectrum simulated via MNCPX.

The uncertainties are shown for the solution spectra obtained with MAXED and GRAVEL, whereas they are not shown for the guess spectrum for clarity. The spectra obtained with MAXED and GRAVEL are in good agreement and show the three peaks typical of the surroundings of a hadron therapy accelerator: the thermal peak centred at 0.025 eV, the evaporation peak centred at a few MeV and the high-energy peak, centred at about half of the energy of the primary beam. The presence of the thermal peak is due to the diffusion and thermalisation of the neutrons produced by the interaction of the primary beam in the phantom with the walls and the surrounding structures. The evaporation region is characterised by many secondary peaks, generated by the interaction of the neutrons with iron, which has several cross section resonances for scattering reactions. The high-energy peak has a tail whose maximum is given by the energy of the primary beam: it is in fact possible that a proton of 230 MeV generates, even if with low probability, a neutron of equal energy in its interaction with the phantom. The spectrum calculated by FRUIT shows three peaks but it is smoothed since the code does not need a guess spectrum and therefore it cannot take into account the small modifications introduced by the iron resonances. The peaks are centred on slightly different energies because FRUIT takes the approximate central energies provided by the user as reference. The difference observed between the three codes in the thermal peak are nevertheless of limited importance, as it will be shown later, since

the conversion coefficients from neutron fluence to *H*(10)* are very small in this energy region. From a qualitative point of view, the evaporation peak is higher than the high-energy one because position 1a is located at 90º from the beam line axis and this increases the probability of detecting neutrons that encountered many scattering events, thus reducing their energy. The solution spectra are generally in good agreement with the guess spectrum. The evaporation and the high-energy peaks are almost superimposable one to each other, with the only visible difference limited to the thermal region.

Fig. 47 shows the results for position 1b.

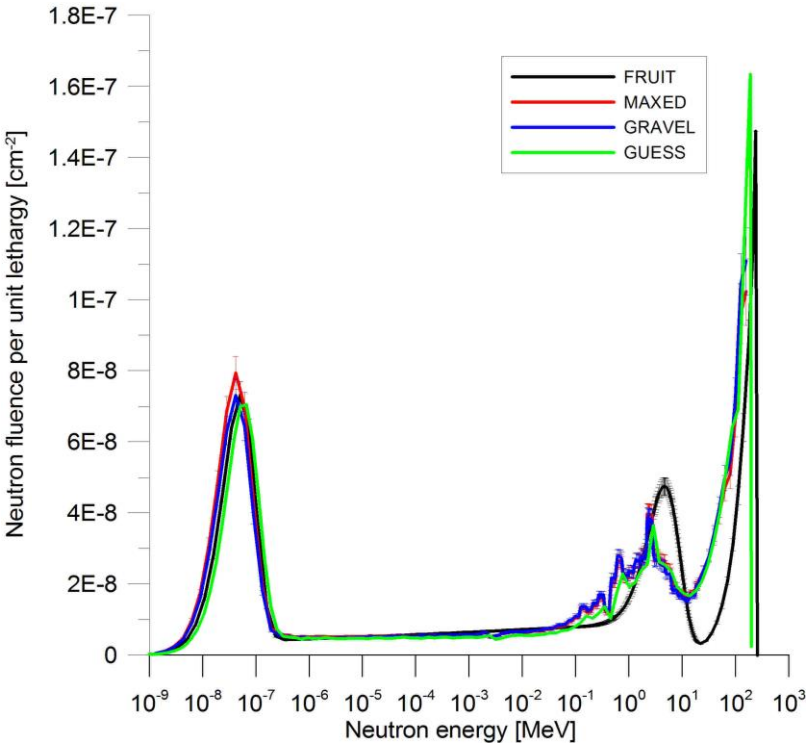


FIG. 47. Neutron spectrum calculated for position 1b at the Essen proton therapy centre with MAXED, GRAVEL and FRUIT, compared with the guess spectrum simulated via MNCPX.

If compared to position 1a the thermal peak in position 1b has a lower intensity while the high-energy peak is consistently higher. This is due to the fact that position 1b is located in the direction of the primary beam and this implies a limited interaction of the detected neutrons with the concrete structures surrounding the accelerator, thus resulting in a lower thermal peak. At the same time the neutrons generated in the phantom have a high probability of travelling free in air for a short path before being detected, thus resulting in an intense high-energy peak. The calculated neutron spectra do not significantly differ from the shape of the guess spectrum, thus confirming the fact that the unfolding procedure modifies the intensity of the peaks of the guess spectrum rather than their shape. The largest

differences between the calculated and the simulated neutron spectrum are in the one calculated with the FRUIT code. This is expected, since the limited amount of *a priori* information needed by the code, if compared to MAXED and GRAVEL, results in a huge simplification of the final shape of the spectrum, which cannot include the small details generated in the evaporation region by the iron resonances.

Fig. 48 shows the results for position 2a.

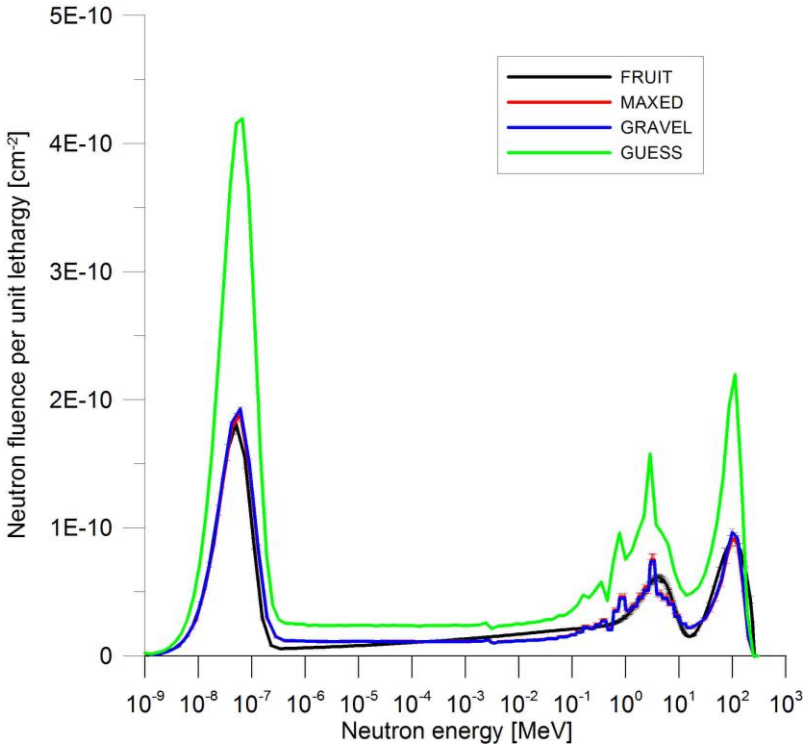


FIG. 48. Neutron spectrum calculated for position 2a at the Essen proton therapy centre with MAXED, GRAVEL and FRUIT, compared with the guess spectrum simulated via MNCPX.

The main difference between the spectra obtained for position 2a and the other positions is the discrepancy present here between the calculated spectra and the guess spectrum, which reaches a factor of 2 in the intensity of the high-energy peak. As an average the fluence intensity is lower by three orders of magnitude than the spectra calculated for position 1b. This is reasonable since position 2a is located in the direction of the beam line as position 1b, but it is shielded by a concrete wall that attenuates the intensity of the neutron fluence and increases the probability of scattering events, thus reducing the high-energy peak and slightly increasing the thermal one.

For the three positions mentioned above, and also for position 1g, whose results have not been shown because they would not add significant information in the context of this discussion, the

measured *H*(10)* per proton impinging on the phantom has been calculated by folding the spectrum with the ICRP fluence to *H*(10)* conversion coefficients [ICRP 1996]. The results are shown in Table XII for the solution spectra obtained with the three unfolding codes, together with the measurements performed with Wendi-2 and LB6411, whose readings have been normalised to the integrated number of protons impinging on the phantom. The measurements performed with the two rem counters lasted for about 10 minutes and the statistical uncertainty on the number of integrated counts was below 1%.

Table XII. Comparison of the *H*(10)* per proton as calculated from the solution spectrum obtained via MAXED, GRAVEL and FRUIT, and as measured with Wendi-2 and LB6411.

| Method | Position | | | |
|---|---|---|---|---|
| | 1a | 1b | 1g | 2a |
| MAXED | $(2.9 \pm 0.4) \cdot 10^{-17}$ Sv/p | $(8.6 \pm 1.2) \cdot 10^{-17}$ Sv/p | $(5.8 \pm 1.0) \cdot 10^{-20}$ Sv/p | $(1.2 \pm 0.2) \cdot 10^{-19}$ Sv/p |
| GRAVEL | $(2.9 \pm 0.4) \cdot 10^{-17}$ Sv/p | $(8.5 \pm 1.2) \cdot 10^{-17}$ Sv/p | $(6.5 \pm 1.1) \cdot 10^{-20}$ Sv/p | $(1.2 \pm 0.2) \cdot 10^{-19}$ Sv/p |
| FRUIT | $(3.3 \pm 0.2) \cdot 10^{-17}$ Sv/p | $(8.1 \pm 0.6) \cdot 10^{-17}$ Sv/p | $(6.2 \pm 0.5) \cdot 10^{-20}$ Sv/p | $(1.3 \pm 0.2) \cdot 10^{-19}$ Sv/p |
| Wendi-2 | $(2.6 \pm 0.5) \cdot 10^{-17}$ Sv/p | $(9.1 \pm 1.8) \cdot 10^{-17}$ Sv/p | $(6.3 \pm 1.3) \cdot 10^{-20}$ Sv/p | $(1.2 \pm 0.2) \cdot 10^{-19}$ Sv/p |
| LB6411 | $(2.4 \pm 0.1) \cdot 10^{-17}$ Sv/p | $(5.5 \pm 0.3) \cdot 10^{-17}$ Sv/p | n.a. | $(0.87 \pm 0.05) \cdot 10^{-19}$ Sv/p |

n.a. = not available

The uncertainties on the rem counter measurements are the sum of the statistical uncertainty, the uncertainty on the beam monitoring and, for Wendi-2 only, the uncertainty on the non-isotropic response. The uncertainty for the solution spectra obtained by MAXED and FRUIT has been calculated by folding the uncertainty of the fluence for each energy bin with the ICRP coefficients. For GRAVEL the relative uncertainty has been assumed to be equal to the MAXED one. The measurement performed with LB6411 in position 1g is not available due to malfunctioning of the detector. The agreement between the normalised *H*(10)* obtained from the calculated spectra is excellent for all positions, thus confirming for MAXED and GRAVEL that when the unfolding is performed by using the same guess spectrum, the final results are very similar. Concerning the FRUIT code, this confirms the reliability of the measurements, since even with a limited *a priori* knowledge on the final spectrum, results

compatible with the MAXED and GRAVEL ones have been obtained. A further confirmation comes from the agreement between the unfolded data and the measurements performed with Wendi-2. The results obtained with LB6411 are about 35% lower for positions 1b and 2a because of its reduced response for neutron energies above 20 MeV, see Appendix. The underestimation is not present for position 1a because of the limited importance of the high-energy peak, as it can be seen in Fig. 46.

The measurements allowed testing the BSS-LUPIN for measuring the neutron spectrum in selected positions in a proton therapy centre. The interaction rate in the proportional counter was high for most spheres, a few $10^6$ $s^{-1}$ as an average, so that the conventional CERN BSS would have suffered from dead time losses, with a consequent underestimation of the integrated number of counts. The system proved to be reliable in the determination of the spectrum in all positions. This is derived from the compatibility between the value of $H^*(10)$ per proton calculated by these spectra and the value measured with the rem counters at the same positions.

### 4.3.2. Measurements at the CERN PS

A measurement campaign was performed with the BSS-LUPIN at the beginning of the access tunnel to SS16 of the CERN PS, i.e. the beam extraction area, identified as location 3 in Fig. 23. The same area was employed to perform the measurements of the intercomparison exercise described in Section 2.2.5. The typical duration of the losses here is 2.1 μs, with an expected fraction of lost beam of 1%. The extraction losses distributed on the overall PS, which are due to the slicing process of the beam, are to be added. The extraction is performed over five turns, each of which lasts for 2.2 μs, resulting in a typical length of the losses of 11 μs. The pulse repetition rate is 0.83 Hz, i.e. one pulse every 1.2 s. The resulting stray radiation field is therefore ideal to test the performance of the BSS-LUPIN in PNF. For comparison the conventional CERN BSS was also employed in the same position. Each sphere was placed in turn in a predetermined position located at about one meter before the interlocked door. This cannot be identified with any of the six positions used for the intercomparison described in Section 2.2.5. because those positions were not accessible. A picture of the experimental set-up used for the measurements with the conventional CERN BSS and the BSS-LUPIN is shown in Fig. 49.


FIG. 49. Experimental set-up for the measurements performed with the 178 mm sphere at the CERN PS: BSS-LUPIN (left) and conventional CERN BSS (right).

The measurements performed with the CERN BSS required the presence of the acquisition electronics close to the detector in order to reduce the noise in the transport of the signal from the detector to the amplifier. For the LUPIN-BSS the signal was transported outside the exposure area into a control room where the acquisitions were performed via a PC that allowed online monitoring. Each measurement lasted for about 30 minutes to minimise the statistical uncertainty. For the CERN BSS the counts were corrected for dead time losses by using equation (1). The measurements were performed with both systems on different days by keeping the type of the accelerated cycles unchanged, from which the intensity and the time structure of the beam losses usually depend. The data is shown in Table XIII.

Table XIII. Data obtained with the CERN BSS and the BSS-LUPIN at PS, expressed in counts normalised to the number of protons accelerated in the machine.

| Sphere | CERN BSS | BSS-LUPIN |
|---|---|---|
| 81 mm | $2.39 \pm 0.13 \cdot 10^{-11}$ | $2.20 \pm 0.12 \cdot 10^{-11}$ |
| 108 mm | $1.69 \pm 0.10 \cdot 10^{-11}$ | $2.38 \pm 0.13 \cdot 10^{-11}$ |
| 133 mm | $1.25 \pm 0.07 \cdot 10^{-11}$ | $2.79 \pm 0.15 \cdot 10^{-11}$ |
| 178 mm | $8.91 \pm 0.55 \cdot 10^{-12}$ | $4.23 \pm 0.31 \cdot 10^{-11}$ |
| 233 mm | $5.00 \pm 0.32 \cdot 10^{-12}$ | $9.39 \pm 0.54 \cdot 10^{-12}$ |
| *Stanlio* | $5.61 \pm 0.35 \cdot 10^{-12}$ | $7.49 \pm 0.45 \cdot 10^{-12}$ |
| *Ollio* | $9.38 \pm 0.76 \cdot 10^{-13}$ | $1.96 \pm 0.40 \cdot 10^{-12}$ |

The global uncertainty takes into account the statistical uncertainties that were always below 1% except for *Ollio*, the uncertainty on positioning and reproducibility of the stray field, as well as the uncertainty on the integrated fluence derived from TIMBER, which was equal to 5%.

The neutron spectrum was calculated by unfolding the measured data with three codes: MAXED, GRAVEL and FRUIT. The guess spectrum needed by MAXED and GRAVEL was taken from ref. [Damjanovic et al. 2012], where the neutron spectrum was obtained via FLUKA simulations for a location close to the measuring area. However, since the guess spectrum was normalised to the number of lost protons and the measured counts have been normalised to the accelerated protons, a fraction of 1% of beam lost in the area was estimated in order to relate the two quantities. Since the attention is here focused on the comparison between the performance of the two BSS systems in the same stray field conditions, Fig. 50 shows the comparison between the solution spectrum obtained only with MAXED for the two systems, whereas the results obtained with GRAVEL and FRUIT are not given for clarity. The uncertainties have been calculated via the IQU_FC33 program implemented in the U.M.G. package.

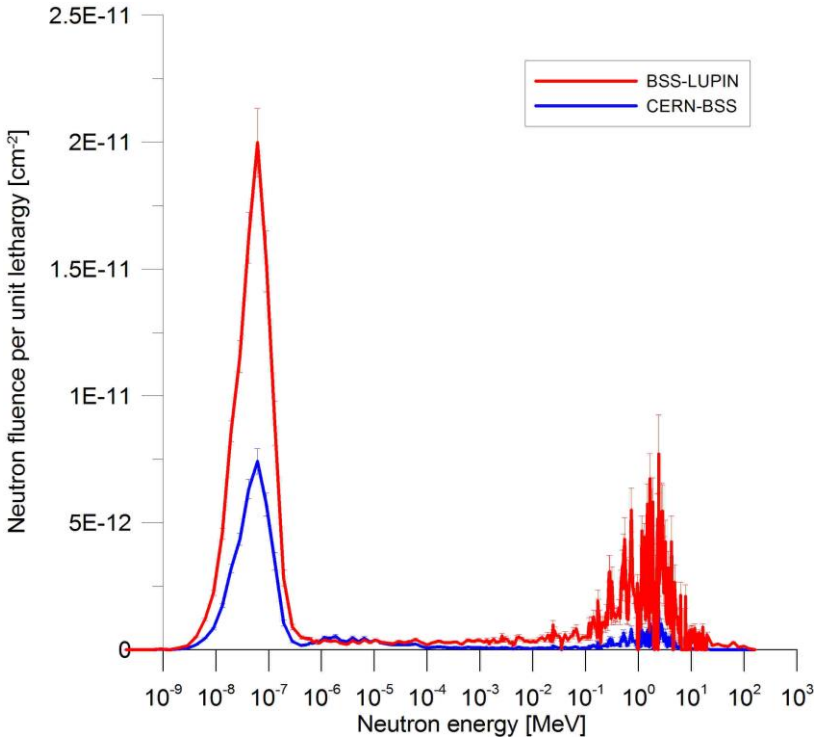


FIG. 50. Spectrum calculated at PS for the measurements performed with the CERN BSS and the BSS-LUPIN, unfolded with MAXED.

The spectra are characterised by a high intensity peak at thermal energies and by several low intensity peaks in the MeV region. This region is particularly jagged due to the high uncertainty of the guess spectrum, which depends on the limited reliability of the Monte Carlo simulations when the expected neutron fluence is very low. The fluence integrated in the intermediate region, from 1 eV to few hundred keV, is negligible. The presence of an intense thermal peak and the limited fluence above 1 eV was expected, since the stray field at the beginning of the PS access tunnel, which is bent and 50 m long, is characterised by neutrons that encountered many scattering events along the concrete walls, thus substantially reducing their energy. Similarly, the probability of a high-energy neutron to reach the measuring position is limited.

Both spectra have a similar shape, whereas the absolute intensity, especially in the thermal and in the MeV region, is substantially different. The CERN BSS spectrum has a thermal peak whose maximum reaches $8 \cdot 10^{-12}$ cm$^{-2}$, consistently lower than for the BSS-LUPIN, whose peak reaches $2 \cdot 10^{-11}$ cm$^{-2}$. For the MeV region it is difficult to define an average value, but the BSS-LUPIN spectrum shows an intensity which is approximately double of the CERN BSS one. The solution spectrum obtained from the CERN BSS consistently underestimates the fluence if compared to the BSS-LUPIN one. This was expected, since the pulsed structure of the stray field present in the measuring location leads to huge underestimation of the integrated number of counts for the CERN BSS. The underestimation is more important as the true interaction rate is higher, i.e. for the spheres which show a high sensitivity in the thermal or in the MeV region. The underestimation introduced the CERN BSS is even more evident if one calculates the normalised *H*(10)* per accelerated proton, see Table XIV. The results are given here for the three unfolding codes used in this study.

Table XIV. Comparison of the *H*(10)* per accelerated proton in the CERN PS as calculated from the neutron spectrum obtained via MAXED, GRAVEL and FRUIT.

| Unfolding code | CERN BSS | BSS-LUPIN |
|---|---|---|
| MAXED | $(6.3 \pm 1.0) \cdot 10^{-13}$ Sv/p | $(3.8 \pm 0.6) \cdot 10^{-12}$ Sv/p |
| GRAVEL | $(6.0 \pm 0.9) \cdot 10^{-13}$ Sv/p | $(4.8 \pm 0.8) \cdot 10^{-12}$ Sv/p |
| FRUIT | $(6.1 \pm 0.3) \cdot 10^{-13}$ Sv/p | $(3.0 \pm 0.3) \cdot 10^{-12}$ Sv/p |

The normalised *H*(10)* has been calculated by folding the average fluence value of each energy bin of the neutron spectrum with the corresponding ICRP fluence to *H*(10)* conversion coefficients [ICRP

1996]. The uncertainty for the solution spectra obtained by MAXED and FRUIT has been calculated by folding the uncertainty of the fluence for each energy bin with the ICRP coefficients. For GRAVEL the relative uncertainty has been assumed to be equal to the MAXED one. The agreement of the results obtained from each system with the three codes is very good: the values are in fact coherent within their range of uncertainties, except for the results obtained with FRUIT for the BSS-LUPIN. This could be due to the fact that FRUIT is a parametric code that does not need a guess spectrum to derive the solution spectrum and this could lead to highest deviations from the results obtained from the other two codes, even in terms of normalised *H*(10)*. The spectra obtained with the BSS-LUPIN show a value higher by a factor of 6 if compared to the CERN BSS. This is a consequence from the fact that the CERN BSS suffers from saturation induced by dead time losses since the interaction rate in the proportional counter is very high. This causes an underestimation of the number of counts for the spheres which have the highest sensitivity in the area and an underestimation of that fraction of the neutron fluence in the final spectrum. For CERN BSS the lowest intensity of the thermal and the high-energy peaks observed in the unfolded spectra results in a huge underestimation of the *H*(10)*, about 80% as an average between the value calculated with the three codes. In order to assess if the BSS-LUPIN is more reliable than the conventional one in this PNF, one can compare these data with the measurements performed with neutron *H*(10)* meters, described in Section 2.2.5. The Hydrogen, the Argon-filled ionisation chamber and LUPIN-BF measured an *H*(10)* included in the range $2.2\text{-}4.3 \cdot 10^{-12}$ nSv per accelerated proton, see Table VII. Therefore, even the position in which the BSS has been used cannot be identified with any of the positions 1-6 of the other campaign. The value calculated from the BSS-LUPIN spectra seems more realistic than the CERN BSS one, which is clearly underestimating the total *H*(10)*.

The measurements allowed comparing the performance of the BSS-LUPIN with the CERN BSS in a stray field characterised by a pulsed structure. The results show that the conventional system suffered from saturation losses and this reflected in an underestimation of the average *H*(10)* normalised per proton accelerated in the PS. On the other hand the spectrum obtained by unfolding the BSS-LUPIN data showed a much more intense thermal and high-energy peak, giving an *H*(10)* value which is included in the range obtained by measurements performed with several neutron *H*(10)* meters in the same area. This confirmed the reliability of the LUPIN electronics which can extend the application of the BSS in PNF.

**Chapter summary**

This chapter describes how the BSS owned by the CERN radiation protection group has been modified by implementing the LUPIN electronics in order to acquire the signal produced in each sphere and derive the number of integrated counts. This upgraded system, called LUPIN-BSS, will allow its efficient operation in PNF. An explanation of the physical properties of the LUPIN-BSS is given, together with a description of the Monte Carlo simulations performed to calculate the response matrix. Two measurement campaigns were also presented, in which BSS-LUPIN has been employed to test its performance in stray fields characterised by different time structures and expected interaction rates. In the second campaign, the one characterised by the most intense PNF, both systems, the conventional CERN BSS and the BSS-LUPIN, have been employed in order to compare the neutron spectra obtained after the unfolding process in the two cases.

# 5. Conclusions and future improvements

## 5.1. Conclusions

The combination of a front end electronics based on logarithmic amplification and a new technique to analyse the signal obtained from the charges generated by neutron interactions in a proportional counter, either $^{3}He$ or $BF_3$, allowed developing a number of neutron detectors that can be efficiently employed in PNF, without suffering from the issues typically encountered in state-of-the-art instrumentation when used in these radiation environments. A comprehensive study into three different devices was carried out in the frame of this thesis: the rem counter LUPIN, a novel beam loss monitor and a neutron spectrometer, BSS-LUPIN. All three were tested during several measurement campaigns under various radiation conditions to critically assess their performance in comparison to commonly used devices and optimise their overall features.

It was found that LUPIN is a highly reliable rem counter that can be employed in steady-state high-energy mixed fields. Its ability to correctly assess the neutron *H*(10)*, in accordance with the results obtained by other commercial rem counters and as estimated in Monte Carlo simulations, was successfully demonstrated. It did not suffer from any saturation effects induced by dead time losses when exposed in a reference PNF with a maximum intensity of 150 nSv per burst. Underestimation effects started to appear only when the detector was exposed to extremely intense PNF encountered e.g. close to the dump of the CERN SPS primary beam. There, space charge effects induced in the proportional counter by the impinging neutron burst caused a maximum underestimation of 30% for an expected *H*(10)* of the incoming neutron field of about 5 µSv per burst, far beyond any limit of interest for radiation protection purposes. However, this measurement proved the possibility of efficiently employing the detector also for machine protection in the context of its use as a beam loss monitor. On the other hand, when employed for measuring the neutron *H*(10)* in operational radiation protection conditions, its performance is comparable, within the range of uncertainties, with that of pressured ionisation chambers, i.e. detectors that by definition do not suffer from any dead time losses since they work in current mode. However, these are affected by other drawbacks that limit their use for routine measurements. Eventually, LUPIN's photon/neutron discrimination properties were found to be excellent both in steady-state and in PNF. In fact, by implementing simple algorithms in the acquisition interface, the photon contribution can be easily discriminated and excluded from the final calculation

of the charge generated in the proportional counters. This assured its proper functioning in virtually all situations usually encountered for radiation protection purposes focused on the determination of the neutron *H*(10)*.

The application of a detector based on the LUPIN electronics as beam loss monitor in a particle accelerator was tested at a hadron accelerator complex, as well as at a Free Electron Laser facility. In both cases, measurements showed that this instrument can be extremely useful in providing important information that can be used at the same time for radiation protection and for beam loss monitoring purposes. As an additional advantage it was shown that it can provide information that usually needs to be derived from several different instruments, thus simplifying overall diagnostics.

A neutron spectrometer constituted by seven Bonner spheres, modified to operate with the LUPIN acquisition electronics, was also tested in PNF and compared with a standard system based on conventional signal analysis, where pre-amplification of the signal is followed by amplification before passage to the discriminator and the counter. This LUPIN-BSS detector correctly estimated the neutron spectrum, as well as the total *H*(10)* as predicted in Monte Carlo simulations and as confirmed by measurements with other rem counters. Moreover, the tests carried out within the frame of this PhD project confirmed that a conventional analysis would have led to a significant underestimation across the entire neutron energy range, thus leading to substantial errors in the determination of the final averaged *H*(10)*.

### 5.2. Future improvements

Some aspects of the devices developed in the framework of this thesis require additional studies in order to further improve their performance; in particular in the view of a possible commercialisation of the detector.

The calculation of the number of neutron interactions and of the neutron *H*(10)* rate is currently performed online for all devices via a purpose-programmed LabVIEW interface. This requires a connection between the detector and a PC via BNC cable. This drastically limits the possibility of using the devices as portable instruments. It would be desirable to have a portable display embedding a microprocessor next to the detector so that the calculations could be performed without the need of external instruments. This way, the user would have a direct indication of the *H*(10)*. This microprocessor would then allow setting all basic parameters needed for detector operation, such as

calibration factors, directly via the display. Since it was found that an acquisition frequency of 10 MHz is a good compromise suitable for most measuring conditions, a Field Programmable Gate Array (FPGA) could be used for this purpose with its frequency set to this fixed value. This would not exclude the possibility of designing a second parallel channel that could be used for a PC connection to conduct tests or for providing TTL signals representing the total number of detected neutron interactions.

As the prototypes described in this thesis show good potential for becoming commercial devices, further investigations into conformity with international standards for neutron detectors should be performed. One of the key documents is the International Electrotechnical Commission report on radiation protection instrumentation [IEC 2014]. It determines the characteristics that a neutron detector for radiation protection applications should fulfil. Most of the requirements concern the dependence of detector performance on variations of the external conditions in which it is employed, and these should *a priori* be easily respected. However, dedicated tests would need to be carried out to confirm this assumption.

LUPIN has proven to be able to efficiently discriminate the photon from the neutron-induced deposited charge in the proportional counter in different stray field conditions via the use of different discrimination techniques. This must currently be selected by the user on the basis of knowledge of the stray field conditions in which the measurements are performed. However, it would be desirable to implement an automatic selection of the proper discrimination technique. Such selection could be triggered by measurements performed using a photon probe installed on top of the detector. Future investigations should determine the desirable characteristics of such a probe and how the electronics should deal with the parallel acquisition of both channels.

It was shown that an instrument based on the LUPIN electronics could be applied as a versatile beam loss monitor in a particle accelerator environment. However, additional studies into communication standards to be adopted, the number of output channels and the type of connectors to be chosen are still required. A further possibility could be to develop a more complex detector system to be employed around particle accelerators to support true on-line non-intrusive beam monitoring. Both these tasks would require dedicated studies and investigations should be performed.

Concerning the BSS-LUPIN, a future study could investigate the possibility of simplifying the unfolding procedure, necessary to obtain the solution spectrum. This is currently performed offline and

requires a considerable amount of time. A LabVIEW interface could be developed in which the number of counts obtained by each sphere would be inserted and the resulting spectrum calculated by taking into account the BSS response matrix, implemented in the code. This would drastically reduce the time needed to perform the unfolding of acquired data. Moreover, one could envisage developing a novel unfolding code using the existing interface, but based on a parametrical method. This code should be developed by taking into account the typical shape of the spectrum of stray radiation fields characterised by PNF. Some tests have already been performed by developing the first part of a code by using WinBUGS [WinBUGS 2014], but further studies are still needed.

Given that the LUPIN electronics and the innovative technique used to analyse the collected signal proved to be efficient in measuring the intensity of PNF as rem counter, beam loss monitor and neutron spectrometer, future investigations could be directed in finding new detection techniques that can be couples to the LUPIN electronics front end. A light-weight rem counter designed to work without moderators, such as the one described in ref. [Nakamura 2012] could be envisaged.

# Appendix

The description of the working principle and the main specifications of the neutron active detectors used for comparison in the measurement campaigns described in Section 2.2. are given below, together with the response functions, where available. For each detector, together with the commercial name, also the acronym, which has been used for simplicity throughout the text, is given in parentheses. In the text the term "conventional rem counter" has been employed for detectors whose maximum energy range is limited up to 20 MeV, as it is the case for BIOREM, LB6411 and 2202D, whereas the term "extended-range rem counter" has been used for detectors with a good sensitivity up to the GeV range, i.e. LINUS and Wendi-2.

**Thermo Scientific BIOREM FHT 752 (BIOREM)**

The Thermo Scientific FHT 752 BIOREM (Fig. A1) is a commercial neutron dose rate meter for stationary and portable use, especially suited for environmental measurements. It employs a $BF_3$ proportional counter placed in a cylindrical moderator containing polyethylene and boron carbide. The output is given in *H*(10)*, but an internal calibration factor, expressed in nSv/count, can be set by the user. The calibration carried out at CERN with a PuBe neutron source resulted in a calibration factor of 1.52 $nSv^{-1}$. The response function [Dumitrescu and Chirosca 2011] is given in Fig. A2.

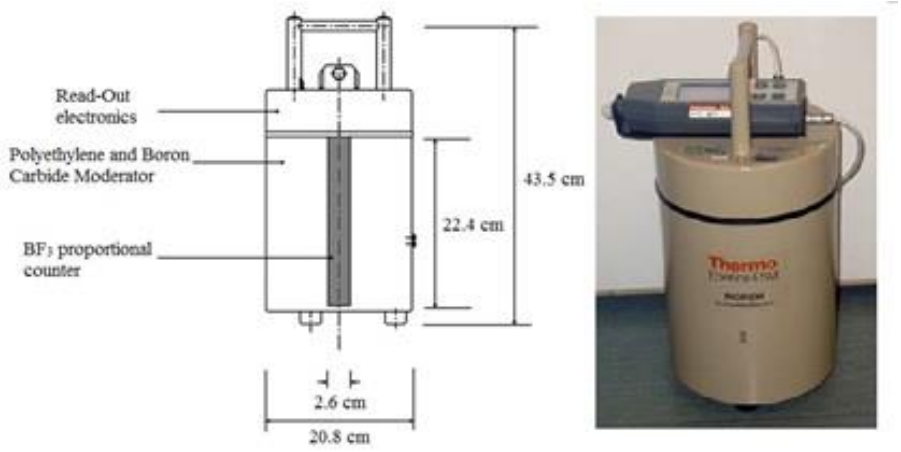


FIG. A1. Geometry (left) and picture (right) of BIOREM.

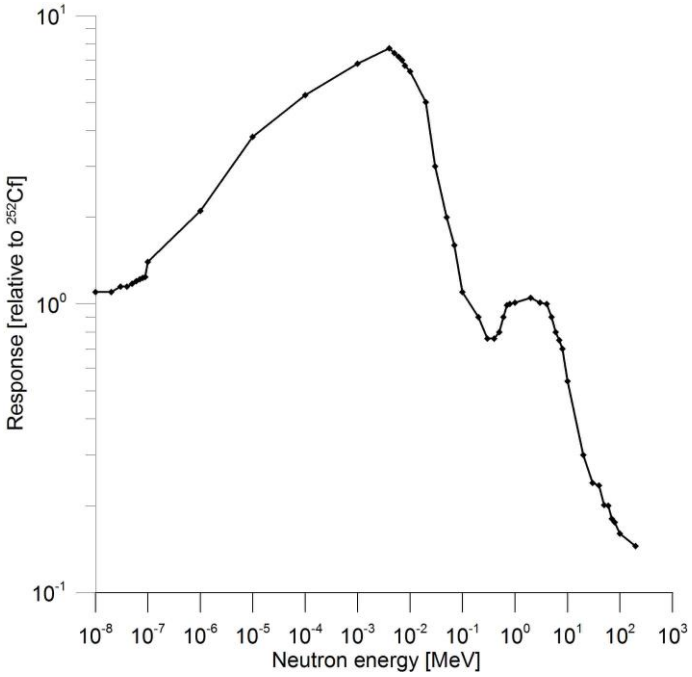


FIG. A2. Response function to neutrons of BIOREM, expressed in units relative to the response of moderated $^{252}$Cf.

**Berthold LB6411 (LB6411)**

The neutron probe Berthold LB6411 (Fig. A3) is a commercial rem counter designed to measure *H*(10)* in different radiation fields up to 20 MeV. It consists of a $^{3}$He/methane proportional counter surrounded by a spherical moderator of polyethylene with density of 0.95 g/cm$^{3}$.The response function [Burgkhardt et al. 1997] is given in Fig. A4.

FIG. A3. Picture of LB6411.

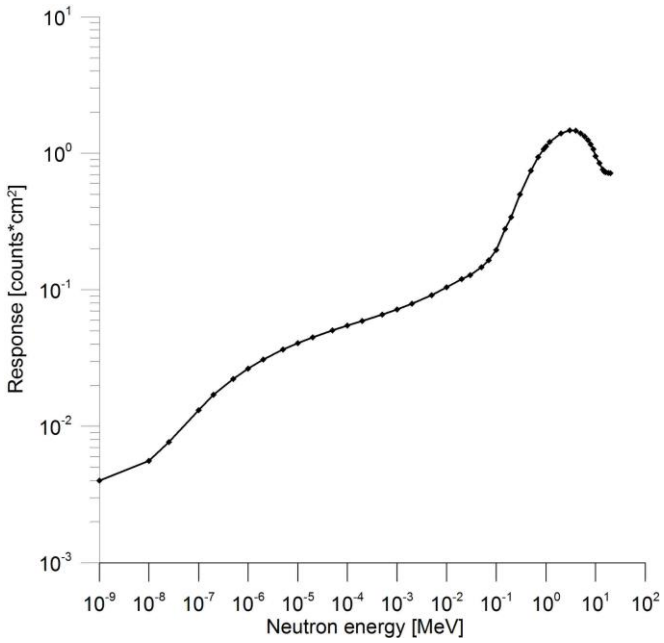


FIG. A4. Response function to neutrons of LB6411.

**Studsvik 2202D (2202D)**

The Studsvik 2202D is a rem counter produced by Studsvik Instrument AB (now KWD Nuclear Instrument AB) with an approximate *H*(10)* response in the energy range from thermal up to 17 MeV. The instrument consists of a BF3 proportional tube embedded in a cylindrical moderator provided with a boron plastic shield. The calibration carried out at CERN with a PuBe neutron source resulted in a calibration factor of 1.03 $nSv^{-1}$. The response function is very similar to the one shown for the LB6411 in Fig. A4.


FIG. A5. Picture of Studsvik 2202D.

**CERN Long Interval NeUtron Survey meter (LINUS)**

The Long Interval NeUtron Survey meter (LINUS) [Birattari et al. 1990, Birattari et al. 1992, Birattari et al. 1993, Birattari et al. 1998] (Fig. A6) in use at CERN is the original extended range neutron rem counter developed about in the 90s years ago from an Anderson-Braun type device. The detector consists of a $^{3}$He proportional counter embedded in a spherical polyethylene moderator, which incorporates a boron-doped rubber absorber and a 1 cm thick lead shell to extend its response function to several hundred MeV by the generation of intermediate-energy neutrons via (n,xn) inelastic scattering reactions. The calibration carried out at CERN with a PuBe neutron source resulted in a calibration factor of 1.09 nSv$^{-1}$. The response function is given in Fig. A7.

FIG. A6. Picture of CERN LINUS.

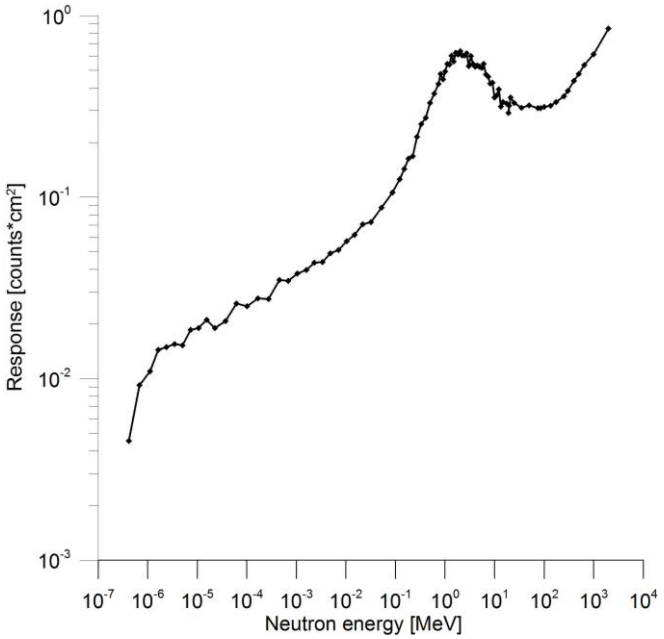


FIG. A7. Response function to neutrons of CERN LINUS.

**Thermo Scientific Wendi-2 FHT 762 (Wendi-2)**

The Thermo Scientific FHT 762 Wide Energy Neutron Detection Instrument (Wendi-2) is a commercial extended range rem counter designed to measure the *H*(10)* rate within an energy range from thermal up to 5 GeV [Jägerhofer et al. 2012]. It consists of a $^{3}$He proportional counter surrounded by a cylindrical polyethylene moderator assembly and a layer of tungsten powder. This additional layer of high-Z material enhances the detector response to high-energy neutrons via inelastic scattering interactions [Olsher et al. 2000, Olsher and McLean 2008]. The geometry of the detector is shown in Fig. A8. The output is given in *H*(10)*, but the internal calibration factor can be changed by the user. The calibration carried out at CERN with a PuBe neutron source resulted in a calibration factor of 3.13 nSv$^{-1}$. The response function of the detector [Jägerhofer et al. 2012] is shown in Fig. A9.

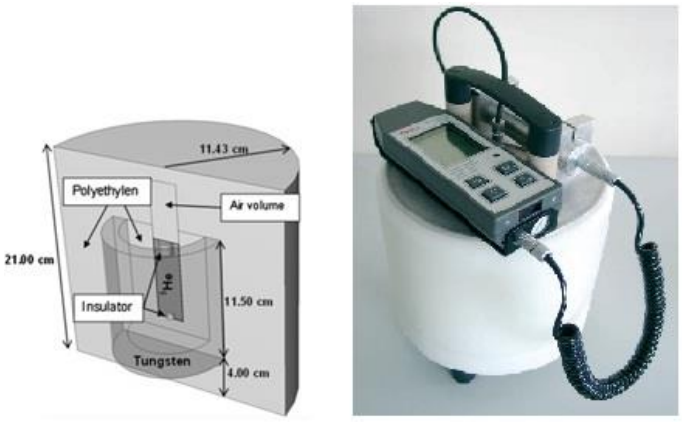


FIG. A8. Geometry (left) and picture (right) of Wendi-2.

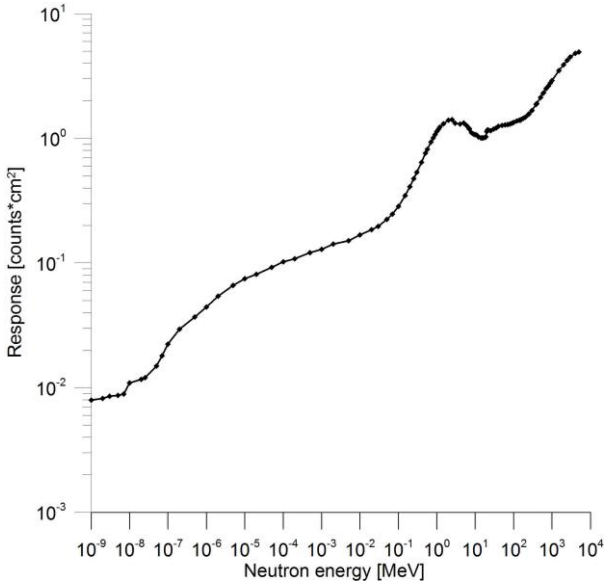


FIG. A9. Response function to neutrons of Wendi-2.

**Framework Scientific ABC 1260 (ABC)**

The Framework Scientific ABC 1260 Neutron Dosimeter (Fig. A9) is a portable neutron area monitor that can be controlled via a PC. It is based on the superheated drop technology [Apfel et al. 1993]. Bubble formation events are recorded in real time by means of piezoelectric transducers picking up the acoustic pulses emitted during drop vaporization. If used with special emulsions, this detector provides a direct measurement of *H*(10)* and *H*(10)* rate. Following an approach similar to that used in the development of the CERN LINUS, its response can be extended to several hundred MeV with the addition of a 1 cm thick cylindrical lead shell placed around the detector cap [Agosteo et al. 2000, D'Errico et al. 2002]. The calibration carried out at CERN with a PuBe neutron source resulted in a calibration factor of 0.01 $nSv^{-1}$.

FIG. A10. Picture of ABC bubble detector (left) and the additional lead shell (right).

**Thermo Scientific RadEye™ NL (RadEye™)**

The Thermo Scientific RadEye NL (Fig. A11) is a commercial neutron radiation detector. It uses a $^{3}He$ proportional counter with 2.5 bar ($2.5 \cdot 10^{5}$ Pa) filling pressure and is equipped with a small-size polyethylene moderator to increase the efficiency to fast neutrons. Its main purpose is to detect radiation sources more than estimating a neutron dose rate [Thermo 2012]. The calibration was performed with the CERN PuBe source by embedding the detector in the polyethylene moderator. This showed a strong geometrical dependence, with a calibration factor varying between 0.47 and 0.80 $nSv^{-1}$.

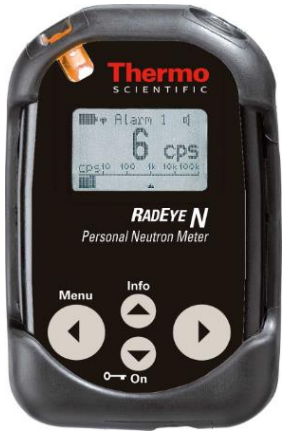


FIG. A11. Picture of RadEye NL.

**Hydrogen and Argon-filled Centronic IG5 ionisation chambers**

The Hydrogen and Argon-filled ionisation chambers used in the measurements are employed in the CERN RAMSES system. They are Centronic IG5-H20 and IG5-A20 ionisation chamber, respectively. They are designed for use in mixed radiation fields as they are capable of detecting high-energy charged particles, photons and neutrons. The gas is pressurised to 20 bars ($2 \cdot 10^6$ Pa). The energy range of the chamber is from 65 keV to 10 MeV for Hydrogen and from 50 keV to 10 MeV for Argon. The measuring range is from 1 µGy/h to 10 Gy/h for Hydrogen and from 100 nGy/h to 10 Gy/h for Argon. The geometry of the chambers is shown in Fig. A12.


FIG. A12. Geometry and picture of the IG5 ionisation chamber. The active gas can be either pressurised Hydrogen or Argon.

A current-to-frequency converter converts the charge created in the active volume to TTL pulses, which can be collected by digital data acquisition cards. To convert the output signal into *H*(10)*, a calibration factor, expressed in nSv/pC or nSv/count, must be applied. This is calculated for each monitoring station according to the expected neutron and gamma spectra in the area. The calculation is done by folding the response function of the detector (shown in Fig. A12 for the neutron component only [Theis et al. 2004]) with the spectra known experimentally or obtained via Monte Carlo simulations.

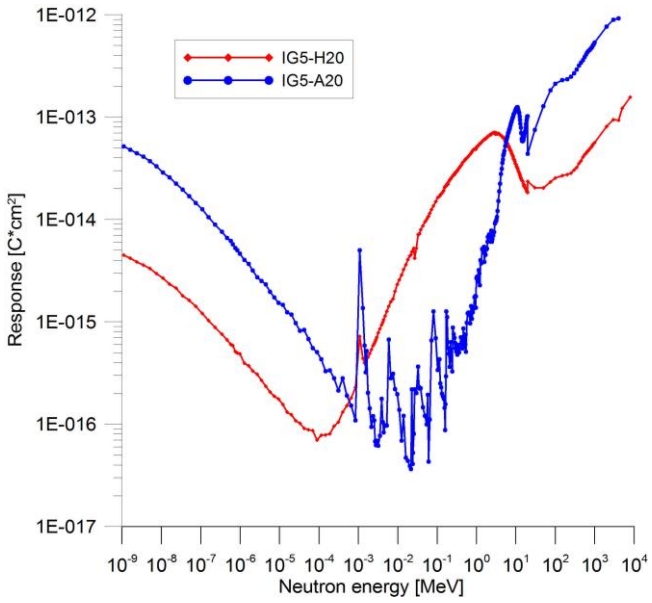


FIG. A13. Response function to neutrons of the IG5-H20 ionisation chamber.

# Bibliography

The validity of the hyperlinks given for some references has been verified in January 2015.

[Agosteo 2010] S. Agosteo, Overview of novel techniques for radiation protection and dosimetry, Rad. Meas. 45 (2010) 1171-1177.

[Agosteo et al. 2000] S. Agosteo, M. Silari and L. Ulrici, Improved response of bubble detectors to high-energy neutrons, Rad. Prot. Dos. 88 (2000) 149-155.

[Agosteo et al. 2010] S. Agosteo, M. Caresana, M. Ferrarini and M. Silari, A dual-detector extended range rem-counter, Rad. Meas. 45 (2010) 1217-1219.

[Ambarzumjan and Iwanenko 1930] W.A. Ambarzumjan, D.D. Iwanenko, On a consequence of the Dirac theory of protons and electrons (in German), Doklady USSR Acad. Sci. Ser. A (1930) 153-155.

[Andersen et al. 2012] K. Andersen, D. Argyriou, K. Batkov, C. Böhme, S. Bousson, I. Bustinduy, C. Carlile, P. Carlsson, L. Celona, M. Comunian et al., European spallation source (ESS) conceptual design report, ESS Report ESS-2012-001 (2012), http://esss.se/documents/CDR_final_120206.pdf.

[Apfel et al. 1993] R.E. Apfel, J.D. Martin and F. d'Errico, Characteristics of an electronic neutron dosemeter based on superheated drops, Health Phys. Suppl. 64 (1993) S49.

[Astier et al. 2003] P. Astier, D. Autiero, A. Baldisseri, M. Baldo-Ceolin, M. Banner, G. Bassompierre, K. Benslama, M. Besson, I. bird, B. Blumenfeld, Prediction of neutrino fluxes in the NOMAD experiment, Nucl. Instrum. Meth. A 515 (2003) 800-828.

[Aza et al. 2013b] E. Aza, M. Caresana, C. Cassell, V. Colombo, S. Damjanovic, S. Gilardoni, G.P. Manessi, M. Pangallo, D. Perrin and M. Silari, Instrument intercomparison in the stray neutron field around the Proton Synchrotron, CERN Technical Note, CERN-RP-2013-054-REPORTS-TN-V.2 (2013),https://edms.cern.ch/file/1295335/3/CERN-RP-2013-054-REPORTS-TN_V2%28PS_intercomparison%29.pdf.

[Badano et al. 1999] L. Badano, M. Benedikt, P. Bryant, M. Crescenti, P. Holy, P. Knaus, A. Maier, M. Pullia and S. Rossi, Synchrotron for hadron therapy: part I, Nucl. Instrum. Meth. A 430 (1999) 512-522.

[Badano et al. 2007] L. Badano, O. Ferrando, M. Caccia, C. Cappellini, V. Chmill, M. Jastrazb, K. Abbas, U. Holzwarth, P.N. Gibson and G. Molinari, A real-time beam monitor for hadrontherapy applications based on thin foil secondary electron emission and a back-thinned monolithic pixel sensor, Proceedings of the 8th European Workshop on Beam Diagnostics and Instrumentation for Particle Accelerators, Venice, Italy, 20-23 May 2007, WEPC20 (2007) 352-354.

[Barquero et al. 2002] R. Barquero, R. Mendez, M.P. Iniguez, H.R. Vega and M. Voytchev, Thermoluminescence measurements of neutron dose qround a medical linac, Rad. Prot. Dos. 101 (2002) 493-496.

[Barranco and Gilardoni 2011] J. Barranco and S. Gilardoni, Simulation and optimization of beam losses during continuous transfer extraction at the CERN proton synchrotron, Phys. Rev. Spec. Top-Ac. 14 (2011) 030101.

[Barros et al. 2014] S. Barros, V. Mares, R. Bedogni, M. Reginatto, A. Esposito, I.F. Goncalves, P. Vaz and W. Ruhm, Comparison of unfolding codes for neutron spectrometry with Bonner spheres, Rad. Prot. Dos., doi:10/1093/rpd/nct353.

[Bedogni et al. 2007] R. Bedogni, C. Domingo, A. Esposito and F. Fernandez, FRUIT: an operational tool for multisphere neutron spectrometry in workplaces, Nucl. Instrum. Meth. A 580 (2007) 1301-1309.

[Battistoni et al. 2007] G. Battistoni, S. Muraro, P.R. Sala, F. Cerutti, A. Ferrari, S. Roesler, A. Fassò and J. Ranft, Proceedings of the Hadronic Shower Simulation Workshop 2006, Fermilab, Chicago, Illinois, USA, 6-8 September 2006, M. Albrow, R. Raja eds., AIP Conference Proceeding 896 (2007) 31-49.

[Billen and Roderick 2006] R. Billen and C. Roderick, The LHC logging service: capturing, storing and using time-series data for the world's largest scientific instrument, CERN Technical Note, CERN-AB-Note-2006-046 (2006), http://cds.cern.ch/record/1000757/files/ab-note-2006-046.pdf.

[Birattari et al. 1990] C. Birattari, A. Ferrari, C. Nuccetelli, M. Pelliccioni and M. Silari, An extended range neutron rem counter, Nucl. Instrum. Meth. A 297 (1990) 250-257.

[Birattari et al. 1992] C. Birattari, A. Esposito, A. Ferrari, M. Pelliccioni and M. Silari, A neutron survey meter with sensitivity extended up to 400 MeV, Rad. Prot. Dos. 44 (1992) 193-197.

[Birattari et al. 1993] C. Birattari, A. Esposito, A. Ferrari, M. Pelliccioni and M. Silari, Calibration of the neutron rem counter LINUS in the energy range from thermal to 19 MeV, Nucl. Instrum. Meth. A 324 (1993) 232-238.

[Birattari et al. 1998] C. Birattari, A. Esposito, A. Ferrari, M. Pelliccioni, T. Rancati and M. Silari, The extended range neutron rem counter 'LINUS': overview and latest developments, Rad. Prot. Dos. 76 (1998) 135-148.

[Bohm 1976] J. Bohm, Saturation corrections for plane-parallel ionisation chambers, Phys. Med. Biol. 21 (1976) 754-759.

[Bramblett et al. 1960] R.L. Bramblett, R.I. Ewing and T.W. Bonner, A new type of neutron spectrometer, Nucl. Instrum. Meth. 9 (1960) 1-12.

[Briesmeister 2000] J.F. Briesmeister, MCNP, a general Monte Carlo N-particle transport code, version 4C, LANL Report LA-13709 (2000).

[Burgkhardt et al. 1997] B. Burgkhardt, G. Fieg, A. Klett, A. Plewnia and B.R.L. Siebert, The neutron fluence and *H*(10)* response of the new LB 6411 rem counter, Rad. Prot. Dos. 70 (1997) 361-364.

[Caresana et al. 2013a] M. Caresana, M. Ferrarini, G.P. Manessi, M. Silari and V. Varoli, LUPIN, a new instrument for pulsed neutron fields, Nucl. Instrum. Meth. A 712 (2013) 15-26.

[Caresana et al. 2013c] M. Caresana, A. Denker, A. Esposito, M. Ferrarini, N. Golnik, E. Hohmann, A. Leuschner, M. Luszik-Bhadra, G.P. Manessi, S. Mayer, K. Ott, J. Röhrich, M. Silari, F. Trompier, M. Volnhals and M. Wielunski, Intercomparison of radiation protection instrumentation in a pulsed neutron fields, Nucl. Instrum. Meth. A 737 (2014) 203-213.

[Chadwick 1932] J. Chadwick, Possible existence of a neutron, Nature 192 (1932) 312.

[Charitonidis et al. 2012] N. Charitonidis, G.P. Manessi and M. Silari, Test run for the HRMT-15 (RPINST) experiment, CERN Technical Note, CERN-DGS-2012-092-RP-TN (2012), https://edms.cern.ch/file/1242218/1/CERN-DGS-2012-092-RP-TN_HiradMat_Test_Run.pdf.

[Charitonidis and Harrouch 2013] N. Charitonidis and E. Harrouch, Round detector support for the HRMT-15 (RPINST) experiment, CERN Technical Note, EDMS No. 1144976 (2013), https://edms.cern.ch/file/1144976/1/TN-RADIATION-STUDIES-FINAL-including_accident_scenarioV2.pdf.

[Cybulski et al. 2012] T. Cybulski, C.P. Welsch and T. Jones, Non-invasive beam diagnostics for a 60 MeV proton beam, Beam Instrumentation Workshop, Newport News, Virginia, USA, 16-19 April 2012, TUPG011 (2012) 152-154.

[D'Errico et al. 2002] F. d'Errico, S. Agosteo, S. Sannikov and M. Silari, High-energy neutron dosimetry with superheated drop detectors, Rad. Prot. Dos. 100 (2002) 529-532.

[Damjanovic et al. 2012] S. Damjanovic, M. Widorski and S. Gilardoni, Shielding studies for the Route Goward / PS crossing, CERN Technical Note, CERN-DGS-2011-065-RP-TN (2012), https://edms.cern.ch/file/1161799/2/2012-CERN-DGS-2011-065-RP-TN-sr-sd.pdf.

[Domingo et al. 2010] C. Domingo, M.J. Garcia-Fuste, E. Morales, K. Amgarou, J.A. Terron, J. Rosello, L. Brualla, L. Nunez, R. Colmenares, F. Gomez, G.H. Hartmann, F. Sanchez-Doblado and F. Fernandez, Neutron spectrometry and determination of neutron ambient dose equivalents in different LINAC radiotherapy rooms, Rad. Meas. 45 (2010) 1391-1397.

[Dighe et al. 2004] P.M. Dighe, K.R. Prasad, S.K. Kataria, Silver-lined proportional counter for detection of pulsed sources, Nucl. Instrum. Meth. A 523 (2004) 158-162.

[Dinter and Tesch 1976] H. Dinter and K. Tesch, Moderated rem meters in pulsed neutron fields, Nucl. Instrum. Meth. 136 (1976) 389-392.

[Dumitrescu and Chirosca 2011] D. Dumitrescu and A. Chirosca, Neutron field correction coefficients for active and passive dosimeters in Cernavoda NPP, Adv. Mat. 5 (2011) 690-695.

[Efthymiopoulos et al. 2011] I. Efthymiopoulos, C. Hessler, H. Gaillard, D. Grenier, M. Meddahi, P. Trilhe, A. Pardons, C. Theis, N. Charitonidis, S. Evrard, H. Vincke and M. Lazzaroni, HiRadMat: a new irradiation facility for material testing at CERN, Proceedings of the 2nd International Particle Accelerator Conference, San Sebastian, Spain, 4-9 September 2011, TUPS058.

[Esposito and Nandy 2004] A. Esposito and M. Nandy, Measurements and unfolding of neutron spectra using Bonner spheres, Rad. Prot. Dos. 110 (2004) 555-558.

[Ferrari et al. 2005] A. Ferrari, P.R. Sala, A. Fassò and J. Ranft, FLUKA: a multi-particle transport code, CERN-2005-10, INFN/TC_05/11, SLAC-R-773 (2005), http://www.slac.stanford.edu/cgi-wrap/getdoc/slac-r-773.pdf.

[Ferrari et al. 2014] A. Ferrari, F.P. La Torre, G.P. Manessi, F. Pozzi and M. Silari, Monitoring reactions for the calibration of relativistic hadron beams, Nucl. Instrum. Meth. A 763 (2014) 177-183.

[Fröhlich 2008] L. Fröhlich, Beam loss monitors, Energy Recovery Linear Instrumentation Workshop, Ithaca, New York, USA, 2-3 June 2008, presentation available at http://www.lars-froehlich.de/download/ERL_instrumentation_ws_2008_BLMs.pdf

[ICRP 1996] International Commission on Radiological Protection, Conversion coefficients for use in radiological protection against external radiation, IRCP publication 74, Ann. ICRP 26 (1996).

[ICRP 2007] International Commission on Radiological Protection, The 2007 recommendations of the International Commission on Radiological Protection, IRCP publication 103, Ann. ICRP 37 (2007).

[IEC 2014] International Electrotechnical Commission, Radiation protection instrumentation – Neutron ambient dose equivalent (rate) meters, IEC 61005:2014, Edition 3.0 (2014).

[Iijima et al. 2011] K. Iijima, T. Sanami, M. Hagiwara, K. Saito and S. Sasaki, Development of a current-readout type neutron monitor for burst neutron fields, Progr. Nuc. Sci. Tech. 1 (2011) 300-303.

[Jägerhofer et al. 2012] L. Jägerhofer, E. Feldbaumer, C. Theis, S. Roesler and H. Vincke, A new method to calculate the response of the Wendi-2 rem counter using the FLUKA Monte Carlo code, Nucl. Instrum. Meth. A 691 (2012) 81-85.

[Justus 2012] A.L. Justus, Count rate limitations for pulse-counting instrumentation in pulsed accelerator fields, Health Phys. 102 (2012) 8-24.

[Klett et al. 2007] Pulsed neutron monitoring, a new approach, Proceedings of the IEEE 2006 Nuclear Science Symposium and Medical Imaging Conference, San Diego, California, USA, 29 October - 1 November, NSS Conference Record 2 (2007) 806-808.

[Klett et al. 2010] A. Klett, A. Leuschner and N. Tesch, A dose meter for pulsed neutron fields, Rad. Meas. 45 (2010) 1242-1244.

[Knoll 2010a] G.F. Knoll, Radiation detection and measurement, 4th edition, John Wiley & Sons, Inc., 79-83.

[Knoll 2010b] G.F. Knoll, Radiation detection and measurement, 4th edition, John Wiley & Sons, Inc., 121-126.

[Knoll 2010c] G.F. Knoll, Radiation detection and measurement, 4th edition, John Wiley & Sons, Inc., 159-183.

[Knoll 2010d] G.F. Knoll, Radiation detection and measurement, 4th edition, John Wiley & Sons, Inc., 524-527.

[Knoll 2010e] G.F. Knoll, Radiation detection and measurement, 4th edition, John Wiley & Sons, Inc., 649.

[Kramer et al. 2007] D. Kramer, B. Dehning, E.B. Holzer and G. Ferioli, Secondary electron emission beam loss monitor for LHC, Proceedings of the 8th European Workshop on Beam Diagnostics and Instrumentation for Particle Accelerators, Venice, Italy, 20-23 May 2007, WEPC03 (2007) 313-315.

[Latu 2007] M. Latu, Radiation monitoring system for the environment and safety, CERN Technical Note (in French), EDMS No. 770397.

[Leake 1966] J.W. Leake, A spherical dose equivalent neutron detector, Nucl. Instrum. Methods 45 (1966) 151-156.

[Leake et al. 2010] J.W. Leake, T. Lowe, R.S. Mason and G. White, A new method of measuring a large pulsed neutron fluence or dose exploiting the die-away of thermalised neutrons in a polyethylene moderator, Nucl. Instrum. Meth. A 613 (2010) 112-118.

[Luszik-Bhadra et al. 2010] M. Luszik-Bhadra, E. Hohmann and T. Otto, A new neutron monitor with silver activation, Rad. Meas. 45 (2010) 1258-1262.

[Luszik-Bhadra and Hohmann 2009] M. Luszik-Bhadra and E. Hohmann, A new neutron monitor for pulsed fields at high-energy accelerators, Proceedings of the 12th International Congress of IRPA, Buenos Aires, Argentina, 19-24 October 2008 (2009).

[Mallows et al. 2012] S. Mallows, E.B. Holzer and J. van Hoorne, Fiber based BLM system research and development at CERN, Proceedings of the 52nd ICFA Advanced Beam Dynamics Workshop on High-Intensity and High-Brightness Hadron Beams, Beijing, China, 17-21 September 2012, THO3C05 (2012) 596-600.

[Mayer and Brysk 1975] F.J. Mayer and H. Brysk, Neutron detection efficiency of silver counters, Nucl. Instrum. Meth. 125 (1975) 323-324.

[Mitaroff and Silari 2002] A. Mitaroff and M. Silari, The CERN-EU high-energy reference field (CERF) facility for dosimetry at commercial flight altitudes and in space, Rad. Prot. Dos. 102 (2002) 7-22.

[Monaco et al. 2006] L. Monaco, P. Michelato, C. Pagani, P. Pierini and D. Sertore, Dark current investigation of flash and pitz RF guns, Proceedings of the 10th European Particle Accelerator Conference, Edinburgh, UK, 26-30 June 2006, WEPLS051 (2006) 2493-2495.

[Nakamura and Heilbronn 2006] Handbook on secondary particle production and transport by high-energy heavy ions, World scientific publishing company (2006).

[Nakamura 2012] T. Nakamura, Neutron detector development and measurements around particle accelerators, Indian J. Pure Ap. Phy. 50 (2012) 427-438.

[Nuttall 2012] W.J. Nuttall, R.H. Clarke and B.A. Glowacki, Resources: stop squandering helium, Nature 485 (2012) 573-575.

[Olsher et al. 2000] R.H. Olsher, H.H. Hsu, A. Beverding, J.H. Kleck, W.H. Casson, D.G. Vasilik and R.T. Devine, Wendi: an improved neutron rem meter, Health Phys. 79 (2000) 170-181.

[Olsher and McLean 2008] R.H. Olsher and T.D. McLean, High-energy response of the PRESCILA and Wendi-II neutron rem meters, Rad. Prot. Dos. 130 (2008) 510-513.

[Payne and Whitehead 2006] S.J. Payne and S.A. Whitehead, Fine spatial beam loss monitoring for the ISIS proton synchrotron, Proceedings of the 10th European Particle Accelerator Conference, Edinburgh, UK, 26-30 June 2006, TUPCH035 (2006) 1079-1081.

[Pedrozzi 2010] M. Pedrozzi, SwissFEL injector conceptual design report, PSI Report 10-05 (2010), http://www.psi.ch/swissfel/HomeEN/SwissFEL_Injector_CDR_310810.pdf.

[Rebai et al. 2012] M. Rebai, L. Giacomelli, C. Andreani, A. Fazzi, C.D. Frost, E. Perelli Cippol, A. Pietropaolo, M. Rhodes, M. Tardocchi, E. Schooneveld and C. Gorini, Diamond detectors for fast neutron measurements at pulsed spallation sources, J. Instrum. 7 (2012) C05015.

[Reginatto and Goldhagen 1999] M. Reginatto and P. Goldhagen, MAXED, a computer code for maximum entropy deconvolution of multisphere neutron spectrometer data, Health Phys. 77 (1999) 579-583.

[Reginatto et al. 2003] M. Reginatto, B. Wiegel, A. Zimbal, UMG code package version 3.2. PTB (2003).

[Reillo 2008] E. Reillo, D. Cano-Ott and T. Martinez, On the neutron transparency of various materials proposed for the AIDA enclosure, CINEMAT Internal Report 12.05.2008, http://www2.ph.ed.ac.uk/~td/AIDA/Meetings/12May2008/AIDA%20chamber.pdf.

[Rios et al. 2013] I. Rios, J. Gonzalez and R.E. Mayer, Total fluence influence on the detected magnitude of neutron burst using proportional detectors, Rad. Meas. 53-54 (2013) 31-37.

[Rossi 2011] S. Rossi, The status of CNAO, Eur. Phys. J. Plus 126 (2011) 78.

[Rutherford 1920] E. Rutherford, Nuclear constitution of atoms, Proc. Roy. Soc. A97 (1920) 374.

[Schmidt et al. 2009] C. Schmidt, T. Stahl and E. Mergel, Current problems in the field of radiation protection technique - Use of active personal dosimeters (APD) in pulsed radiation fields, in: Proceedings of the 2009 EUROSAFE Forum for nuclear Safety, Brussels, Belgium, 2-3 November 2009 (2009), http://www.eurosafe-forum.org/files/Presentations2009/Seminar5/Abstracts/5.3-Current%20problems%20in%20the%20field%20of%20radiation%20protection%20technique-Schmidt-Mergel-Stahl.pdf.

[Shea and Morgan 2010] D.A. Shea and D. Morgan, The helium-3 shortage: supply, demand, and options for congress, Congressional Research Service, 2010, http://fas.org/sgp/crs/misc/R41419.pdf.

[Shiltsev 1998] V.D. Shiltsev, Fast PIN-diode beam loss monitors at Tevatron, Nucl. Instrum. Meth. A 29 (1998) 81-92.

[Slaugther and Pickles 1979] D.R. Slaughter and W.L. Pickles, A highly sensitive silver-activation detector for pulsed neutron sources, Nucl. Instrum. Meth. 160 (1979) 87-92.

[Stockner et al. 2007] M. Stockner, B. Dehning, C. Fabjan, E.B. Holzer and D. Kramer, Classification of the LHC BLM ionization chamber, Proceedings of the 8th European Workshop on Beam Diagnostics and Instrumentation for Particle Accelerators, Venice, Italy, 20-23 May 2007, WEPC09 (2007) 328-330.

[Sutter 2011] A. Sutter (As-Raydetect-Gmbh, Official distributor of Centronic for Switzerland) Private communication, 2011.

[Theis et al. 2004] C. Theis, M. Rettig, S. Roesler, H. Vincke, Simulation and experimental verification of the response functions of Centronic high-pressure ionisation chambers, CERN-SC-2004-23-RP-TN (2004), https://edms.cern.ch/file/456393/3/IG5_response_simulations.pdf.

[Thermo 2008] Thermo Scientific Inc., Thermo Scientific FHT 725 / FHT 752 H User's manual, Version 28.02.2008.

[Thermo 2012] Thermo Scientific Inc., RadEye™ selection guide, Version 08.2012.

[Thomas et al. 1984] P.M. Thomas, K.G. Harrison and M.C. Scott, A multisphere neutron spectrometer using a central $^{3}$He detector, Nucl. Instrum. Methods 224 (1984) 225-232.

[Tomoka and Fukasuka 1984] T. Tomoda and S. Fukasuka, Deterioration and recovery of $BF_3$ counters due to operation in intense radiation fields, Nucl. Instrum. Meth. 224 (1984) 557-565.

[Vanhavere et al. 2004] F. Vanhavere, D. Huyskens and L. Struelens, Peripheral neutron and gamma doses in radiotherapy with an 18 MeV linear accelerator, Rad. Prot. Dos. 110 (2004) 607-612.

[Von Dardel and Sjostrand 1954] G. Von Dartel and N.G. Sjostrand, Diffusion parameters of thermal neutrons in water, Phys. Rev. 96 (1954) 1245-1249.

[Weizhen et al. 2009] W. Weizhen, L. Jianmin and K. Kejun, A modified neutron dose-equivalent meter for pulsed radiation field, Nucl. Instrum. Meth. A 603 (2009) 236-246.

[Westcott 1948] C.H. Westcott, A study of the expected loss rates in the counting of particles from pulsed sources, Proc. R. Soc. Lon. Ser-A 194 (1948) 508-526.

[WinBUGS 2014] D. Spiegelhalter, A. Thomas, N. Best and D. Lunn, WinBUGS User Manual, www.mrc-bsu.cam.ac.uk/bugs

[Wittenburg 2008] K. Wittenburg, Beam loss monitors, Proceedings of the CERN Accelerator School 2008, 249-280.

[Woznicka et al. 2000] U. Woznicka, K. Drozdowicz and J. Dabrowska, A generalized interpretation of buckling experiments for thermal neutrons, Nucl. Instrum. Meth. A 455 (2000) 660-669.

[Zhukov 2010] A. Zhukov, Beam loss monitors: physics, simulations and applications in accelerators, Proceedings of the Beam Instrumentation Workshop 2010, Santa Fe, New Mexico, USA, May 2010, THTNB01 (2010) 553-565.